1-1-2013

Visual Exploration And Information Analytics Of High-Dimensional Medical Images

Darshan Pai
Wayne State University,

VISUAL EXPLORATION AND INFORMATION ANALYTICS OF HIGH-DIMENSIONAL MEDICAL IMAGES

by

DARSHAN PAI

DISSERTATION

Submitted to the Graduate School

of Wayne State University,

Detroit, Michigan

in partial fulfillment of the requirements

for the degree of

DOCTOR OF PHILOSOPHY

2013

MAJOR: COMPUTER SCIENCE

Approved by:

_____

Advisor Date

_____

_____

_____

ACKNOWLEDGMENTS

I would like to express my gratitude to the many people who saw me through my research; to all those who provided support, exchanged ideas, and offered comments that helped make this dissertation possible.

I would like to specially thank my advisor, Dr. Jing Hua, for his guidance during my PhD years. His professional commitment and accessibility during the last several years provided me with the necessary training and expertise towards conducting research and publishing papers. I would also like to thank my external committee member, Dr. Otto Muzik, for his help with all my projects and giving access to the data sources. His constructive criticisms and prompt feedback was essential towards the development of robust applications.

I am also very grateful to Dr. Ming Dong and Dr. Daniel Grosu for serving on my prospectus and dissertation committee. I received plenty of constructive suggestions and invaluable comments on this dissertation. Thanks to Dr. Hamid Soltanian-Zadeh and Dr. Jeffery Loeb for providing me with data whenever necessary.

Thanks to my colleagues in the Graphics and Imaging Laboratory, past and present: Dr. Zhaoqiang Lai, Dr. Guang-Yu Zou, Dr. Yunhao Tan, Dr. Chang Liu, Dr. Vahid Taimouri, and Dr. Jiaxi Hu, for their support and good wishes.

Last but not the least: I would like to thank God, my parents, my doting sister, and my lovely wife for their love and support during my PhD journey. I beg forgiveness of all those who have been with me over the course of the years and whose names I have failed to mention.

TABLE OF CONTENTS

LIST OF TABLES

LIST OF FIGURES

CHAPTER 1

INTRODUCTION

Data visualization is a rapidly evolving field and has transformed how we analyze increasingly large and complex data sets. The hardware resources are improving fast, and with the vast computing resources available, massive amounts of data can be reliably generated and stored. This data is multidimensional, having many complex attributes and variables; the attribute themselves can be multidimensional quantities (vector, tensor). The challenge is to sift through this data and identify the most relevant dimensions for knowledge discovery and classification. Innovative visualization tools are needed to qualitatively browse through the datasets, summarize the data, and assist the user in finding structure, trends, features, outliers, and correlations. Depending on the task at hand, an expert user can confirm a hypothesis, explore attributes within the data through advanced interaction tools, identify consistent patterns, or refine an existing visualization to optimize the data. This systematic visualization framework has been proven to be beneficial in a variety of domains such as machine learning, computer vision, gene-expression analysis, traffic management, social integration, stock market, and data mining. There are nontrivial visualization challenges within the medical imaging field. The most notable research in medical imaging is the analysis of neurological disorders afflicting the human brain. The brain is the most advanced organ in the human body. An exquisitely dynamic system, all aspects of human existence are explained by intricate low-level interactions between distinct biological processes. Researchers studying the brain have provided descriptive constructs at the biological and molecular level. It has also been described in terms of its chemical constituents and labeled as a set of psychological concepts. However, the characterization of these various descriptions is possible only through computational studies on high-level brain function. Medical image analysis is currently at the forefront of human brain research because of rapid advances in acquisition devices, and it produces high-dimensional and multiresolution

functional images. The internal mechanisms of the various processes are abstracted within the information space of each modality. Various brain states corresponding to motor skills, language, communication, sensory perception, emotions, and sleep have been mapped to precise brain activity measurements. Scientific visualization tools confirm these measurements using an accurate 3-D rendering of the spatial structure of the brain. Mapping functional modalities within the 3-D context allows scientists to visually project high-level function from different anatomical vantage points with excellent detail. Algorithmic advances in functional mapping have made analysis of brain disorders very popular in the clinical fraternity. Cross-subject statistical comparisons of functional maps across multiple subject groups have been successful in generating a diagnostic signature describing the disease. But the current system is still very limited in generating predictive indicators with high fidelity. A successful surgery does not always guarantee a favorable future prognosis. The reason for the poor outcome is because most of these analysis results are mapped to, at most, two features. The available statistical tools do not fully utilize the entire information feature space composed from different image modalities, thus limiting human judgments regarding the important process that governs the symptom, which is a critical deficiency for accurate prediction.

The objective of our research is the development of a robust visualization framework with three important goals. The first goal is to develop a rigorous mathematical model for spatial alignment of brain shapes. The accurate transformation of the spatial structure into distinct analysis units forms the anatomical basis for systematic statistical design in functional and morphological brain disorder studies. The second goal is the design of a visual spatial representations for integration, exploration, and analysis of a large collection of medical images. The integration of multiple images is essential for exploring the data and understanding the subtle relationship between distinct features. The third goal is an analytical processing framework design that combines the power of human insight to iteratively devise clever data-driven techniques that interactively guide the user toward discovering relevant hypotheses. The trans-

formation of multiple images into a high-dimensional feature space is composed along the anatomical basis, and an interface equipped with augmented visual representations assists the user during the exploration of subtle relationships and interdependencies among multiple features. The hypotheses is confirmed in real time, and confirmatory visualizations present the final results within the global anatomical context. The potential gain for the analyst is an intelligent and interactive visual analytic tool for understanding the human brain dynamics that synergize complex biological processes defining human behavior.

1.1 The Needs and Challenges in Multimodal Medical Images

Medical imaging devices and technologies have seen rapid advancement in recent years, which has also impacted the quality as well as the amount of raw data generated. This, along with minimally invasive procedures, has opened a new frontier in research for discovering similar or disparate patterns among cross-subject populations using image-based data-driven computing models. There is no single image modality that can comprehensively capture the brain dynamics. Data acquisition scanners capture certain aspects of a biological process and abstract it within the information space of the modality. Each acquisition of an image modality carries qualitatively different information content, associated with its inherent strengths and limitations. This information space captures either the morphological snapshot of the brain or the high-level functional snapshot of the brain. For example, a T1 modality image of the brain clearly identifies the various tissue structures within the brain. This type of imaging can generate a high spatial resolution of the data after 3-D reconstruction. But apart from segmentation, any ability to quantify the image or analyze the various tissues based on function is limited. In contrast, molecular imaging data, such as positron emission tomography (PET), provide very detailed quantitative information of brain activity but lack anatomical detail. Electrophysiological brain activity is recorded using EEG grids and provides a good temporal resolution

but does not include specific localization information. Functional magnetic resonance imaging (fMRI) and single-photon emission computed tomography (SPECT) measure brain response to routine tasks like learning or communication. Diffusion tensor imaging (DTI) generates a vector-valued image of the diffusion properties of the white matter tissue. Susceptibility weighted imaging (SWI) and magnetic resonance angiography (MRA) provide detailed structure images on the vasculature of the brain. These images are diverse and are acquired using vastly disparate protocols. Most of these images are intrinsically multidimensional and derive a bunch of distinct and equally high-dimensional and multiresolution features. Examining abnormal behavior and composing it as a cooperative set of specific functions becomes a task in brain reverse engineering. Finding a correlation between the salient features from these different images is non-trivial and difficult to perceive except for some discernible cases. This need for multiple-image modalities also requires a systematic mechanism to combine the information from multiple modalities. Through our research, we present a coordinated visualization framework for multimodality integration for qualitatively providing invaluable clinical information from these diverse modalities, analyzing relationships, and discovering abnormalities within and across populations.

1.2 Merits of a Coordinated Visualization Framework

Humans are most responsive to visual information. Since neuroimaging data is high-dimensional and very complex, a systematic visual representation of data guides the user towards a better understanding, exploration, and management of brain disorders. The merits of a coordinated visualization framework is listed below.

1.2.1 Geometric Modeling for Spatial Alignment of Images

Ideally, for medical imaging data, there is no clear model that describes the normal brain activity. For quantifying abnormal behavior in a patient, it becomes necessary to generate the normative distribution for comparison. Statistical models can be built that allow the pooling of data sources across subject populations exhibiting normal behavior. But the inherent phys-

iological variability of the brain makes it difficult to identify the homotopic regions on the brain surface. Along with the complexity of the acquired data, which is mostly unstructured, this can easily overwhelm the useful information and affect the likely outcome of the study. This problem can be solved by developing a structural basis for composing the morphological and functional features for testing. For accurate comparative studies, an accurate spatial alignment framework has to be constructed. Since the physiological variability can be encoded within the intrinsic geometric space of the surface shape, we follow an explicit geometrical construction for surface alignment. Essentially, the brain is considered as a 3-D object. A computational geometry-based alignment methodology developed within our coordinated visualization framework explicitly captures various geometric features within the brain that will drive a mapping and registration algorithm for accurate shape alignment. This creates a homotopic space across different subjects for exploring biologically significant measures. This space also forms the anatomical basis that defines the structure of the feature data acquired from multiple modalities. A systematic composition of the features, along with an accurate structural alignment, allows the user to explore varied features within the global anatomical context of the brain, but with the added ability to focus on a particular anatomical vantage point.

1.2.2 Quantifying Medical Images

Because of the brain's highly convoluted structure, it is difficult to localize pathological brain tissue. Abnormal behavior will manifest itself as a functional abnormality or a morphological abnormality. To quantify the abnormality, much of the initial speculation comes from past experiments and empirical pieces of evidence from similar studies. Neurologists examine existing cases and suggest features to compare based on the abnormalities they observe. The features are arranged within a spreadsheet or a statistical package for comparative analysis. To successfully test a hypothesis, the reference set is selected based on various criteria not limited to age, environmental factors, and psychology. For each patient, the modality is processed manually, and the quantified value corresponding to the feature is saved for anal-

ysis. If localization varies across patients, the reference set will have to be processed once for testing every patient. Depending on the number of references included in the study and the speed of processing needed for quantification, a successful analysis may require several days. If speculation fails to generate a noticeable result, a different hypothesis is tested, and the data processing starts all over again. This process is very time-consuming and is prone to trial and error thus making it impossible to explore the entire feature set. Moreover, finding the relationship between multiple significant features is not intuitive in all cases and is typically ignored due to lack of insight. The visual analytics framework offloads some of the laborious aspects of the analysis by providing an intelligent system that works in unison with the human analyst. Ranking measures associated with each feature indicates its significance and can be visualized and manipulated interactively by the user based on his expert knowledge and insight gained from the visual representative models. Multiple features can be tested and compared directly to identify interesting patterns and verified in real time. This data-driven model for comparative analysis is possible due to easy access of information coupled with an interactive visual interface for feature representation.

1.2.3 New and Emerging Modalities

A new and emerging modality may introduce interesting features that needs to be tested within the current statistical model. Apart from the data processing step, the statistical model may require restructuring to incorporate the new modality. The characterization of the feature may not be very intuitive, and there may be disagreement regarding the significance of the new features. The feature might have a different format, making it difficult to incorporate for statistics. Because the new modality is a potential information source, our visual framework allows for expanding the feature space. We have multiple feature formats available for comparison, with each feature format having a specific ranking criteria so that the significance can be easily perceived. The processing of the new modality is initiated to transform the features in a form compatible with the current mathematical basis structure created within the framework.

Once the features are incorporated within the visual framework, it can be mapped to visual entities and visualized using the different viewing options available. It can be easily tested for interdependencies with other available features. The final analysis results can be very easily visualized and verified in real time as described in the previous section.

1.2.4 Tool for Image Analytics

Medical images are essentially high-dimensional. For each individual subject, various features derived from its corresponding imaging modality is composed into a high-dimensional feature vector. The features may themselves be multidimensional or simple 1-D scalar measures. During exploratory analysis, the user does not know what the output will be or how it will be derived. The goal is to use expert knowledge and insight to explore the significant patterns within the high-dimensional data. Visual analysis of information within this high-dimensional data can be challenging. To aid with the exploration, an interactive visual interface with real-time response to queries is paramount. Moreover, the display device is 2-D and of limited resolution. Humans have a hard time perceiving relationships within the data for anything greater than five dimensions: two of the dimensions represent the orthogonal axis with the other dimensions representing shape, size, and color of the data points. To manage the high-dimensional unstructured feature set, the system provides a systematic data representation to tackle basic problems intrinsic to this analysis. First, the highly complex structure of the brain is managed by the systematic division of the brain in terms of anatomical viewpoints. This initial description of the spatial dimension forms the structural basis for subgrouping the overlapping multidimensional features from the various image modalities. Second, an array of visualizations within each spatial dimension window provides tools for manipulating different parameters for feature selection and comparing multiple visualizations side by side for interactive trial and error. Visual encodings of size, shape, and color are provided to leverage perceptual skills toward interpreting patterns among features. These specifications are translated to formal queries and reflected across different subject groups. Thus, provenance

is maintained across the population and interactively assembled on demand as a coordinated multi-view table layout with the salient features mapped to columns and the rows categorized into different subject groups. To the best of our knowledge, our approach is the first attempt to use visual analytics for a multimodality integration of medical images. This will potentially generate a high-level understanding of the underlying disorder, leading to faster and more accurate prediction of the disease and its symptoms and, subsequently, a better prognosis.

1.2.5 Other Advantages

- Brain parcellation: The brain surface is subdivided into a finite set of triangular ROI elements, called the *surface ROI mesh*. The surface mapping algorithm designed for the alignment of brain shapes ensures that each element within the *surface ROI mesh* is homotopic across populations. In other words, each element in one subject is anatomically equivalent to the corresponding element in a different subject. The entire set of elements forms the anatomical dimension for composing the functional and morphological features for visual analysis. The ROI element is large enough to generate the true distribution of the brain activity for each feature. The anatomical basis follows a hierarchical parcellation routine, and the level of subdivision can be dynamically changed. The basis can be further optimized by anatomical labeling schemes that cluster different elements together to highlight the brain activity based on true anatomical boundaries. Another advantage of the parcellation is that there are no self-intersections on the surface. This is a direct consequence of the intrinsic parameterization algorithm used for surface mapping.

- Native-space analysis: Native space refers to the original brain surface reconstructed from the corresponding anatomical image. Template space is the average brain surface to which different subjects are aligned to. The template provides a common reference system for the anatomical alignment of individual brain surfaces. The native-space analysis is better suited for multimodality data integration in clinical routine, as clinical management decisions are usually evaluated for a particular subject under very specific con-

ditions. Template-space analysis suffers from excessive smoothing and warping during the alignment of the original data to the template. We lose the most perceivable features such as structure-specific differences and characteristic individual variabilities in the data. With a conformal mapping-based geometric alignment framework, it is easier to characterize and quantify abnormal brain behavior in the native brain space of each individual subject. The advantage of native-space analysis is an increased precision in analysis and minimal statistical error.

1.3 Research Contributions

Our research contributions are summarized below:

1. Design and develop an algorithm for surface and volume alignment of individual brain shapes to the template brain. The algorithm is an explicit geometric computation paradigm based on the parametrization of the surface to a canonical domain and uses intrinsic geometric entities for driving the mapping algorithm. The algorithm initiates the volume alignment once the surface mapping is fixed.

2. Develop a statistical environment for cross-subject analysis optimized with scientific visualization tools for quantifying and confirming brain abnormalities. Abnormal behavior is quantified either through a functional modality or a structural modality. In this dissertation, we concentrate on three modalities, namely, the PET, DTI, and EEG. The MRI image is used for alignment and to provide an anatomical context.

3. Design a spatial representation for coordinated visualization of the various data sources. We develop a coordinated multi-view table layout for simultaneous visualization of salient features in 3-D that guides the analyst in his exploration process. We also design a 2-D representation that maps multiple features to visual encodings and discover interdependencies between them. The goal is to enhance the information sources clearly so that implicit relationships can be easily perceived.

4. Design a coordinated visual analytics framework for the integration and management of the feature sets. The analyst uses the interactive interface to select features, and generate its significance ranks. He/She can manipulate the data in different ways to visually deduce, in real time, patterns, correlations, and interdependencies between multiple features.

1.4 Dissertation Organization

The remainder of this dissertation is organized as follows: Chapter 2 begins with an overview of past and current practices in the field of medical image analysis, information visualization, and visual analytics. In Chapter 3, after a literature review of the surface mapping procedures, we delve into a rigorous mathematical construction of the template model that will be the reference for the global alignment of individual geometric shapes. The surface and the volumetric mapping process will be explained in detail. The final mapping will be validated for accuracy using a qualitative testing mechanism. Chapter 4 will present detailed case studies for characterizing brain disorders. We will list the statistical design and the data processing steps taken for each experiment. The neural fiber reconstructions using DTI will facilitate algorithms for analyzing its vector-valued features. In Chapter 5, the visual analytic framework called BrainFusion is presented, which is a comprehensive interface that allows for analysis of the high-dimensional feature space. We will describe the design of two spatial representations, namely, the coordinated multi-view table layout and the Mollweide view. The complete design of the framework is explained in detail along with case studies that will highlight the efficacy of the application. The final chapter concludes the dissertation and summarizes our contribution to visual computing in brain research and lists some interesting ideas for future work within this domain.

CHAPTER 2

BACKGROUND

The field of brain research has shown tremendous progress over the years. The advancement of neuroimaging for brain characterization allows clinicians to gather analysis data either on the underlying anatomy or the high-level brain function. Over the past two decades [31], improved acquisitions and large scale development of the analysis methodologies targeted three critical application areas:

1. Integration of the functional and the anatomical image sources [109].

2. Mapping information within different patient groups [115].

3. Comparison studies across different subject populations [105].

The visualization of the analysis results is an inherent part of the computing model. Scientific visualization tools reconstruct the true physical space of a subject in a virtual computing environment. Researchers use these tools for confirmatory analysis, and also to visualize the results in the anatomical space. These visualizations become critical decision markers for the intended clinical or surgical outcome. Currently, a large number of features, extracted from multiple modalities, are available for analysis. These features are complex, multidimensional, and overlap with each other in the physical space, making integration, and subsequent significance testing hard to achieve.

Research in various fields have highlighted the advantages of exploratory data analysis. Information visualization and visual analytics use data-driven mechanisms that employ human insight in conjunction with automated computing analysis models. This capability of data-driven exploration exemplifies the knowledge gained through the analysis. High dimensional data are processed and manipulated interactively, and an increased understanding of the data translates to a very high level of information and knowledge transfer. For example, researchers

in the bioinformatics and gene-expression analysis fields use information visualization techniques for identifying subtle relationships among genes and proteins that are indistinguishable in the physical space. The goal of our research is to develop visual analytic techniques for multimodality integration of high-dimensional neuroimaging datasets. This will reduce the time for exploration of significant features, highlight the relationships between various features, and confirm prognosis results with high fidelity.

The research spans several major fields of study including geometry processing of images, geometry based mapping and registration, statistical brain analysis, information visualization, and visual analytics. The following sections briefly review some of the prior work.

2.1 Geometry Processing

Volume data acquired from 3-D scanners is typically unstructured data. Ideally, analysis of images quantifies changes in shape and/or physiological function. Accurate processing of the images is indispensable for identifying the structure of interest as well as extracting the features to be used as constraints for subsequent mapping and analysis. Image segmentation has been a field of active research for a long time but remains the most difficult and an important first step in image processing systems. An accurate segmentation of anatomical brain structures and their compact 3-D geometrical representation is difficult due to the complexity and physiological variability of the structures under study. Moreover, sampled data introduces artifacts that cause non-uniformity in the data. These can induce bias field, intensity distortions, and noise that causes structural boundaries to be indistinct and disconnected. Lower resolution images as well as partial volume effects can further complicate an already ill-posed problem. Segmentation approaches are classified into low- and high-level approaches. Low-level approaches are mainly model-free approaches [100, 97, 51, 45, 68, 142] and work directly with voxel information such as intensity and texture. Since most of these methods only include local information during segmentation, the object boundaries are not consistent. They do not account for the extreme shape complexity and variability among individuals, and will regularly require expert

intervention to correct these inaccuracies. The development of continuous deformable models provide a geometric model-based approach based on Lagrangian dynamics that handles the shortcomings of earlier methods. Since then, an extensive body of literature has emerged on deformable models in computer vision and medical image analysis [84]. To adapt to complex topologies [83], various geometric deformable models [19, 20] were developed. Geometric variants, especially discrete models [90, 101, 54], are more adept at handling real complex topologies since they provide more appropriate control of the shape deformations compared to implicit models. Moreover, incorporating prior shape information [29, 77, 101] for boundary determination has proven helpful for robust and accurate segmentation of the 3-D structures. The following papers [137, 50, 27] cite various successful attempts to improve the computing speed and reduce the dependency on initial conditions. An interesting alternative to the deformable model is an implicit level-set surface where the contour deformation is mathematically represented as a propagating wavefront. Level sets can be easily solved in terms of partial differential equations, which constrain the propagation based on image-derived information. During the past decade, various medical image segmentation methods based on level sets have been proposed [111]. Osher and Sethian gives an excellent review on the applications of level sets in their book [88].

2.2 Image Registration and Alignment of Surfaces

Pooling the data within patient groups requires an accurate anatomical alignment between images. Aligning multiple images to each other is a very difficult problem because of the natural physical variability that exists between different individuals. This is much more prominent in human brains where sulcal and gyral folds on the surface differ in size, shape, and structure from one subject to another. To minimize statistical error in functional group analysis it is important to reduce the bias introduced by anatomical variability. Additionally, to warp a generic atlas-model or a user-defined template to the patient data, minimizing the influence of anatomical variability is indispensable. Registration of brain volumes is one of the first

methods of alignment [113]. It uses a limited reproducible set of anatomical landmarks for affine registration between two images. The underlying assumption is that the images and tissues are highly similar to each other leading to poor alignment results for cases where local variation is high. Hence, automatic non-rigid deformation-based intensity methods [5, 135] became more popular. Based on the domain of the biological problem, registration approaches are broadly classified into different categories. The classifications are based on the spatial dimension, nature of the transformation, order of the transformation, and the parameterization of the transform [81]. Most of the methods described above work well for small deformations but do not handle the topology of the structure very well. Hence, a group of diffeomorphic maps were developed that handles large deformations [25] and also ensures that the topology is preserved during the mapping [24, 47, 9]. This is advantageous for aligning images to a standard reference system [115] and subsequent analysis in the common atlas space. Applications using intensity-based volumetric registration are very robust for sub-cortical structures within the brain since their topology is very consistent, but is not very effective for cortical surface alignment. The surface of the brain has a very convoluted topology and the features are essentially non-Euclidean. Surface based alignment procedures use essential geometrical properties of the surface for inter-subject registration. It uses either a parameterization approach to flatten the surface to a plane [57] or a sphere [40], or directly work with the surface geometry [118, 64]. The surfaces are modeled as a 2-D closed manifold [48, 120, 140] while topologically describing it in the spherical coordinate system. Correspondences are established between surfaces through warping in the spherical coordinate system [139, 144], precluding the necessity to deform the original 3-D surface. To ensure an accurate surface alignment, various geometric features for example, curve landmarks and sulci folds, are delineated [64, 93, 131]. Various methods for automatic matching have also been proposed in literature [129, 120, 139]. Automatic alignment still remains a very challenging problem and landmark-based surface matching has been more accurate and reliable [95]. Combined approaches for volumetric as

well as cortical surface registration [130, 93, 65, 46] have also been developed and are capable of aligning both the surface as well as sub-cortical structures within the brain. In this proposal, we use conformal parametrization of the surface in the spherical domain and employ landmark constraints for accurate surface registration between individual brain images. We use thin-plate splines for warp regularization using corresponding landmark points as deformation interpolants.

2.3 Statistical Image Analysis

As powerful algorithms were devised for robust alignment of brain datasets, analyzing differences in anatomical structures as well as functional analysis were naturally considered. The natural physical variability among individuals within a particular group and between cross-subject populations combined with a lack of a common physical model, describing the mean anatomy and its variation within the group, makes statistical shape analysis the most attractive solution for comparative studies. Knowledge of the underlying variability also reduces the statistical error in functional neuroscience studies. Brain mapping tools and automatic morphometric methods replaced the classic ROI-based strategies for analyzing area, length, and volume of the tissue structures under study. Analysis of shape incorporate various geometric features like the sulci patterns on the cortical surface, gyral patches, sulcal folding depth, vector fields, and curvature. Other scalar measures defined over the shape such as area, volume, and point clouds describe the gross statistics while ignoring the fine geometric details. White matter analysis incorporate diffusion tensor measures for describing the underlying white matter atrophy. Subsequent neural connectivity analysis highlights the organization of the white tissue micro-structure. These analysis studies have been applied to various medical analysis problems identifying changes in the brain due to aging, development, cognitive skills, diseases, and longitudinal studies [117]. Analysis of the anatomical variations within a particular group have also lead to the construction of average multi-subject atlases [115, 113, 9], which describes a common reference model that can be used for alignment and registration for future studies

within that group. These models can also be designed as a generative model [33] that can describe and simulate specific deformation criteria. Brain mapping provides spatial normalization algorithms that align to a common reference system of a template anatomy (atlas or prototype brain). These mapping methods use either affine [60] or low-dimensional nonlinear volume based registration [135, 5] or non-linear surface warping techniques [139, 39, 35, 143], as described in the earlier section. Voxel-based morphometry [6] methods are a set of algorithms that perform whole brain analysis of gray and white matter densities. This point-to-point comparison studies in 3-D, measures gross differences in volumes as well as function (PET-MR and fMRI-MR studies) within the subject data. This methods works very well for analysis of sub-cortical shapes, but require blurring of the data [6] to account for variability, especially in the cortical surface. The blurring reduces the statistical power, requiring a larger sample size for meaningful statistics [133]. In contrast, results from the analysis of shapes and functional analysis performed using surface-based techniques generates better statistics [4]. Moreover, incorporating knowledge of major sulci during warping is more reasonable than blind morphing procedures driven only by surface features. The deformation that maps one shape onto another have been useful for measuring significant anatomical variability among different subjects [7, 37, 32]; the basis for deformation-based morphometry. Various extrapolating schemes have also been developed that use the information from the matched landmarks to create a variability map of the entire space [37, 32]. An alternative method to pure coordinate-based morphometries uses an automatic ROI generation algorithm for whole-brain analysis. Local shape features generated for each subject creates a deformation and provides a method for creating a set of ROI elements based on a anatomy-based parcellation scheme [82] or a shape-based parcellation scheme [94]. In this proposal, we develop a similar scheme for parcellation. We first use a diffeomorphic mapping to create a conformal parametrized spherical surface [143] that is aligned to the template using constrained landmark matching and warp regularization [144]. ROIs are defined using a subdivision scheme on the template and rep-

resents the unit of analysis, which is transfered back to the native subject space for statistical native-space brain analysis [94].

2.4 Information Visualization

Information visualization is a field of research in computer graphics designed for the analysis of abstract data. The goal of this visualization is to generate an intelligent mapping of the data to the screen and highlight the internal structure of its information. Abstract data is large, high-dimensional, may contain non-spatial and non-numeric parameters, and is either structured or unstructured. Interactive graphical representations of abstract data reinforce the cognition of the human analyst. Interactions allows the user to transform the data, explore the various relationships hidden within its internal structure, and gain an in-depth understanding of the connections within the data.

2.4.1 Information Visualization in Medicine

The complementary information spaces represented by each image modality display a snapshot of the brain within that space. The basic problem is to integrate the disparate spaces and furnish a comprehensive characterization. BrainFusion (Chapter 5) presents our first attempt to reverse engineer the brain using visual analytics and uncover an insightful prediction. In the past, visual analysis in the medical domain was used in the area of bioinformatics to understand the interactions between genes [103]. The rank-by-feature framework [104] provides a good exploration statistic for the identification of relevant genes and their interconnectivity. Low-dimensional visual representations [22, 61] of white matter fiber tracts using DTI images help with the clustering of fiber bundles for studying the anatomical connectivity between specialized regions. The techniques furnish a coordinated multi-view layout for flexible selections between the 2-D abstraction and the 3-D spatial view to gain useful anatomical information but do not perform any analysis across subject groups. Recently, [59] introduced the 'connectogram' that produces a circular representation of the human cortical network architecture for classifying neuroconnectivity relationships that combines multiple acquisition protocols to cal-

culate associated volumetrics and morphometrics. A recent paper by Borkin *etal* [15] describes a 2D-3D interface for visualization of stress on the artery wall.

2.4.2 Multidimensional Visualization

There have been numerous techniques to effectively visualize high-dimensional datasets, such as scatterplots and scatterplot matrices [21], parallel coordinates [58], hyperslices, iconic displays [23], dense pixel displays [71], stacked displays [76], and star glyphs [132]. These are general representations of high-dimensional data and easily scalable to the requirements of a specific domain. They provide effective visualizations at lower dimensions and reduce visual clutter. Relevant information can be obtained by focusing on important visual representations. Automated dimensionality reduction techniques such as principal component analysis (PCA), multidimensional scaling (MDS) [14], and self-organizing maps (SOM) [73] produce interesting patterns for most well-behaved datasets, but the outputs tend to be static visualizations and do not support exploration. Various tools such as projection pursuit [41, 56] and grand tour [8, 28] were proposed to not only provide excellent views of high-dimensional projections but also search for low-dimensional projections that reveal interesting structures. These methods have a clear advantage over automated analysis techniques [70] for datasets which do not reveal patterns automatically and need human knowledge and creativity for improved results. However, these techniques are exhaustive and quickly became cumbersome as the datasets became larger and representations reached the level of cognitive overload. Intuitive techniques that off-load some of the insight deduction logic to a computational machine agent allow the construction of models [44] with arbitrary relationships that fit the data. Moreover, to enhance visual expressiveness and more flexibility toward exploration, interactive navigation [34] is encoded within visual representations that support automatic reordering of relevant dimensions. Dimension ordering [3] is another technique that places similar dimensions together and forms a clustering of important low-dimensional projections [138, 49]. Ranking measures [114, 104, 107, 102, 134] quantify each visual representation within a set of candidate

visualizations based on relevance. This helps the user to focus on the most expressive structures at the start of the exploration stage and effectively manage high-dimensional data. [62] describes a technique that provides initial parameters regarding the number of dimensions and tolerance value on information loss due to low-dimensional projections, as a guidance toward visualizing interesting patterns.

2.4.3 Low-Dimensional Projections

Multidimensional datasets are usually explored in a low-dimensional projection space. Dimensional reduction has inherent advantages of reducing the visual clutter and to identify interesting dimensions for visualization. The easiest and most popular techniques utilize Principal Component Analysis (PCA), Multidimensional Scaling (MDS), and Self-Organizing Maps (SOM) [73]. In a majority of cases dimensions that are identified correspond to interesting patterns within the data. These patterns may not be intuitive for novice users. Projection pursuit attempts to locate important features on the dimensions itself. The algorithm tours through the high-dimensional data set and arranges the dimensions such that the most interesting or the most similar dimensions are listed together. [34] uses a variant of the projection pursuit [28] to make a matrix of scatterplots that are reordered to allow for smooth navigation between the different dimensions through query building. A rank-by-feature method described in [104] gives a rank to each feature providing the user with an intuitive idea about projections that will generate the most interesting patterns.

2.4.4 Interactive Exploration

Interaction in multidimensional datasets is important especially for exploring data where interesting patterns are vague or unclear. Interactive interfaces has many forms and is oriented towards how the user intends to use the data. Interactive navigation help explore the various dimensions of the underlying data [34]. For visualizing interdependencies between different datasets, the overview and detail is provided by Focus+context visualization techniques. Interactions are needed to visualize interdependencies between visual representations and navigate

between multiple visualizations. This provides flexibility during exploration and helps users to instantly check the outputs and manipulate them as necessary. Interactions allow for zooming into certain parts of the data while keeping track of global context [70]. Table Lens [98] is a interactive filtering technique that provides a bigger screen layout to certain parts of the data independent of the overview. Multiple views of the dimensions is rendered for interactive clustering in hierarchical clustering methods [103]. A taxonomy of interactions in information visualization is provided in [75].

2.5 Summary

Medical image data from various acquisition sources will be treated as a high dimensional feature vector. These high dimensional datasets will be analyzed interactively in a visual analytic framework to gather knowledge about specific pathological subject groups under study. Identifying the relationships between the various dimensions will reflect and enrich the pathological description thus leading to more precise knowledge of the underlying cause. Specific questions and hypothesis tests can be verified and the most sensitive measures can be ranked and evaluated. The various techniques and methodologies are described beginning from the next chapter.

CHAPTER 3

CONSTRAINT-BASED CONFORMAL MODEL FOR MAPPING AND REGISTRATION

In this chapter, we introduce the Standard Conformal Brain Model (SCBM). It represents the canonical model used for inter-subject mapping and global alignment of brain structures. The SCBM is mathematically formulated using geometrical concepts in conformal parameterization. An explicit geometry based technique performs robustly under extreme physiological surface variations. We start this chapter by describing the motivation behind using a geometry-based method for alignment. A brief explanation of the mathematics of conformal parameterization is given, as we formulate the theory for the standard conformal model construction and describe the algorithm designed for the alignment of individual brain surfaces to the model. The anatomical surface ROI unit for analysis is described next, followed by an illustration of the entire pipeline using an example brain data set. We extend the SCBM with a tetrahedral mesh solution to create the volumetric conformal model (VCM) for matching brain volumes. The last section will provide a detailed assessment of the spatial accuracy and validate our claim regarding the robustness of the brain-mapping algorithm to accurately align anatomical boundaries.

3.1 Motivation

Comparative analysis and statistical inference [85, 110, 117] play a crucial role in the interpretation of neuroimaging data [136, 43, 116]. Statistical models defined on the diseased brain identify significant changes in function and structure when compared with normal subject populations. Quantifying these differences help describe guidelines for a future course at diagnosis and surgical planning. The most challenging step is to identify anatomically homologous regions in the brain - especially on the cortical surface - invariant of the extreme physiological

variations prevalent across individuals. Research in brain mapping and registration is one of the most investigated areas in medical image analysis and neuroscience ([43, 39, 121]). Currently, there are two distinct categories for brain registration - the **implicit intensity-based technique** and the **explicit geometry-based technique**.

Implicit intensity-based techniques do not require an explicit segmentation of the brain volume. The most common technique is to use an intensity based warping algorithm to guide an individual brain image to a reference atlas image. Voxel-based analysis methods such as statistical parametric mapping (SPM) [43] and FSL [108] are powerful techniques used for comparing functional modalities. It provides an efficient algorithm for processing brain volumes without initial ROI selections. There is extensive literature ([17, 72, 86, 99]) describing the usefulness of SPM analysis for detecting functional abnormalities. However, due to the small-scale physiological variation in brain structure among subjects it is impossible to assign identical anatomical locations to image voxels. Hence the data is heavily smoothed to improve the likelihood of image voxels to correspond anatomically. As a consequence, these methods suffer from suboptimal sensitivity and the subsequent necessity to exclude data sets that significantly deviate from the template.

Explicit geometry-based technique takes advantage of intrinsic geometric properties in the brain structure to achieve improved mapping and registration. Recent studies [55, 4] have demonstrated that intensity-based approaches cannot address the huge variability of cortical patterns among individuals. The papers suggest using surface-based methods [119] that explicitly identify salient geometric features on the cortex for registration. Since the brain is a 3-D object, myriad representations are available for extracting features for surface analysis. Some of these representations include: curvature based representations [124], regional point representations [26], spherical harmonic representations [69], shape distribution [87], spline representations, harmonic shape images [141], and surface feature indexing. However, the brain has a complex and convoluted structure and these methods do not extract enough distinc-

tive features in order to generate a good final mapping. Most of these methods get stuck in local minima, affecting the final result. Studies described in [80, 123] start with a manually labeled brain atlas that is warped to the individual brain surface and the labels transferred onto the subject's cortical surface. Popular software programs such as FreeSurfer [38] and Caret [35], model the brain as a cortical sheet in canonical space, which is geometrically accurate and topologically correct. Using an isometric transformation, each individual brain surface is mapped to a canonical sphere. Their mathematical formulation is constructed in the 3-D embedding space (Euclidean). Surface registration can also be equivalently carried out in the parametric domain [128, 129, 79]. The brain surface is topologically equivalent to the sphere and is easily parameterized to the spherical domain [48]. Subsequent matching and registration is much more efficient in this canonical space. The reasons are as follows: first, because the registration is similar to a plastic deformation along a 2-D sheet, many of the errors associated with transformations in the Euclidean space (self-intersections) are eliminated; second, this registration can be implicitly scale-invariant, for example if we use conformal mapping; and third, the 3-D registration is reduced to a 2-D computing problem that is more efficient.

In the last few years, conformal mapping techniques have gained a wider acceptance in brain mapping [119, 57]. But conformal mapping on its own cannot account for the inherent variability and induces distortion. Energy optimization approaches based on minimizing a global cost functional (or flow equation) work well but have the disadvantage of being restricted to a local minimum. Hence, to achieve high registration accuracy, non-rigid deformation techniques [131] are employed, along with an explicit match of local homologous features in the anatomical space [143].

3.2 Surface Parameterization: Theory

3.2.1 Conformal Mapping

In differential geometry, surfaces are modeled as 2-$manifolds$ that have an inherent 2-D structure. 3-D surfaces can be represented in the 2-D space using surface parameterization

schemes. Conformal mapping has recently become popular because of its many practical merits - angle-preserving, intrinsic to surface geometry, and being independent of the approximating mesh resolution [57, 48]. Mathematically, local conformal structure can be defined as follows. Suppose M is a 2-manifold with a set of local coordinate charts $\{(U_i, \Phi_i)\}$, where U_i are open sets on M, the union of which covers M, and $\Phi_i : U_i \rightarrow \mathbf{R}^2$ is a homeomorphism that maps U_i to the planar parameter domain. A point p on M can be covered by multiple local coordinate charts, e.g., (U_i, Φ_i) and (U_j, Φ_j), the coordinate transition function $\Phi_{ij} : \Phi_j \circ \Phi_i^{-1}$ converts one pair of local parameters $\Phi_i(p)$ to another, $\Phi_j(p)$. A Riemannian metric on the surface M is a differential quadratic form and is locally represented as

$$ds^2(u, v) = E(u, v)du^2 + 2F(u, v)dudv + G(u, v)dv^2, \tag{3.1}$$

where u, v are the local coordinates. A Riemann surface is a two-dimensional manifold, such that all transition functions are analytic functions. The Riemannian metric has a special form within each chart,

$$ds^2(u, v) = \lambda(u, v)(du^2 + dv^2). \tag{3.2}$$

These types of local coordinates are called isothermal coordinates. Suppose $\Phi : M \rightarrow N$ is a diffeomorphism between two Riemann surfaces, (U, Φ) is a chart on M with the local isothermal coordinates denoted by (x, y), while (V, Ω) is a chart on N with the local isothermal coordinates denoted by (u, v), and $\Phi(U) \subset V$. The Φ restricted on U induces a map between the parameter domain, $\Phi : (x, y) \rightarrow (u(x, y), v(x, y))$. If

$$\frac{\partial u}{\partial x} = \frac{\partial v}{\partial y}, \quad \frac{\partial u}{\partial y} = -\frac{\partial v}{\partial x} \tag{3.3}$$

holds for any restrictions of Φ, then Φ is called the *conformal map*. $\lambda(u, v)$ is called the *conformal factor*. Conformal means angle preserving. Suppose γ_1 and γ_2 are two arbitrary curves on M that intersect at the point p with angle α, and Φ is a conformal map from M to

N, then $\Phi(\gamma_1)$ and $\Phi(\gamma_2)$ are two curves on N that intersect each other at the point $\Phi(p)$ with angle α.

Given a conformal parameterization of the surface $S(x_1, x_2)$, we can define two functions on the domain D, the conformal factor function $\lambda(x_1, x_2)$ and the mean curvature function $H(x_1, x_2)$. If $\lambda(x_1, x_2)$ and $H(x_1, x_2)$ are given along with the boundary condition $S(u, v)|_{\partial D}$, $S(x_1, x_2)$ can be uniquely reconstructed [48]. This property translates to a compact representation for 3-D surfaces. A conformal mapping exists between a closed genus zero surface and a topologically equivalent unit sphere. Since a closed genus zero surface has no boundary, a registration criterion can be simply defined using (λ, H). Figure 3.1 shows the conformal mapping of the brain surface to a unit sphere with its geometric attributes (mean curvature and conformal factor) highlighted using a rainbow color map. In Figure 3.1(d), a checkerboard texture is mapped to the sphere using polar coordinates as the texture coordinates. Using the inverse conformal map the texture is transferred onto the brain surface, as shown in Figure 3.1(a). The angles at each edge of the white/black squares are preserved as needed. Figure 3.1(b) and 3.1(c) illustrate the mean curvature and logarithmic conformal factor color coded on the brain surface respectively. After the conformal mapping, the geometric attributes are similarly color coded on the sphere and shown in Figure 3.1(e) and 3.1(f). One observation worth noting is that the function value of conformal factor transits more gradually than that of mean curvature. This indicates that the conformal factor is a larger scale geometric feature when compared to the mean curvature.

3.2.2 Computing the Conformal Map: Harmonic Energy Minimization

A surface is most commonly represented as a mesh having a set of points and triangle faces, and is of arbitrary resolution. Since the conformal mapping is only dependent on the metric defined on the surface, it is invariant to its mesh triangulation. The spherical surface is curvature-constant and presents a simple canonical model for computing metrics. This property makes conformal mapping very appealing to a majority of matching and classification

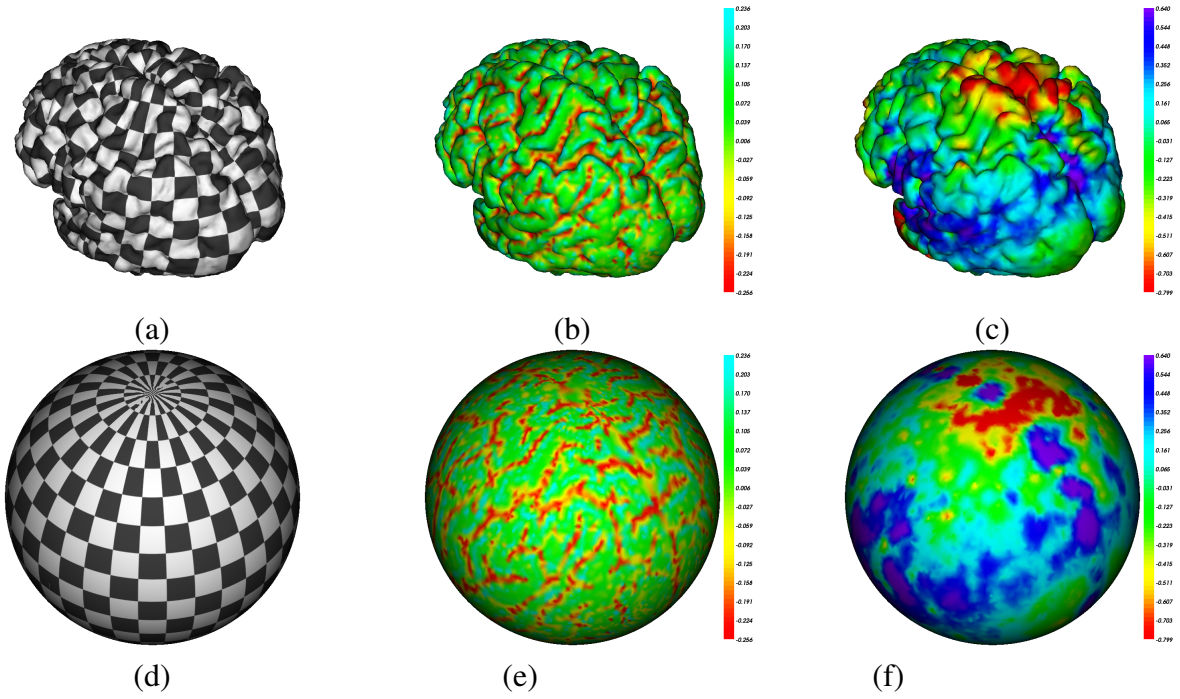

Figure 3.1: Spherical Conformal Mapping of Brain Surface. (a) The original brain surface with the texture induced by the conformal mapping from its spherical domain (d). The conformality is visualized by texture mapping of a checkerboard image. In (b) and (c), mean curvature and logarithmic conformal factor are color-encoded on the brain surface, respectively. (d) shows a sphere texture-mapped by a checkerboard using polar coordinates. (e) and (f) visualize the mean curvature function and the conformal factor function retained on the spherical domain.

problems. Conformal mapping ensures that the local geometries are preserved on the spherical surface. A surface matching between two parameterized canonical surfaces ensures a similar match between the corresponding surfaces in the native space. The goal is to compute the conformal map. As described in [48], two surfaces are conformal to each other if the mapping $f : M_1 \rightarrow M_2$ is harmonic. In other words, the harmonic energy is minimal when the mapping between surfaces is conformal. The energy functional is mathematically described as,

$$E = \int_M ||df||^2 dV, \tag{3.4}$$

where M is the manifold, df is the differential on f, and dV is the area on which the metric is induced.

We describe the procedure to formulate an alternate equation (3.4) for the discrete mesh surface. The mesh is described as a topological space called the simplicial complex $|K|$, which is a compact representation of the mesh. For example, a simplicial 2-complex consists of points, edges, and triangular faces. Based on the above definition, equation (3.4) can be rewritten in terms of the simplicial complex $|K|$ as,

$$E = \sum_{u,v \epsilon K} k_{u,v} ||f(u) - f(v)||^2, \tag{3.5}$$

where u and v denote the points, u, v denotes the edge linking u and v, and $k_{u,v}$ is the string energy. f is denoted by a piecewise linear function. Any edge u, v will have adjacent faces connected to it as shown in Figure 3.2. If α and β are the angles, and $k_{u,v}$ is given by,

$$k_{u,v} = A\frac{\cos(\alpha)}{Area_x} + B\frac{\cos(\beta)}{Area_y}, \tag{3.6}$$

the energy E is the harmonic energy. A and B are constants based on the mesh resolution. Since the function f is piecewise, the discrete Laplacian is defined as

$$\Delta f = \sum_{u,v \epsilon K} k_{u,v} ||f(u) - f(v)||. \tag{3.7}$$

The function f minimizes the harmonic energy if the tangential component of Δf is zero for every vertex in $|K|$. For a vector-valued function $\overrightarrow{f} = (f_0, f_1, f_2)$, the energy will be defined as the norm of $\overrightarrow{f}$:

$$E(\overrightarrow{f}) = ||\overrightarrow{f}||^2 = \sum_{0}^{2} ||f_i||^2. \tag{3.8}$$

Equivalently, the discrete Laplacian is defined as

$$\Delta \overrightarrow{f} = (\Delta f_0, \Delta f_1, \Delta f_2). \tag{3.9}$$

In a vector-valued setting, $\overrightarrow{f}$ is harmonic, if and only if the tangential component of the Laplacian is zero. This can be easily solved using the steepest gradient descent algorithm:

$$\frac{d\overrightarrow{f}(t)}{dt} = -\Delta\overrightarrow{f}(t). \tag{3.10}$$

As was explained in the previous section, we compute a conformal mapping $\overrightarrow{f} = M_1 \rightarrow$

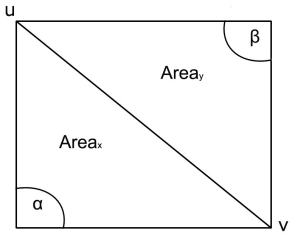

Figure 3.2: Edge u,v shared between two faces.

S^2 from the brain M_1 to the sphere S^2. This can be constructed using the steepest gradient descent method. However, this solution is not a unique solution and forms a Mobiüs group. Hence we fix the coordinate system using a zero-mass center constraint. This will restrict the conformal map to a 3-D euclidean rotation group. The orientation of the brain surface is explicitly assigned by manual selection of the coordinate points. Figure 3.8(c) explains the procedure to fix the coordinate system. We first locate the center of the brain as the midpoint of the line joining the Anterior commissure (AC) and Posterior commissure (PC). The AC-PC line is the first axis of dimension. The second axis is drawn perpendicular to the AC-PC line, and parallel to the mid-plane of the brain. The third axis is calculated as the cross-product of the first two axes. The axes are aligned to the world coordinate system through a rotation and is constrained during the conformal mapping procedure to ensure a unique map.

3.3 Creating the SCBM Template

3.3.1 Choosing the Standard Brain for Parameterization

There are two approaches for template brain selection. The selection will be used for subsequent creation of the SCBM template. In the first approach, a set of normal healthy brain data sets are selected from within the population used for the analysis. The brain data sets are averaged to create the template brain data set. The second approach is to randomly pick the best acquisition of a normal data set and use it as the template. The second approach is biased, subjective, and time consuming. We decided to use the brain atlas, the *ICBM*152 brain data set, provided by the International Consortium for Brain Mapping. The brain atlas has a general acceptance across the medical field and has been used as a template in many analysis studies. The *ICBM*152 brain data set can be downloaded from the following website, www.loni.ucla.edu/ICBM/Downloads/Downloads Atlases.shtml. This brain data set is an average of 152 adult human brains. Details on the development of the *ICBM*152 template is given in [36].

3.3.2 Landmark Feature Extraction

We define common landmarks that act as constraint priors for a robust alignment. The following set of nine cortical landmarks were defined (see Figure 3.3): (i) central, pre-central and post-central sulcus stretching from the midline to about 1cm superior to the sylvian fissure, (ii) parieto-occipital sulcus as defined in the midplane (iii) sylvian fissure stretching from the anterior edge of the brainstem to a virtual line connecting the inferior endpoints of the parieto-occipital and post-central sulcus, (iv) superior temporal sulcus reaching from the temporal pole to the above virtual line, (v) inferior temporal sulcus, (vi) transverse-occipital sulcus and (vii) superior frontal sulcus. This landmark set was chosen such that it consists of largely reproducible anatomical locations easily recognized in individual brains despite the inherent physiological variation among them. Moreover, this landmark set covers the lateral brain surface relatively uniformly, a crucial requirement for an accurate conformal mapping of the entire

cortical surface. Each landmark is a set of ordered points, which uses splines to create regular feature curves. These curves are uniformly reparameterized along their length to produce a dense point set representation. The reason for this will be clear when we introduce the thin-plate spline deformation in section 3.4.2.

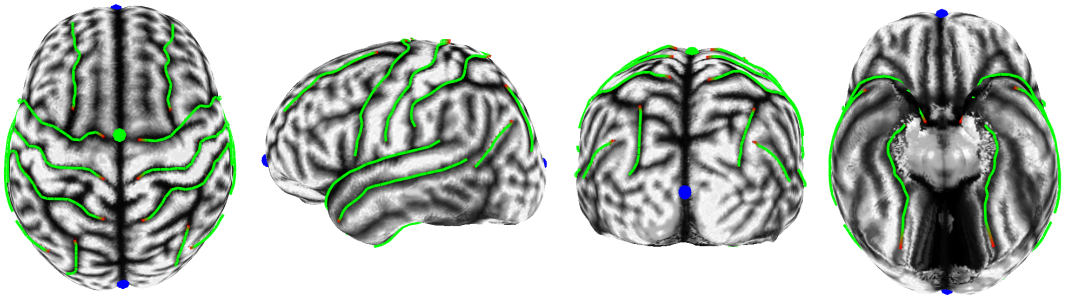

Figure 3.3: Definition of the cortical landmark set using the *ICBM*152 template brain. Only landmarks that can be reliably defined in all individual subjects were used. The following 9 landmarks were used: Central (C), pre-central (PreC) and post-central (PostC) sulcus, sylvian fissure (SF), superior (ST) and inferior temporal (IT) sulcus, superior frontal (SF) sulcus, parieto-occipital (PO) and transverse-occipital (TO) sulcus.

3.3.3 The SCBM Template

Figure 3.4 shows the parameterization of the *ICBM*152 brain template in the spherical domain. We refer to this spherical surface model as the Standard Conformal Brain Model (SCBM). The SCBM has a fixed orientation and is a unique conformal map defined for the *ICBM*152 data set. The orientation of the SCBM should be maintained for each individual subject before the inter-subject alignment algorithm is computed. This step is required to ensure that the global surface alignment is unique too. This orientation transformation follows the same protocol given in section 3.2.2, followed by a simple rigid rotation transformation and is trivial. After the orientation transformation the axes remains constrained during the optimization procedure.

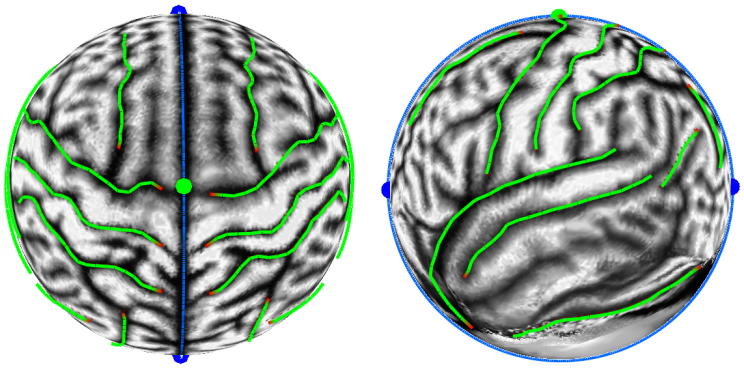

Figure 3.4: The Standard Conformal Brain Model (SCBM).

3.4 Inter-Subject Alignment of Brain Surfaces Using SCBM

In this section, we formulate the algorithm for a robust brain surface registration using the SCBM as the reference. The following sections briefly explain each step of the algorithm.

3.4.1 Parametric Registration

Parameterizing two surfaces to a common canonical domain naturally correlates their parametric coordinates. Suppose that M_1 and M_2 are two surfaces to be matched and its parameterizations are given by $\varphi_1 : M_1 \to \mathbf{R}^2$ and $\varphi_2 : M_2 \to \mathbf{R}^2$ respectively. The transition map $\varphi_2 \circ \varphi_1^{-1} : M_1 \to M_2$ defines a bijection - a one-to-one correspondence between M_1 and M_2. Given a matching criterion, the registration of 3-D shapes can be consequently defined as an automorphism μ in the parametric domain such that the transformation in the 3-D space can be formulated as $\psi = \varphi_2 \circ \mu \circ \varphi_1^{-1}$, whereby the matching error is minimized. Therefore, the 3-D shape registration is simplified to a 2-D image matching problem in the parametric domain and is more robust, accurate, and efficient. We call this matching framework the *parametric registration*. The 3-D shapes are represented as a vector-valued function $\vec{g}(x_1, x_2)$ defined on the domain D, where the function values are attribute vectors encoding the geometric information of the indexed local areas on the surface.

Landmark Constrained Conformal Mapping for Surface Alignment

We chose the SCBM as the parameterized reference shape for aligning individual brain surfaces. The landmarks are selected on each individual brain surface using the process described in section 3.3.2. The landmark curves are reparameterized to a dense point set representation to ensure that each curve has the same cardinality to its corresponding landmark curve defined on the SCBM. The next step is to derive the parametric registration that computes the individual brain conformal model (ICM) and aligns it with the SCBM. We use the same harmonic energy minimization step described in section 3.2.2 with an additional step for computing the automorphism. Intuitively, the automorphism μ generates a transformation matrix that aligns the landmarks on the ICM to the corresponding landmark in the SCBM. This is called the landmark constrained conformal mapping, because each landmark point on the ICM is constrained to align with its counterpart on the SCBM.

3.4.2 Non-Rigid Deformation Using Thin Plate Splines

Parametric registration computed using the landmark constrained conformal map may induce distortions during the matching process. There are unnatural stretching or squeezing at certain locations on the ICM, which is a direct consequence of the landmark constrained mapping. To prevent these distortions, the mapping is supplemented with a topology preserving non-rigid deformation technique that relaxes these distortions and ensures that the surface look natural. Many ideas were proposed for modeling the deformation of the surface. Thompson et.al. [118] modeled the deformation as an elastic viscous fluid equilibrium, which has only been solved on a planar domain. Joshi et al. [66] formulated a thin-plate spline warp in the parameter space of two square maps conceptually glued along the boundaries. The intrinsic geometry of the original surfaces is accounted for by using covariant derivatives. As no analytic solution exists, the optimum will be solved numerically. In [131, 13, 122], the registration of brain surfaces was conducted on a spherical parameter domain and is similar to our method. However, the underlying deformation model is fundamentally different. Moreover, these mod-

els were computed iteratively. We derived a spherical thin-plate spline model that is computed analytically and is more rigorous and efficient.

Thin-plate Splines: Theory

Thin-plate splines (TPS) are a class of widely used non-rigid interpolating functions, which has a closed-form solution as well as an intuitive physical interpretation. Because of its efficiency and robustness, TPS has been used extensively for smooth data interpolation and geometric deformation [13, 122, 126]. We employ TPS for an explicit matching of primary cortical structures on the spherical parameter domain, which serves as a nice basis for further refinement.

However, one major issue with TPS is that the conventional formulation is defined in the Euclidean space, which cannot be directly applied to the spherical domain. To ensure a smooth deformation on the spherical domain, the spherical analogue needs be explicitly redefined. Recently, the spherical extension of the traditional spline techniques has received increased attention [18, 53, 126]. Here we summarize the essential formulation of the spherical thin-plate splines (STPS). For full mathematical details and related deductions, refer to [126].

The thin-plate spline is the two-dimensional analog of the cubic spline in one dimension. The approach begins with an energy E that measures the quality of an interpolating function and finds a single function $u(x)$ that matches the given data points and minimizes this energy measure,

$$E = \int_{\Omega} \|Lu(x)\|^2 dx, \tag{3.11}$$

which is subject to the constraints that $u(p_i) = q_i$ for $i = 1, \ldots, M$. When $L = \nabla^2$ and $u(x)$ is viewed as the deflection orthogonal to the plane, the variational solution to Equation (3.11) is the TPS interpolation that models the configuration of the lowest physical bending energy of a thin plate. Instead of assuming that $u(x)$ corresponds to the lifting of the plate, we can apply this idea to the coordinate transformation. In the 2-D case, by using two separate thin-plate spline functions u_θ and u_ϕ which model the shifts of landmarks in each component, we arrive

at a vector-valued function $\vec{u}(\theta, \phi)$ specifying a 2-D transformation. The spherical analogue of the thin-plate bending energy functional defined by (3.11) in the Euclidean space has the form

$$J_2(u) = \int_0^{2\pi} \int_0^{\pi} (\Delta u(\theta, \phi))^2 \sin\phi d\theta d\phi, \tag{3.12}$$

where $\theta \in [0, \pi]$ is latitude, $\phi \in [0, 2\pi]$ is longitude, and Δ is the Laplace-Beltrami operator given by

$$\Delta u = \frac{1}{\sin^2\theta} u_{\phi\phi} + \frac{1}{\sin\theta}(\sin\theta u_\theta)_\theta. \tag{3.13}$$

To obtain a thin-plate interpolating spline on the sphere S^2, one needs to find a transformation $u \in H(S^2)$, an appropriately defined reproducing kernel (Sobolev) space of squared integrable functions on S^2, to minimize J_2 subject to

$$u(P_i) = z_i, \quad i = 1, 2, \ldots, n, \tag{3.14}$$

where $P_i \in S^2$ and z_i is the fixed value of P_i. Let

$$K(X, Y) = \frac{1}{4\pi} \int_0^1 \log h(1 - \frac{1}{h})(\frac{1}{\sqrt{1 - 2hz + h^2}} - 1)dh, \tag{3.15}$$

where $z = \cos(\gamma(X, Y))$ and $\gamma(X, Y)$ is the angle between X and Y. The solution has a closed form, given by

$$u_n(P) = \sum_{i=1}^{n} c_i K(P, P_i) + d, \tag{3.16}$$

where

$$\mathbf{c} = \mathbf{K}_n^{-1}[\mathbf{I} - \mathbf{T}(\mathbf{T}^T\mathbf{K}_n^{-1}\mathbf{T})^{-1}\mathbf{T}^T(\mathbf{K}_n^{-1})]\mathbf{z}, \tag{3.17}$$

$$d = (\mathbf{T}^T\mathbf{K}_n^{-1}\mathbf{T})^{-1}\mathbf{T}^T(\mathbf{K}_n^{-1})\mathbf{z}, \tag{3.18}$$

$$(\mathbf{K}_n)_{ij} = K(P_i, P_j), \tag{3.19}$$

$$\mathbf{T} = (1, \ldots, 1)^T, \tag{3.20}$$

$$\mathbf{z} = (z_i, \ldots, z_n)^T, \tag{3.21}$$

in which $\mathbf{K}_n$ is the $n \times n$ matrix with its (i, j)th entry $(\mathbf{K}_n)_{ij}$.

Given the displacements $(\Delta\theta_i, \Delta\phi_i)$ of a set of points $\{P_i\}$ on the sphere in spherical coordinates, the STPS can be used to interpolate a deformation map $S^2 \to S^2$ that is consistent with the assigned displacements at $\{P_i\}$ and smooth everywhere with an imposed minimization of J_2. Let $\{P_i = (\theta_i, \phi_i)\}_{i=1,\ldots,n}$ be the n points with known one-to-one correspondences to another set of points $\{Q_i = (\theta_i', \phi_i')\}_{i=1,\ldots,n}$:

$$(\theta_i, \phi_i) \to (\theta', \phi') = (\theta_i + \Delta_\theta, \phi_i + \Delta_\phi). \tag{3.22}$$

Each component of the displacement $(\Delta\theta_i, \Delta\phi_i)$ can be treated as a scalar value at $P_i(\theta, \phi)$ separately. Therefore we obtain

$$u_\theta(P_i) = \Delta\theta_i, \quad i = 1, \ldots, n \tag{3.23}$$

and

$$u_\phi(P_i) = \Delta\phi_i, \quad i = 1, \ldots, n, \tag{3.24}$$

which is similar to Equation(3.14). Computing the corresponding smoothing functions $u_\theta(P)$ and $u_\phi(P)$ are straightforward, where two separate STPS functions are involved. The resulting automorphism $S^2 \to S^2$ for each point $P \in S^2$ is given as,

$$P(\theta, \phi) \to P(\theta + u_\theta(\theta, \phi), \phi + u_\phi(\theta, \phi)). \tag{3.25}$$

This global deformation field $(u_\theta(\theta, \phi), u_\phi(\theta, \phi))$, determined by the STPS, is optimal in the sense that it minimizes the TPS deformation over a spherical domain, which is invariant under

arbitrary rotations of landmarks.

Surface Deformation using Curve Constraints

The formulation of the Spherical TPS describes the deformation of a spherical image constrained by a set of point-based interpolants. As described in section 3.3.2, landmarks features on the brain are essentially geometric curves. To deal with curve landmarks, we adjust the formulation of the spherical TPS to deal with curve constraints. The condition of the STPS is rewritten as,

$$u(C_i(t)) = z_i(t), \quad i = 1, \ldots, n, \quad t \in [0, 1], \tag{3.26}$$

where $C_i(t)$ is the ith control curve, with a corresponding target curve located at $z_i(t)$, both of which are parameterized by t. It follows from Equation (3.16) that

$$u_n(P) = \sum_{i=1}^{n} \int_0^1 C_i(t) K(P, P_i(t)) + d, \tag{3.27}$$

If each curve is converted to a set of dense points, $C_i(k)$ $(k = 0, \ldots, N_i)$, and supposing each $C_i(k)$ has a corresponding sampled value $z_i(k)$, and we treat $C_i(k)$ as a single point, Equation (3.16) is still valid for spline curves. $\mathbf{c}$ has to be modified to

$$\mathbf{c} = (C_1(0), \ldots, C_1(N_i), \ldots, C_n(0), \ldots, C_n(N_n))^T \tag{3.28}$$

and $\mathbf{z}$ to

$$\mathbf{z} = (z_1(0), \ldots, z_1(N_i), \ldots, z_n(0), \ldots, z_n(N_n))^T. \tag{3.29}$$

Accordingly, the previous square matrix K_n is now a $(\sum_{i=1}^{n} K_i) \times (\sum_{i=1}^{n} K_i)$ matrix, given by

$$\mathbf{K} = \begin{pmatrix} \vdots & & \\ \dots & K_{N_i \times N_j} & \dots \\ \vdots & & \end{pmatrix} \tag{3.30}$$

where the $K_{N_i \times N_j}$ is a sub-block matrix in which

$$K_{N_i \times N_j}(p, q) = K(C_i(p), C_j(q)). \tag{3.31}$$

Figure 3.5 shows the result of the STPS deformation on the spherical surface using the feature curves. Figure 3.5(c) is the result of deforming the surface in Figure 3.5(b) to the template, Figure 3.5(a). To ensure one-to-one correspondence between the curves defined on the two surfaces, the point sets for each corresponding curve has the same cardinality. The order of the feature curves delineated on the template and the subject should be homologous and parameterized on the domain [0,1]. Figure 3.5 shows an orthogonal grid on top of the spherical images to highlight the deformation that takes place during the alignment of the landmark features.

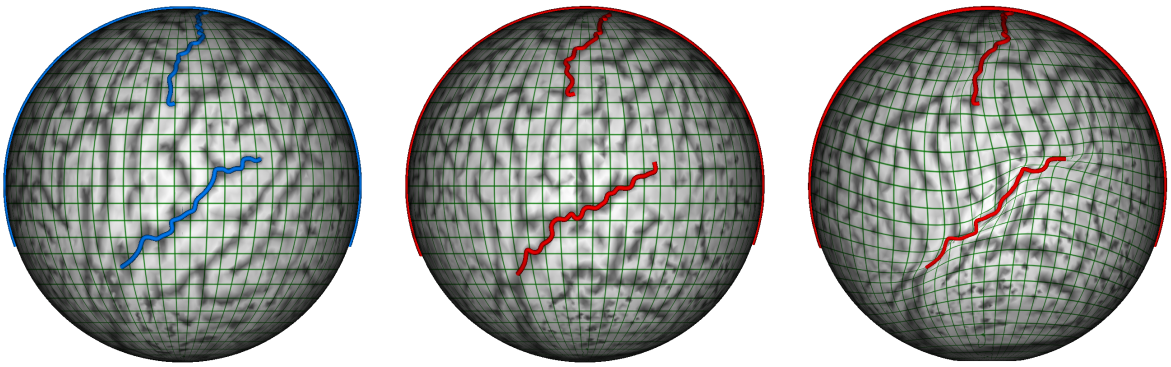

(a) (b) (c)

Figure 3.5: Non-rigid feature registration under the STPS deformation. (a) is the spherical domain of the template. (b) shows the domain of the subject. (c) shows the effect of STPS deformation performed on (b).

3.4.3 Compound Optimization

The parametric registration and the STPS deformation field aligns the landmarks given two surfaces, S_1 and S_2, and reduces the distortions induced during transformations within the spherical domain. The deformation does not ensure that the surface area in-between the landmarks are aligned correctly. To further align the anatomy of the two brain surfaces in between the various landmarks, we define the following metric in the shape space based on the conformal factor $\lambda(u, v)$ and mean curvature $H(u, v)$ as

$$d(S_1, S_2) = \int_{S_2} ((\log \lambda_1(u, v) - \log \lambda_2(u, v))^2 + (H_1(u, v) - H_2(u, v))^2) d\mu, \tag{3.32}$$

where the $d\mu$ is the area element of the unit sphere S^2. This nonlinear optimization procedure based on the Newton-Raphson method minimizes the distance functional and aligns the surface shapes and the registration is assumed to be complete. During the minimization of the distance functional, local topology should be maintained. In other words, the conformality in the spherical space should be maximum. This requirement can be enforced by adding the harmonic energy operator to the distance functional. The optimization displaces each vertex in the tangential space of the sphere, thus maintaining the topology of the surface at all times.

3.4.4 The Surface Matching Algorithm

The complete algorithm for brain surface matching is summarized as follows:

1. Create the brain surface B_1 and select the landmarks q_i
2. Run the landmark constrained conformal mapping (Section 3.4.1) to compute the initial alignment of the ICM to the SCBM.
3. Run the STPS deformation model (Section 3.4.2) to relax the distortions induced by the conformal map.

4. Run the compound optimization procedure (Section 3.4.3) to align the brain anatomy in-between the landmarks.

3.5 Unit of Analysis: Surface ROI Mesh

The previous section explains the formulation of the algorithm for accurate global alignment of two brain surfaces in the parametric domain. Because the transition map is bijective, each point on the canonical sphere will map to the homotopic point in the native brain surface. In other words, the global alignment ensures that surface-based statistics will be free of localization error, a clear advantage over VBM.

The next step is to generate the analysis unit for computing statistics. The goal of our research is to provide a system where significant features can be quantified across the entire brain using statistical models. Since functional brain activity data is mostly high-dimensional unstructured data, to generate meaningful statistics we have to define a structural basis to extract meaningful features. These structural analysis units encompass the whole brain and define anatomical vantage points. These units are large enough to generate a meaningful quantity, and small enough to be perceivable anatomically across the brain. Generating these meaningful basis elements is extremely challenging in the native space due to the brain's convoluted topology. However, its spherical counterpart is curvature-constant, which makes it very easy to derive a homotopic structure across multiple brain surfaces. We define a fractal subdivision scheme to determine a regular configuration of multiresolution cortical surface elements. Because the transition map is bijective, the elements are easily mapped back to the native space and guaranteed to be homotopic. These finite number of multi-resolution elements form a mesh around the brain surface and termed as the **Surface ROI mesh**. Each triangular element in the mesh will represents a unit of analysis for quantifying the brain activity feature extracted from either a functional or a structural modality.

3.5.1 Procedure

As shown in Figure 3.6, at the top level, the sphere is divided into eight spherical triangles corresponding to the eight quadrants. For the next level of detail, the midpoint of the edges in each triangular patch from the previous level is marked and connected along the arc of the great circle to form an encapsulated triangle. The number of triangles (t_k) at each level (k) can be calculated as $t_k = 8 \times 4^k$. Defining the cortical elements in this way ensures a non-overlapping subdivision of the surface such that each surface point belongs to exactly one cortical element. In addition, the elements are efficiently indexed using a hierarchical quad-tree data structure [112]. Figure 3.7 shows the Surface ROI mesh at the resolution level 3, which was empirically found to be the practical resolution for most statistical analysis models with regards to the spatial accuracy and noise sensitivity. One of the cortical elements in the figure is highlighted in blue.

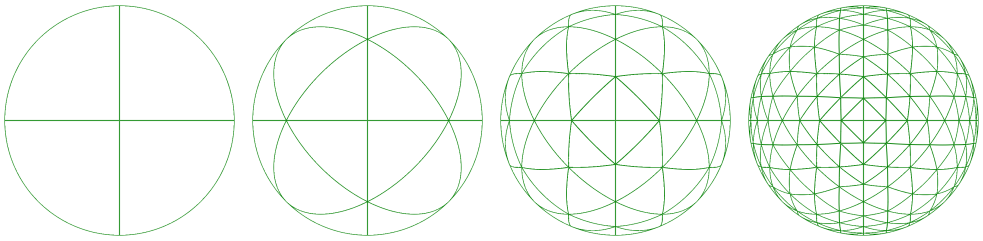

Figure 3.6: Fractal spherical subdivision. (a) Level = 0; (b) Level = 1; (c) Level = 2; (d) Level = 3. Starting with the eight quadrants of the sphere at level 0, the midpoint of edges are connected in each surface triangle generating the next level of parcellation.

3.6 Example: Real Brain Data Set

Figure 3.8 and Figure 3.9 illustrates the entire procedure for mapping a brain dataset to the template (SCBM) and the subsequent creation of the *surface ROI mesh*. The brain surface (Figure 3.8(a)) was generated using an in-house software application implemented based on the marching cubes algorithm. Any surface generator will work that outputs a surface of closed topology. The software application also provides an interactive tool to select the landmark

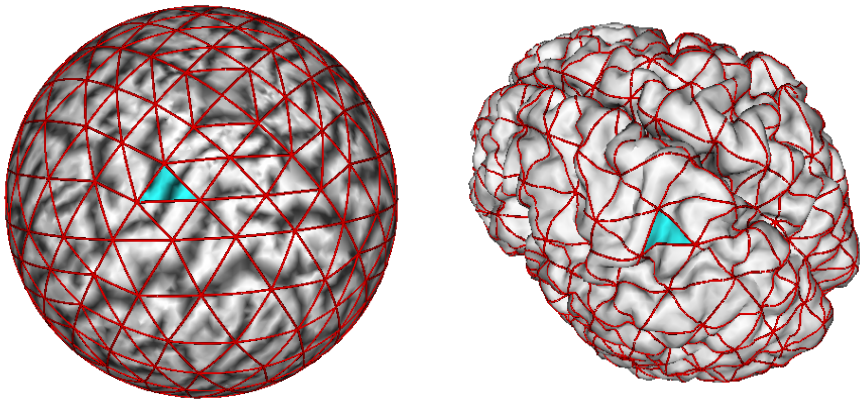

(a) (b)

Figure 3.7: Finite cortical elements defined in the native space of individual brains. (a) shows the spherical parameter domain is first regularly parcellated based on fractal subdivision method. Each cell is then reversely mapped back to the native space of the brain, forming a set of cortical elements, as shown in (b).

features. An expert neuroanatomist selects the landmarks using the specifications given in section 3.3.2. The orientation of the brain in fixed using the procedure explained in section 3.3.3 and illustrated in Figure 3.8(c). A rigid transformation is calculated to align the orientation axes with that of the SCBM. This initial rigid alignment will be constrained along with the other landmarks during the optimization.

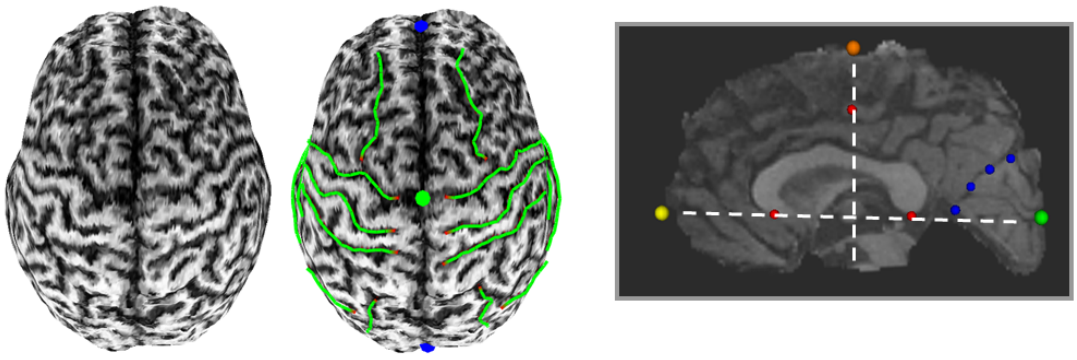

(a) (b) (c)

Figure 3.8: (a) shows an individual brain subject. (b) shows the brain with the landmark features. (c) shows the procedure to fix the orientation of the brain.

Figure 3.9 illustrates the steps to create a homotopic *surface ROI mesh* encompassing the

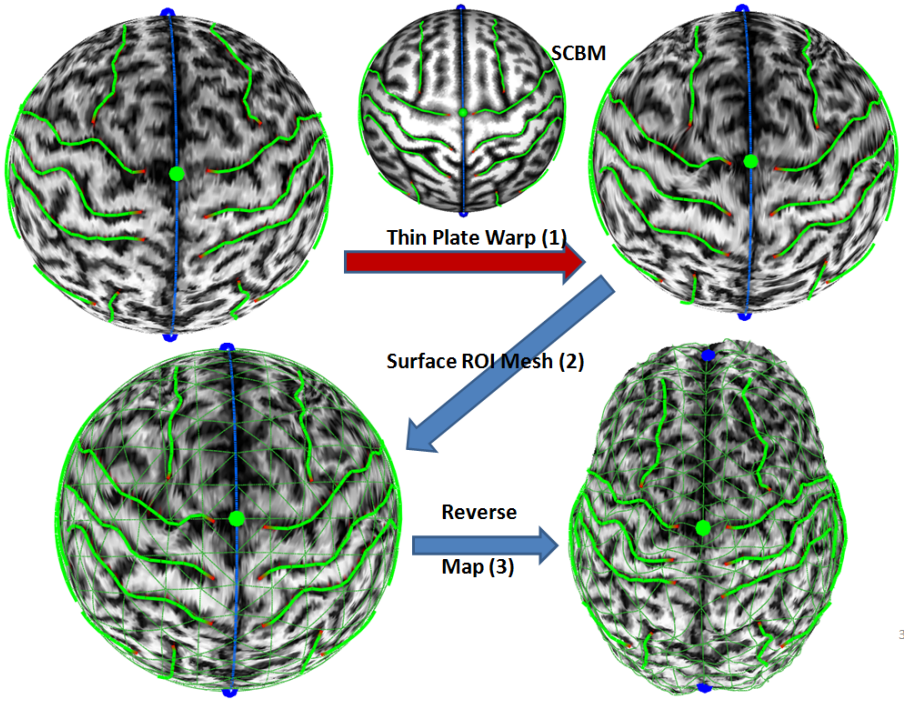

Figure 3.9: Framework for global alignment and generating the surface ROI mesh for an individual subject. Each triangular element represents an homotopic ROI for generating statistics.

brain surface. The brain surface in Figure 3.8(a) is initially mapped to a unit sphere. As described in the section 3.4.1, the landmark curves on the brain are reparameterized to a dense point-set representation. Initially, because of the rigid alignment these points are assumed to be very close to each other. The landmark curves defined on the SCBM represents the target landmarks, denoted as p_i. After the parametric registration and the STPS deformation the landmarks on the subject brain q_i will be aligned to its counterpart p_i on the SCBM. This is defined as step 1 in Figure 3.9. Step 2 creates the Surface ROI mesh at resolution level 3, which is equal to 512 unique cortical element ROIs. Finally, in step 3 the inverse map will transfer the *surface ROI mesh* onto the original brain surface. At the end of the three steps we have a *surface ROI mesh* designed for whole-brain analysis. The triangular elements are biologically relevant and can be grouped together and labeled based on the predefined anatomical or functional boundaries.

Figure 3.10 illustrates the creation of homotopic *surface ROI meshes* in two individual sub-

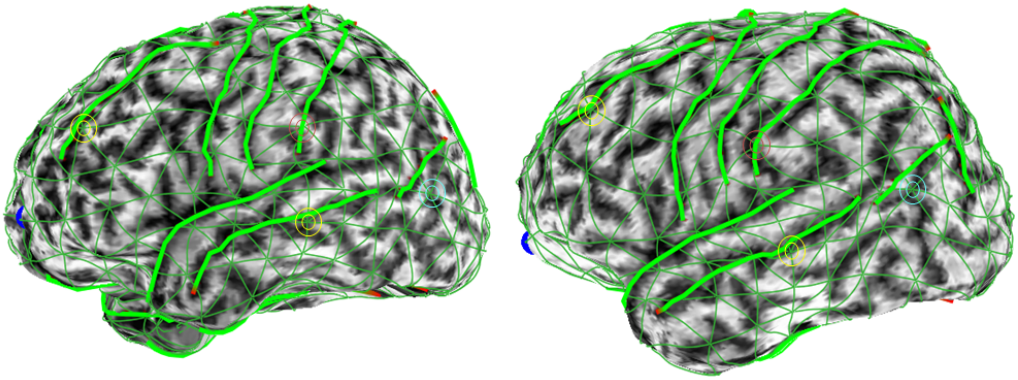

(a) (b)

Figure 3.10: (a) and (b) are two individual brain surfaces shown after the global alignment to the SCBM. The surface ROI mesh is marked at various points. These points allow the user to visually inspect the alignment.

ject brains. Although the shape and location of the triangular ROI elements differ between the two brains in native space, each ROI element is characterized by the same spatial relationship to its own cortical landmarks. Each ROI element will be mapped to the same location on the canonical sphere.

The computational complexity at the various stages of our alignment framework are listed as follows. The surface generator using the marching cubes algorithm took around 30 minutes to process, starting from the deskulling of the 3-D MRI image. The landmark estimation is done manually and depending on the operator expertise took around $15 - 20$ minutes. The global surface alignment to the SCBM took an average of 25 minutes. The *surface ROI mesh* at resolution level 3 was generated in 2 minutes.

3.7 Volumetric Conformal Mapping

The SCBM based registration is very effective for analyzing brain disorders that affect the cortical surface. We extend the SCBM algorithm to also include mapping of brain subcortical structures. This represents the Volumetric Conformal Mapping (VCM) algorithm for volumetric matching of brain volumes. Most of the the requirements for VCM are the same, but the treatment is slightly different because the parametric dimension increases by one. First,

the brain volume is represented as a tetrahedral mesh. The brain mesh is still of genus zero topology and the topologically equivalent canonical domain is represented by a solid ball. The tetrahedral brain mesh is shown in the Figure 3.11(a). The goal is to find a conformal map to the solid ball shown in Figure 3.11(d). The procedure starts with the creation of the SCBM. Once the SCBM is computed, the surface conformal map is fixed and we optimize the variational equation for harmonic energy minimization to the mesh structure enclosed within the surface [130]. This step is computationally intensive because of the increased resolution. The VCM model looks similar to the SCBM except that its a tetrahedral volume as shown by the cutout in Figure 3.11(e). The textured slice shown in Figure 3.11(c,f) shows that the geometry is preserved after the volumetric conformal mapping too.

To summarize, the steps required for the volumetric conformal mapping is listed below:

1. Create the brain surface B_1 and select the landmarks q_i
2. Run the landmark constrained conformal mapping (Section 3.4.1) to compute the initial alignment of the ICM to the SCBM.
3. Run the STPS deformation model (Section 3.4.2) to relax the distortions induced by the conformal map.
4. Run the compound optimization procedure (Section 3.4.3) to align the brain anatomy in-between the landmarks.
5. Constraining the surface map compute the variational equation for harmonic energy minimization for the mesh structure enclosed within the surface.

3.7.1 Volumetric Matching of a Subject Brain to the VCM

For matching of brain volumes we start with an initial mapping of the brain surface to the SCBM. Once the surface mapping is completed, the surface map is fixed, and the algorithm proceeds with a surface constrained conformal mapping for registration of the brain volumes.

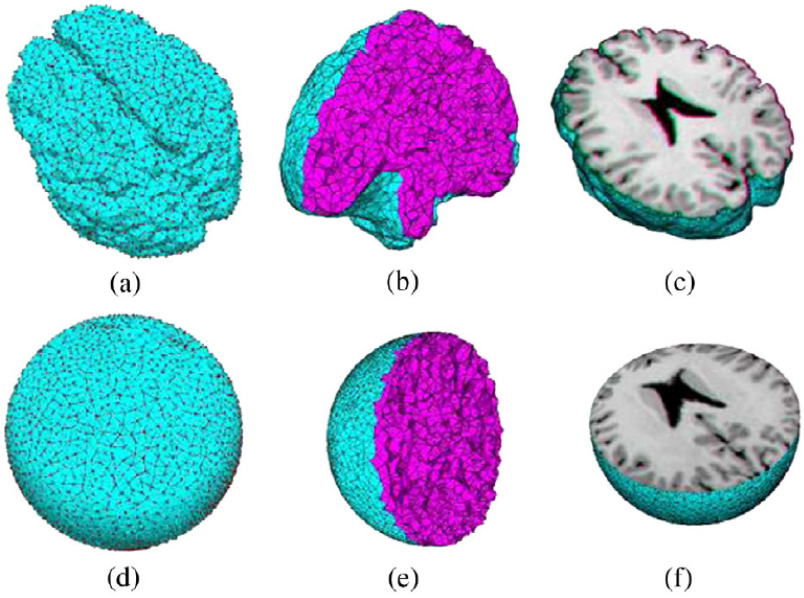

Figure 3.11: An illustration of conformal mapping applied to the brain: (a) tetrahedral mesh equivalent of the brain volume; (b) internal mesh structure; (d) the solid ball created by volumetric conformal mapping; (e) internal structure of the brain after conformal mapping; (c),(f) interpolated slices which show that the conformal mapping preserves the brain geometry.

In the volumetric case we choose the surface boundaries of internal structures as the landmarks for constrained optimization. Some of the landmarks chosen for optimization are the corpus callosum, the pons, the anterior and the posterior commissure, and the cingulate. These structures are prominently visible in brain MRI images and can be segmented very easily using well-known segmentation algorithms. Harmonic energy minimization for the internal mesh structure is numerically solved until the volumes are registered. Since the internal structures are not as physiologically variable as the cortical surface, we found that there was no need to include a deformation function during matching. The volumetric alignment algorithm took an average of 45 minutes to compute.

3.8 Statistical Assessment of Spatial Accuracy

To assess the spatial accuracy of the *surface ROI mesh*, we develop two separate approaches: a quantitative approach that yields a measure of local displacement error at each

vertex point of the *surface ROI mesh*, and a semi-quantitative approach that evaluates the spatial relationship between finite cortical elements and the surface landmarks when compared to the localization ratings given by expert neuroanatomists.

3.8.1 Quantitative Assessment of Spatial Accuracy

To calculate the local displacement error, the 512 vertices's that define the *surface ROI mesh* of each individual brain were transferred into *ICBM*152 template space. As the vertices's have different distances to landmark points (for which the transformation is exact), they show a slight displacement among the subjects. In order to quantify the local displacement, we determined the displacement error (DE) in each vertex point (r_i) as,

$$DE = \frac{1}{N}\sum_{i=1}^{N} |\overrightarrow{r_i} - \overrightarrow{r_L}|, \tag{3.33}$$

where r_L represent the location of the vertex in template space and N is the total number of vertices's. The DE values were subsequently rendered on the cortical surface by means of a Gaussian distribution with $1cm$ full-width at half maximum $(FWHM)$ and allowed quantitative assessment of local spatial accuracy (Figure 3.12(a) and Figure 3.12(b)). The DE was determined independently for the adult and the pediatric control groups and for five anatomical territories (frontal, temporal, parietal, occipital and central). In order to determine whether the DE measures differ between the groups or territories, a $2 \times (2 \times 5)$ repeated measures ANOVA was applied, where the between-subjects factor represents the group and the two within-subjects factors represent the hemispheres (L/R) and anatomical territories (5 levels).

3.8.2 Qualitative Assessment of Spatial Accuracy

The *surface ROI mesh* will be accepted in clinical routine if the results correspond well with the readings of an expert observer. To assess the accuracy of the *surface ROI mesh* against an expert rating, seven anatomically locations (the inferior and superior frontal gyrus, pre-central and post-central sulcus, superior and anterior-inferior temporal gyrus, parieto-occipital fissure)

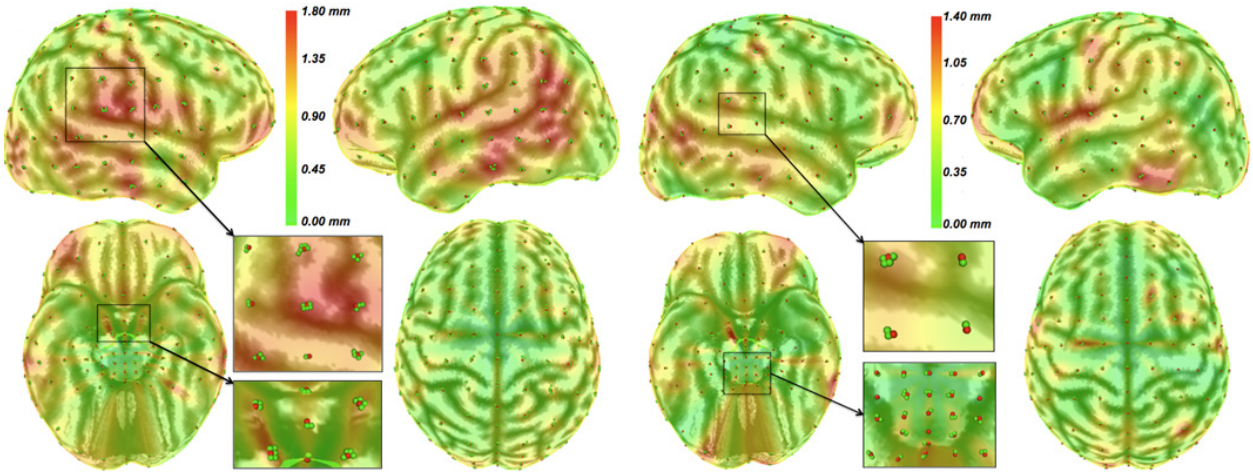

(a) (b)

Figure 3.12: Local displacement error in the adult (a) and pediatric (b) group rendered onto the template brain. The displacement error is calculated in each vertex point for the two groups and the average displacement error is then displayed on the cortical surface. The inserts show local spatial clustering of vertex points derived from individual subjects (green) of each group and the corresponding template points (red). Average displacement values were found to be $< 2mm$, with the largest displacement being detected in the temporal lobe.

per hemisphere were defined in the template brain by selecting a set of finite cortical elements (see Figure 3.13 (top row)). The indices associated with the selected finite cortical elements were recorded and corresponding finite cortical elements were then determined in native space of normal subjects. Subsequently two expert observers reviewed independently the location of all anatomical territories in both the adult and pediatric groups at two separate occasions (2 days apart, altered presentation sequence). Visual agreement between the template and native space locations was evaluated according to a 4-point score (4 = complete alignment, 3 = minimal misalignment, 2 = noticeable misalignment, 1 = substantial misalignment), yielding a total of 140 scores per session. In addition to a descriptive analysis, we applied a $10 \times (2 \times 7)$ repeated measures ANOVA, where the between-subjects factor represented the individuals and the two within-subjects factors were the hemisphere (L/R) and the anatomical location (7 levels).

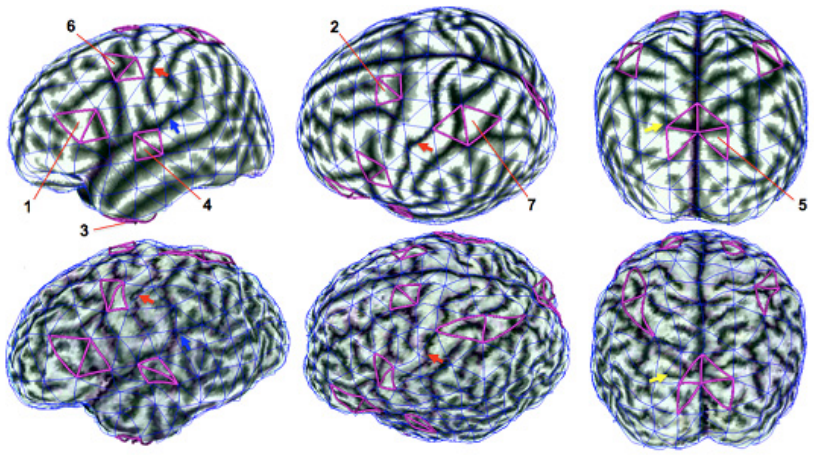

Figure 3.13: Anatomical locations used for agreement scoring. Template brain (top row) with the following locations: 1 inferior frontal gyrus, 2 superior frontal gyrus, 3 anterior-inferior temporal gyrus, 4 superior temporal gyrus, 5 parieto-occipital fissure, 6 pre-central sulcus, 7 post-central sulcus. Corresponding locations in native space of a representative subject (bottom row). As the cortical topology differs between individual subjects, spatial agreement between the template and native space was assessed based on the spatial proximity to major anatomical landmarks such as the central sulcus (red arrow), sylvian fissure (blue arrow) and transverse-occipital sulcus (yellow arrow).

3.8.3 Quantitative Evaluation of Displacement Error

Figure 3.12 shows a surface rendering of the displacement error in atlas space for both adult (Figure 3.12(a)) and pediatric (Figure 3.12(b)) control subjects. In general, the displacement error was higher in adults as compared to pediatric subjects (main group effect $p < 0.001$), although the absolute displacement was less than $2mm$ in both groups. Table 3.1 reports the average displacement in each of the 5 anatomical territories. No L/R differences were determined in either group. The displacement error was significantly different between anatomical territories ($p = 0.005$) and was found to be the largest in the temporal lobe.

3.8.4 Agreement Score Assessment

The average overall agreement score characterizing the spatial agreement between anatomical locations in template and native space was found to be between 3.23 and 3.89, dependent on the anatomical location (see Table 2). Almost $2/3$ (62%) of all locations were judged as completely aligned and only 2% were found to show noticeable misalignment, with the re-

Table 3.1: Mean displacement error (+SD) determined in five anatomical territories for both the adult and pediatric groups.

		Displacement(mm) Adults	Pediatric
Frontal	L	0.52 (0.07)	0.36 (0.05)
	R	0.59 (0.10)	
Central	L	0.57 (0.11)	0.47 (0.10)
	R	0.66 (0.10)	
Temporal	L	0.70 (0.16)	0.52 (0.10)
	R	0.67(0.17)	0.55 (0.08)
Occipital	L	0.46 (0.15)	0.40 (0.10)
	R	0.50 (0.16)	0.41 (0.08)
Parietal	L	0.62 (0.11)	0.50 (0.10)
	R	0.64 (0.13)	0.54 (0.11)

maining 36% of locations being judged as slightly misaligned. There was no difference in agreement score between the two hemispheres, however a significant main effect with respect to the location of anatomical regions was detected ($p = 0.005$). Regions at inferior frontal (1, see Figure 3.13), superior frontal (2), superior temporal (4) and pre-central (6) locations showed on average very high agreement scores (3.73–3.91), whereas scores for the post-central (7), parieto-occipital (5) and anterior-inferior temporal (3) location were somewhat lower (3.32–3.65). Figure 3.13 shows a representative image of the location of finite elements in the template and a subject. It can be seen that in general all regions align well with major cortical landmarks (such as central sulcus and sylvian fissure), even though regions that were scored lower $(7, 5, 3)$ are slightly distorted. There was no significant difference in overall readings between the adults and pediatric subjects (Table 3.2).

3.9 Summary

In this chapter, we explain the methodology for global surface alignment of individual brain data sets. The algorithm was mathematically formulated and illustrated with an example brain

Table 3.2: Average score (4.0 = best, 1.0 = worst) in 7 anatomical locations (see also Figure 3.13). The table shows the average scores obtained from two expert neuroanatomists who evaluated the images on two separate occasions.

		Average Score	
		Adults	Pediatric
Inf Frontal	L	3.77 (0.05)	3.88 (0.12)
	R	3.75 (0.14)	3.78 (0.09)
Sup Frontal	L	3.91 (0.11)	3.77 (0.15)
	R	3.76 (0.21)	3.80 (0.13))
Inf Temporal	L	3.40 (0.20)	3.38 (0.10)
	R	3.59 (0.12)	3.43 (0.08)
Sup Temporal	L	3.80 (0.20)	3.68 (0.13)
	R	3.73 (0.10)	3.79 (0.18)
Occipital	L	3.43 (0.32)	3.49 (0.14)
	R	3.65 (0.19)	3.36 (0.08)

data set. The main goal for the global surface alignment was to define a anatomical basis for conducting accurate whole brain surface analysis studies. The surface based registration guarantees accurate localization of anatomic vantage points defined by finite multi-resolution cortical elements. This cortical element set is termed as the surface ROI mesh and forms the smallest analysis unit for quantifying features. Finally, we extend the surface alignment algorithm for registration of brain volumes. After the surface map is fixed, the algorithm proceeds with the computation of the internal map. The volumetric registration allows for the analysis of internal structures, especially for quantifying the micro-structural properties of the brain white matter tissue, as will be described in chapter 4. The SCBM-based and VCM-based registration algorithms were published in [94], and the NeuroImage journal [93], respectively.

CHAPTER 4

SCIENTIFIC VISUALIZATION SOLUTIONS FOR SCBM-BASED QUANTITATIVE CROSS-SUBJECT IMAGE ANALYSIS

The previous chapter mostly dealt with the creation of a spatial environment that accurately maps anatomical locations across multiple brain data sets. An explicit geometry-based solution was developed for computing the global alignment of individual brain data sets. The principal reason for undertaking this step was to generate a systematic ROI mesh structure encompassing the brain for pooling features from multiple functional and morphological data sources. The absence of a spatial bias allows analyst's to accurately employ statistical models to test for significant feature patterns that correlate with abnormal behavior. Having an ordered basis rooted in the anatomy not only helps visualize the results in the global space but also provides enough latitude for local control and focus on specific regions of interest.

In this chapter, we focus on the development of quantifiable experiments and qualitative studies for analyzing the significance of features extracted from multiple image modalities. We begin the chapter with a brief overview of the various image modalities used in our experiments and the protocol used for each image acquisition. The latter sections will concentrate on the development of cross-subject analysis experiments for each modality and provide a detailed discussion of the quantification results. For each experiment, scientific visualization tools play a prominent role for the reliable creation and display of the features in the 3-D spatial context and to confirm the significance of the analysis results. Visualization tools supplement the analysis with the effective presentation of information that help scientists make insightful conclusions about brain behavior.

4.1 Image Modalities

4.1.1 Magnetic Resonance Imaging (MRI)

Magnetic resonance imaging is a medical imaging technique mostly used in radiology because of its ability to visualize the internal structures of the body in detail. The general approach to acquire MRI images is to excite the nuclei of the molecules within the tissue structures using a powerful magnet. The radio frequency fields alter the alignment of the nuclei within the magnetization and generates a rotational field that is detected by the scanner. Different tissue structures excite differently to the RF field and produce the necessary contrast for differentiating tissue structures in the body. The MRI produces a very good contrast between different soft tissues, making it especially useful for imaging the brain. Depending on the type of magnetization used, the gradient of the RF field, and the rotational spin recorded by the scanner, there are a bunch of different MRI-based scans available. Some examples include the T1-weighted MRI that measures the spin-lattice relaxation time, the T2-weighted MRI that measures the inverse contrast to the T1-weighted MRI, $T2^*$-weighted MRI for increasing the contrast of blood, and other variants.

Acquisition Protocol: For our analysis, we used T1-weighted images acquired in the coronal plane using a 3-D inversion recovery (IR) spoiled gradient echo (SPGR) sequence with a TR/TI/TE=7.6/1.7/500 ms, ip angle=20, field of view (FOV)=$200mm \times 200mm$, matrix size=256×256, pixel size=$0.781mm \times 0.781mm$, and slice thickness=$2.0mm$. All T1-weighted images were rotated to the axial orientation to visualize the 3-D image in radiological convention.

4.1.2 Positron Emission Tomography (PET)

Positron emission tomography is a 3-D image acquisition technique that produces a volume image of the functional processes in the body. A gamma ray-emitting tracer is introduced in the body, which reacts with the biologically active molecule. A 3-D image of the tracer concentration at each point in the body is reconstructed by computer analysis to create the PET

image. In our analysis, we use the FDG tracer, which is an analogue of glucose and measures the metabolic activity. The PET image reflects the regional glucose uptake across the brain volume.

Acquisition Protocol: PET studies were performed using the CTI/Siemens EXACT/HR scanner (Knoxville, TN) with a reconstructed image resolution of about $5mm$ full width half maximum (FWHM). Subjects were not allowed to eat for at least four hours prior to the PET-imaging procedure and static FDG PET images were obtained based on coincidence data acquired between 40–60 $minutes$ after tracer injection. The PET image volumes are coregistered to the T1-weighted MRI image using an in-house registration tool. Any rigid registration algorithm is suitable for this task. After the registration, the PET and the MRI occupy the same physical space.

4.1.3 Electroencephalography (EEG)

Electroencephalography is the recording of the electrical activity either on the intracranial brain surface or the scalp. When the neurons in the brain get excited, voltage fluctuations, which are recorded by the EEG, are generated. EEG is the most preferred diagnostic application for localizing seizure onset focus in epilepsy. Sometimes, EEG may also be used for diagnosing brain tumors, stroke, or other focal brain disorders. A secondary application of EEG is for the diagnosis of coma or brain death. The EEG modality is not a typical 3-D image. Rather, it is a recording of the electrophysiological activity at electrode channels implanted at various locations on the brain, also known as EEG grids.

Acquisition Protocol: For our analysis, we implant intracranial EEG grids that record electrical activity for at least 24 hours. From the activity data, we label the electrodes into three categories: the seizure onset, the seizure spread, and the normal. For each electrode, we retrieve the interictal spike profile in between two seizure events. These spike profiles measure the frequency, amplitude, duration, and slope of the spike.

4.1.4 Diffusion Tensor Imaging (DTI)

Diffusion tensor imaging is a variant of the MRI technique and measures the diffusion of water molecules in biological tissue. The water molecules around the tissue restrict its movement in the direction of the neural fiber bundles. It is the most preferred modality for visualizing the structural organization of white matter microstructure. This MRI technique measures the diffusion with the sole intent of reconstructing neural fiber tracts within the tissue. As the name suggests, the DTI defines a tensor at each voxel in the 3-D image. To acquire the diffusive properties from the scanner, different diffusion-sensitizing gradients are applied to the RF field in different orientations. At least six diffusion-weighted images are required to calculate the diffusion tensor, but the current practice dictates at least 30 unique diffusion-weighted images. Having a higher number increases the SNR of the acquisition and improves the angular resolution resulting in an improved 3-D fiber reconstruction.

Acquisition Protocol: The DTI data were acquired in the axial plane using 25 non collinear weighting directions and a single-shot echo-planar imaging (EPI) sequence with a b-value of $1000s/mm2$. Each volume covered a $240mm \times 240mm$ field of view with $0.9375mm \times 0.9375mm$ in-plane resolution and $2.6mm$ slice thickness with no interslice gap.

4.2 Visual Analysis of Image Features Across Subjects

In this section, we list some of the analysis results for localizing brain disorders in space via quantification of the brain activity features. For each analysis study, we briefly explain the disorder and the hypothesis that is being tested. The analysis is supplemented by scientific visualization tools that will assist the scientist to load the data, extract and process the features from the data, and compute the cross-subject analysis results. A rendering display will present the final results in the reconstructed 3-D physical space, allowing the scientist to gain insight and provide visual confirmation of the statistics.

4.2.1 Quantitative Assessment of Cortical Surface Abnormality Using PET

Individuals that suffer from epileptic seizures have a noticeable effect on the tissue metabolic activity along the cortical surface. Research studies in epilepsy suggests that patients with a strong seizure focus have lower metabolic activity at certain locations when compared with the normal subject group. We used our visualization application for analyzing the cortical surface systematically and attempted to verify the following hypotheses:

1. **H1:** There are significant areas of lower than normal PET activity on the brain cortical surface.

2. **H2:** The 3-D visualization interface is essential for perceiving the global map of abnormality in the reconstructed 3-D physical space.

Initial Setup

The first step is the extraction of the features. To quantify abnormal brain activity, we first need to create the normal distribution of the PET activity along the cortical surface. The PET activity is represented in feature space as a normalized histogram defined for each element in the *surface ROI mesh*. Each cortical ROI element encloses a certain anatomy of the brain surface. The PET activity is sampled at all the surface points within the ROI using the normal fusion technique, described in [125] and illustrated in Figure 4.1. An inverse normal vector starting from a vertex on the brain surface measures the PET value along the vector until it reaches a depth between $5mm$ and $15mm$ within the surface. The PET activity values aggregated along this vector are averaged to generate the attribute for the corresponding surface point. For our experiments, the depth was fixed at $10mm$. A statistical nonparametric approach builds the normal distribution for each ROI element using the combined feature distributions from a set of normal subject populations.

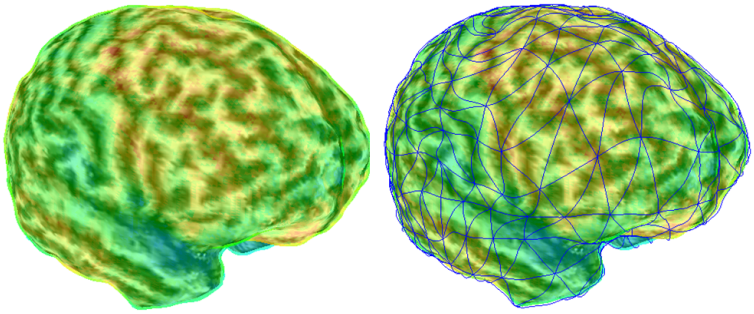

(a) (b)

Figure 4.1: Fusion of PET and MRI data. (a) shows the rendering of the PET concentration on the cortical surface. (b) shows the brain with the surface ROI mesh overlay.

The Normal Subject Distribution

The feature space represents an empirical distribution of the normal PET activity split between elements of the surface ROI mesh. For each corresponding element j and a subject i, at the level k, we compute the corresponding intensity histogram $\{H_{ijkl}\}$, where the index l is the histogram bin. The histogram is normalized to a unit area and is written as

$$H_{ijkl} = \frac{H_{ijkl}}{\sum_{l=1}^{m} H_{ijkl}}. \tag{4.1}$$

The average histogram for a group of N subjects is calculated as

$${}^{n}H_{jkl} = \frac{\sum_{i=1}^{N} H_{ijkl}}{N}. \tag{4.2}$$

Equation 4.2 is the normal distribution computed for the whole brain surface.

The Criteria for Abnormality

A_{ijk} is the numerical value that measures the difference in the area enclosed by the histogram $\{H_{ijkl}\}$ and the corresponding average normal histogram $\{{}^{n}H_{jkl}\}$. This measure is calculated

using the following equation:

$$A_{ijk} = \sum_{l=1}^{M} |H_{ikjl} - {}^{n}H_{jkl}|. \tag{4.3}$$

We find the probability density function (PDF) of the difference areas, A_{ijk}, for the normal subject group. Our data indicated a skewed distribution of the difference area resembling a Chi^2 distribution. However, we applied an alternative approach of determining cutoff thresholds for abnormality which does not require an analytical estimation of the PDF. From our preliminary data set we found that most of the nominal values for the normal subjects were within the 2.5 standard deviations (SD) from the group mean. Using the Chi^2 distribution the p-values for 2.5 and 3.0 SD were computed as $p = 0.01$, and 0.005 respectively. In comparison, the abnormal difference area was nearly 7.5 SD from the normal group mean. Since this result had a very high confidence value, for our analysis we fixed any value for A_{ijk} having a variance value larger than $\pm 2SD$ as the abnormal element.

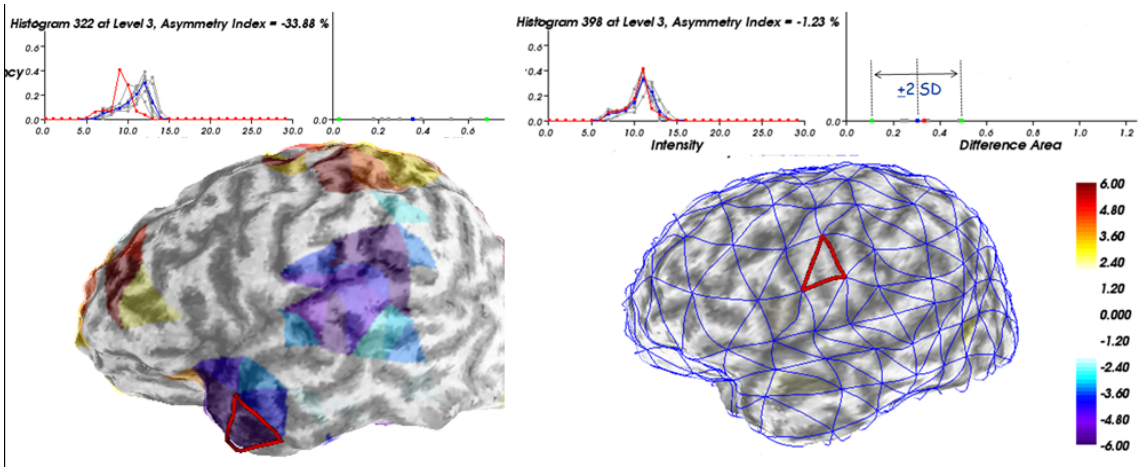

(a) (b)

Figure 4.2: Abnormality detection using PET and MRI integration. (a) PET abnormalities in a patient. The histogram for the element highlighted in red shows the activity for the patient in reference to the normal histograms. (b) A normal subject for comparison. As can be seen in the illustration, the surface is white, indicating no significant PET abnormalities in the data. The histogram for the highlighted element is also similar to the reference histograms.

Analysis

A set of 10 normal subjects were chosen for testing the hypothesis. These 10 normals were aligned to the SCBM, and the feature distributions were computed and saved in a database. Figure 4.2(a) visualizes the result for a pediatric patient with epilepsy. The visualization was designed to globally highlight the abnormality in the physical space using specific color mapping schemes. For the clear depiction of the abnormalities, we chose a diverging color map where the red color was mapped to A_{ijk} values higher than normal, and the blue color was mapped to A_{ijk} values lower than normal. The normal surface areas are shown in white so that only the difference areas are highlighted. To provide local control, an interactive tool allows the analyst to select an ROI element, which displays a graphical plot showing the feature distribution for that element. The gray-colored distributions represent the feature distribution of every single normal subject that was included in the statistical study. The patient's feature distribution is shown in red, while the normalized distribution is shown in blue. The plot is annotated with the element index and the ROI subdivision level. The accompanying plot on the right graphically displays, using a scatter plot, the mean and the standard deviation (SD) of the difference areas $\{A_{ijk}\}$ over the 10 normals; the patient's location is rendered as a red point. For the selected region highlighted in red in Figure 4.2(a), the difference area A_{ijk} has a value around $-5.2SD$, which was detected as an abnormality. For illustrative purposes, we display the analysis result for a normal subject in Figure 4.2(b). As expected, we found no abnormalities on the surface. The graphical plots clearly show that the feature distribution for the selected element is similar to the normal subject distribution.

User Study

We conducted a user study with five participants each analyzing five pediatric epilepsy patients. The visual analysis application scored a $> 90\%$ rating among the participants when posed with hypotheses $H1$ and $H2$. One participant was interested in testing this application for analyzing

patients with tuberous sclerosis and for children's longitudinal development studies.

4.2.2 Qualitative Analysis of Spatial Relationship Using PET and EEG

Currently, the most effective treatment for epilepsy is resection surgery. A great deal of planning and presurgery clinical sessions lead up to the decision recommending resection surgery. One of the sessions involves an invasive procedure for recording electrical impulses using intracranial EEG grids. One of the most critical decisions influencing the final outcome deals with the optimum placement of EEG grids. Choosing the grid locations is a laborious process and involves many brainstorming sessions among clinicians, neuroscientists and brain surgeons. Our intent was to introduce the visualization tool in the decision-making process. Specifically, we wanted to ascertain whether imaging features can guide the decision-making process effectively. We analyze the features across subjects that belong to the epilepsy group and examine the reproducibility of the result.

Initial Setup

We acquired CT images that captured the grid locations on the brain surface in 3-D. A mutual information-based 3-D volumetric registration algorithm was developed for aligning the CT image to the reference T1-weighted MRI image, as shown in Figure 4.3. The CT image was rendered in volume, and a thresholding operation was initiated to segment the EEG grid locations in CT. These locations were transferred onto the brain surface and reconstructed as spherical balls, as shown in Figure 4.3 on the right. For the analysis, we acquire PET images for the patients. We also record the seizure category for each implanted electrode for each patient. We pose the following hypothesis: The seizure onset areas are always in the boundary neighborhood of a hypometabolic region.

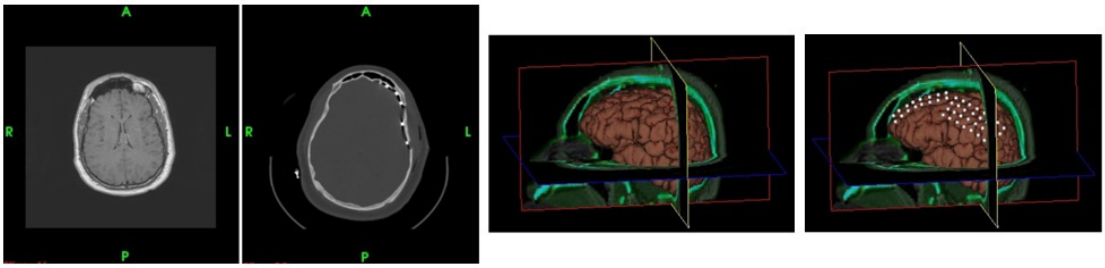

Figure 4.3: The MRI-CT registration pipeline. The grids are transferred to the MRI image as spherical balls.

Feature Representation of a Hypometabolic Region

Using the fusion approach described in section 4.2.1, we derive the mean value of the PET activity distribution for each ROI element. Using asymmetric analysis, the hypometabolic element is defined as the difference value between the mean value of an ROI element and the mean value of the ROI element symmetrically located in the opposite hemisphere. A negative value is identified as the hypometabolic element. The aggregate set of connected hypometabolic ROI elements forms the hypometabolic region.

Neighborhood of a Hypometabolic Region

The neighborhood of any ROI element is the set of all ROI elements that share an edge or the vertex with it. This neighborhood, also referred to as the first neighborhood, is precalculated and stored as an adjacency list within the application and can be queried on demand. The boundary neighborhood of the hypometabolic region is the set of ROI elements that falls in the neighborhood of a hypometabolic ROI element.

Analysis

Figure 4.4 visualizes the results from the procedure explained earlier. The EEG grids are visualized on the brain surface. The seizure onset electrodes are displayed in red. The hypometabolic regions are shaded in blue. The neighborhood ROI elements that form the boundary of the hy-

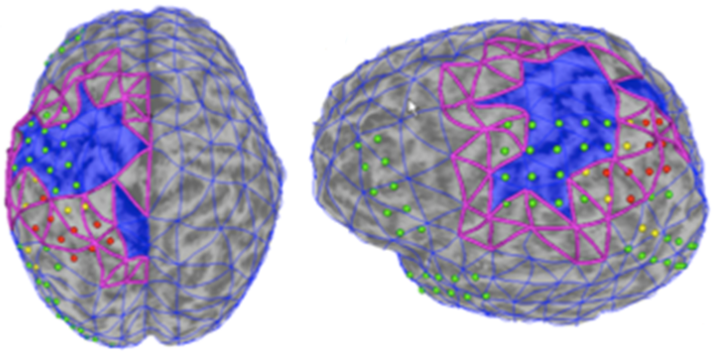

(a) (b)

Figure 4.4: Onset electrodes (red) are located outside the abnormal PET regions (blue) but are located within the border regions around the PET abnormality.

pometabolic region are highlighted in pink. The visual analysis clearly shows that the seizure onset electrodes were clearly shown to be outside the hypometabolic regions and located in the boundary neighborhood. This pattern was shown to be common among epileptic patients suffering from metabolic disturbance [2]. We designed an overlap measure based on the Dice coefficient for testing whether this observation was significant. This measure calculates the percentage overlap of the seizure onset electrodes with the neighborhood elements across patients. We found that this percentage was more than 90%. The visualization framework was able to consistently identify this spatial relationship that led to a robust placement protocol for future cases. To access the clinical variables associated with the metabolism changes in and around the hypometabolic region, we performed the Pearson's parameteric test for continuous and the Spearman's rank correlation test for ordinal variables. This was important so as to have much better confidence on the patients chosen for the study.

4.2.3 Creating a Standard Brain Activity Atlas Using Feature Composition Across Subjects

EEG grids are not only useful for seizure localization but are also used for mapping the highly specialized anatomical regions that relate to motor functions, language, and analytic thinking. Mapping these regions is essential for brain disorders that require surgical interven-

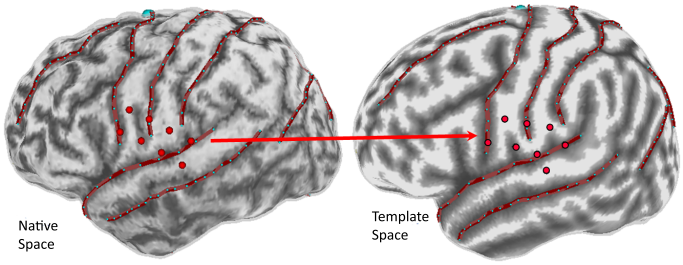

Figure 4.5: Transfer of electrodes from native space to the ICBM152 brain template.

tion and a successful rehabilitation post surgery. Motor and language area localization studies are pursued in a clinical lab setting over several hours. The patient is given a set of tasks designed to stimulate the regions at specific time intervals. Depending on the task and the electrical impulse record, the brain surface is classified to one of the highly specialized region labels. The purpose of this analysis was to ascertain whether specific anatomical areas correlate with these highly specialized functions, multiple areas are involved, or there is no correlation to any particular anatomical area. This analysis differs from the earlier analysis scenarios, because the analysis output is visualized on the template brain. The goal of the output is to identify the functional boundaries in brain anatomy for these highly specialized functions.

Initial Setup

There are 10 subjects chosen for this study. The brain surface of each subject was matched to the SCBM using the global alignment algorithm described in section 3.4.4. Each subject was implanted with EEG electrodes and was asked to perform a series of tasks. The data at each electrode was recorded every 10 $milliseconds$. Whenever the area under the electrode was stimulated, the electrode would generate an impulse. This impulse was given a value of 1; a no-impulse reading was given a value of 0. Hence, the feature is a high-dimensional temporal sequence of 1s and 0s for each electrode.

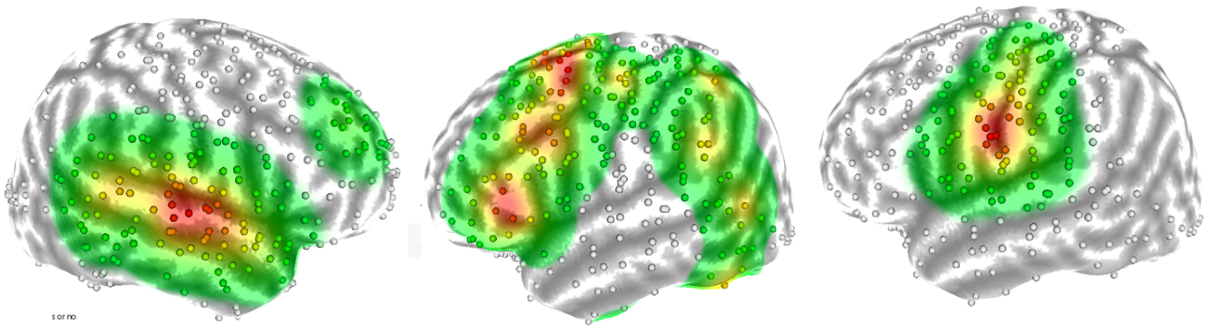

(a) (b) (c)

Figure 4.6: Standard brain atlases revealing specialized brain regions for (a) auditory, (b) language, and (c) sensory motor functions.

Atlas Visualization

Figure 4.6 shows some of the feature composition for different specialized functions visualized on the *ICBM*152 template. To visualize the electrode data on the *ICBM*152 surface, the 3-D electrode location was transformed to the corresponding template surface location (Figure 4.5) by convolution with the inverse transition map, described in section 3.4.1. For each time interval, the feature values for all the electrodes across the 10 subjects was composed to generate an influence field on the template surface, mapped to the sequential color map ranging from red to green. Higher influence values were highlighted using the color red. We generated two output visual patterns for rendering the atlas. The static patterns are shown in Figure 4.6 for the auditory, language, and sensory-motor functions. These frames correspond to temporal events where the influence field was the strongest, indicating the task was being performed. The moving pattern scrolls through the entire time sequence and clearly visualizes how the influence field grows and wanes as different tasks are being conducted.

Analysis

From the output, it is clear that the auditory region and sensory-motor region are strongly concentrated in the superior temporal region and the primary motor cortex, respectively, whereas the regions defining language involve multiple anatomical areas. Clinicians have found po-

tential use for these atlas visualizations to find correlations between speech impairment and specific neurological disorders.

4.2.4 Quantitative Cross-Subject Analysis of Connectivity Using DTI

DTI is a vector-valued image modality for visualizing neural fiber reconstructions. The neural fibers connect anatomical areas either on the cortical surface (cortico-cortical fibers) or within the brain, and the fiber organization along these connections can be quantified using anisotropy measures derived from the DTI image. The DTI image is very sensitive to white matter fiber orientations, and hence, most analysis studies target the white matter fiber organization. We briefly explain, in the following two sections, the diffusion tensor mathematics and the algorithm used for 3-D neural fiber reconstructions.

Mathematics of the Diffusion Tensor

DTI is a relatively new imaging modality technique [11] and relates the microstructural particle displacements, p, in underlying tissue with image intensities. In brain images, p along white matter fibers are higher. Hence, the probability distribution of p will represent an ellipsoid structure, indicating high anisotropy. The DTI image models p as a simple diffusion with a Gaussian profile as given in Equation (4.4),

$$G(x; D, t) = ((4\pi t)^3 det(D))^{-1/2} exp(\frac{-x^T D^{-1} x}{4t}), \tag{4.4}$$

where D is the diffusion tensor and t is the diffusion time. The MRI acquisition sequences follow the Stejskal-Tanner imaging sequence, which models the observed intensity of anisotropic samples as

$$S = S_0 e^{-bg^t Dg}, \tag{4.5}$$

where b defines the various parameters of the sequence called the weighting factor. To sample the ellipsoid p uniquely, the 3×3 diffusion tensor D needs to be solved. This requires at

least six independent measurements along the g gradient orientations. The solution is a set of eigenvalues, that specify an orientation-independent measure of the anisotropy at each voxel and the corresponding eigenvectors, which indicate the direction of water diffusion.

Probabilistic Tractography for 3-D Neural Fiber Reconstructions

A probabilistic tracking algorithm is devised based on work by Friman et al. [42]. The algorithm is based on a Bayesian inference and estimation scheme. Uncertainties due to noise or complex fiber architectures are not disregarded but captured in the model itself in the form of the posterior distribution at each voxel.

Given a source region X, the probability of connectivity between X and a target region Y is given by the formula

$$p(X \to Y \mid D) = \int_{V^1} p(1) \times p(v_{1:1} \mid D) + \int_{V^2} p(2) \times p(v_{1:2} \mid D) + ... + \int_{V^n} p(n) \times p(v_{1:n} \mid D), \tag{4.6}$$

where $p(v_{1:n} \mid D)$ is the probability of the fiber path going from X to Y, given the diffusion data D. V^n represents the sampling space of the connectivity between X and Y of path length 1 through n. Since Equation (4.6) is not analytically solvable, a rejection sampling strategy is employed. In other words, a large number of sampled fiber paths starting from the source region X is drawn at random, and the probability of the path between X and Y is evaluated. These random paths are computed stepwise until a predetermined length n. The steps are assumed to be unit length vectors, with the condition that each step is dependent only on the previous step direction. Since these samples reflect the model of the actual fibers, the posterior distribution at each step is calculated based on the diffusion data D. This distribution is written in terms of Baye's theorem as

$$p(\widehat{v}_i, \theta \mid \widehat{v}_{i-1}, D) = \frac{p(D \mid \widehat{v}_i, \theta) p(\widehat{v}_i \mid \widehat{v}_{i-1}) p(\theta)}{p(D)}. \tag{4.7}$$

The first term in the numerator represents the likelihood distribution at the current point and uses a constrained model based on a Gaussian diffusion profile. $p(\widehat{v}_i \mid \widehat{v}_{i-1})$ is the prior to indicate the dependence of the current point on the previous step direction. This assumption works well in a complex fiber neighborhood, because there will always be a preference for the previous step. The nuisance priors, $p(\theta)$, are the parameters of the Gaussian profile modeled as Dirac priors. Finally, $p(D)$ is the normalizing constant, which, combined with the above expressions, gives the probability distribution at $\widehat{v}_i$ over a unit sphere, as shown in Figure 4.7(a). To draw a random path, all the possible directions on the sphere are discretized and one direction is picked at random. The resulting sampling space for a source region X is illustrated in Figure 4.7(b).

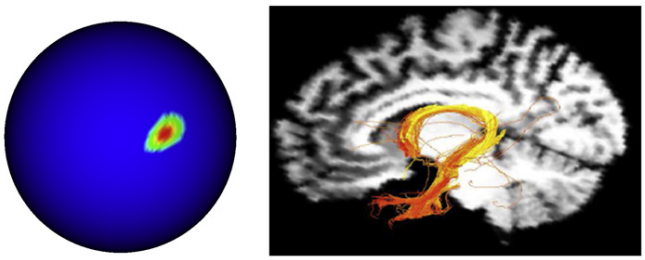

(a) (b)

Figure 4.7: (a) Posterior distribution at a voxel. Red represents the high probability for the path, corresponding to a low uncertainty value for this voxel. (b) Fiber tract identifying the fornix bundle, with probabilistic tracking.

Time Complexity: The fiber tractography algorithm is computationally expensive. Whole brain cortical fiber tractography can take upto 24 hours to compute. Our implementation has been developed on a Windows XP machine with 4 cores. To speed up computation we have implemented a parallel version of the algorithm based on the OpenMP framework. This allows us to combine the power of multi-core technology wherever available. To save time on analysis we also allow tractography on user selected seed voxels, chosen as ROIs within the brain, or surface ROI elements.

Affine Registration: MRI/DTI

The DTI image is compiled as a set of diffusion-weighted images and a non-diffusion-weighted image called the $B0$ image. The $B0$ image is a T1-weighted image but has a lower resolution, making it unsuitable for parametric registration (Section 3.4.1). So we always scan a high-resolution T1-weighted MRI image along with the DTI image. A 12-parameter affine registration [16, 135, 43] registers the DTI to the MRI image. The transformation matrix is preserved without resampling the DTI to the physical MRI space. Spatial transformation in DTI is nontrivial and modifies the real tensor orientation of the underlying data [1, 96, 63]. This can potentially smooth out the diffusive properties, introducing bias in the subsequent analysis studies.

Initial Setup

The caudate region located in the subcortical region of the brain is an important part of the brain associated with learning and memory. Developmental problems associated with language and voluntary control has long been associated with changes involving the caudate nucleus. Since many fiber tracts radiate from the caudate to the brain surface, changes in the fiber organization may affect development in pediatric cases. We decided to test our hypothesis on a set of pediatric subjects exposed to early deprivation. We wanted to test the following scenario: Does early deprivation in pediatric patients cause changes in the fiber organization between the caudate and the cortex?

Connectivity Measure: The Geometric Mean Probability

Probabilistic tracking creates a sampling space of fiber paths initiated from the seed regions. We calculate the normalized probability score for each path as given by the following equation

$$(GMP)_i = \frac{\sqrt[n]{(p_1)(p_2)..(p_n)}}{\sum_{j=0}^{k} N_j}, \tag{4.8}$$

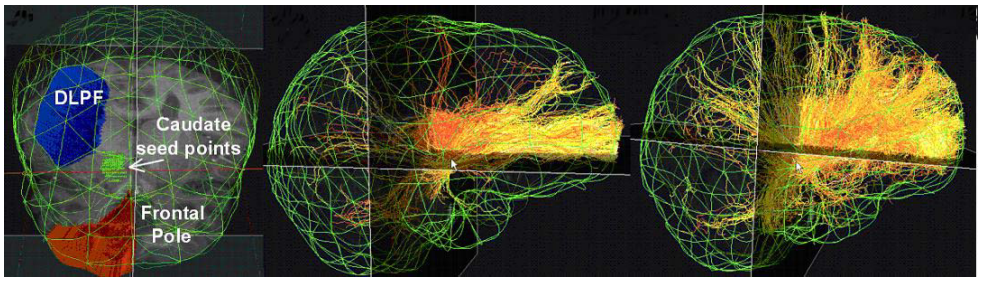

(a) (b) (c)

Figure 4.8: (a) shows the source ROI and the two target regions. (b) and (c) show the sampled fibers for the source ROI for the normal and ED subjects, respectively.

where n is the fiber path length and $p_{1..n}$ is the step probabilities along the path. The numerator represents the geometric mean of the step probabilities and generates a probability value that is independent of the path length n. The denominator N_j is a normalizing term, which is the sum of the geometric means of k fiber paths sampled from the seed region. This assigns an overall probability value to each path, termed as the geometric mean probability (GMP).

Analysis

Ten pediatric subjects with early deprivation (ED), forming a set, were chosen for the study. Similarly, 10 normal subjects, forming a set, were selected as controls. Each data set was globally aligned to the SCBM to generate the *surface ROI mesh*. An anatomical labeling scheme was built to organize the ROI elements based on anatomical areas. This was necessary to visualize the fiber endpoints on the cortex. The caudate nucleus was segmented from the MRI image and transformed to the physical DTI space using the affine registration matrix described in section 4.2.4. The segmented area was chosen as seed voxels for initiating the fiber tracking. For each voxel, $15,000$ samples were initiated to build the sampling space of fiber tracts. The ROI elements were chosen as the targets, and the GMP score was calculated for each ROI element.

Figure 4.8 illustrates the visualization results for a ED subject and a normal subject. Figure 4.8(a) displays the caudate region in green and the two target regions composed of ROI

elements, the dorsolateral prefrontal cortex (DLPF) and the frontal pole (FP). Figure 4.8(b) shows strong connections for fiber tracts between the head of caudate and the frontal pole for the normal population. Figure 4.8(c) shows that the fiber tracts are more diffused in early-deprivation subjects between the FP and the DLPF. To determine whether there were group differences with respect to the probability of the fibers, a $2 \times 2 \times 3$ mixed-design ANOVA was applied, where the between-subjects factor was the group (ED, normals) and the two within-factors were the source region and the target regions. Statistical results based on the GMP score confirm the differences. The values show that the connectivity values for tracts between the caudate and frontal pole are similar for the ED groups ($P = 0.27 \pm 0.13$) and controls ($P = 0.31 \pm 0.14$). In contrast, the caudate and DLPF region significantly increased in the ED group ($P = 0.053 \pm 0.04$) when compared with normals ($P = 0.0087 \pm 0.004$), as confirmed by the diffused tracts in Figure 4.8(c). To ensure that the results were reliable, we had two raters individually define the connectivity scores. The Pearson's correlation coefficients ranged between 0.96 and 0.99. Therefore, we conclude that the cross-subject connectivity analysis based on the GMP feature, was able to confirm cortical regions with significant differences in connectivity strengths [12].

4.3 Cross-Subject Evaluation of Subcortical Fiber Bundle Atrophy Using DTI

4.3.1 Initial Setup

We use our volumetric brain mapping and registration framework to evaluate the hypothesis that medial temporal lobe epilepsy has associated atrophy in the fornix and cingulum fiber bundles ([93]). We conducted a population-based comparison study using 12 healthy volunteers and 15 epileptic patients. For each subject, we use the MRI image and the 25-direction DTI image. Anatomical images are conformally mapped to a VCM (Section 3.7). Seed voxels selected in the reference template are mapped to the native space of each subject via the

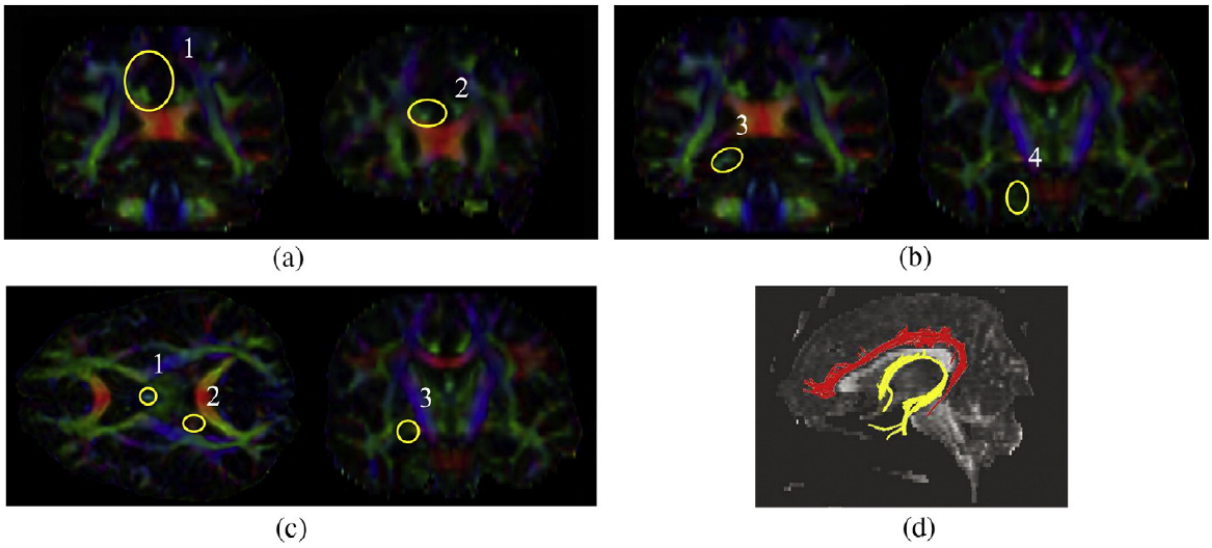

Figure 4.9: (a) and (b) show the manual selection of ROIs for the cingulum in DTI. (c) shows the manual selection of the ROIs for the fornix in DTI. (d) A DTI image on which the extracted cingulum and fornix fiber bundles are superimposed in red and yellow, respectively.

volumetric transition map. The MRI and the DTI are affine registered (Section 4.2.4) to each other. To track the fibers, the seed voxels are chosen on the template. Figure 4.9(a, b, c) shows the ROI selection protocol for the cingulum and fornix fiber bundles. The inverse map and the corresponding affine registration parameters transform the seed voxels defined on the VCM to the DTI space of each individual subject. The cingulum and the fornix fibers are illustrated in Figure 4.9(d). Probabilistic tracking of the bundles will generate around $2,000$ samples for each voxel in the ROI. The anisotropy cutoff is set at 0.2, and the maximum length of the fiber path is set at 500.

4.3.2 Protocol for Choosing the ROIs

The ROI selection protocol for the cingulum and fornix bundles is explained below (Figure 4.9). For the cingulum, there are four ROIs. Two are drawn in the coronal plane at locations where the genu and the splenium of the corpus callosum intersect the midsagittal plane (Figure 4.9(a)). The other two ROIs are drawn on the slice where the splenium intersects the midsagittal plane and the second one where the pons intersects the midsagittal plane

(Figure 4.9(b)). For the fornix bundle, three ROIs are drawn. The first ROI is drawn at the foramen of Monro; the second ROI is drawn at the posterior limb of the internal capsule. The third ROI is drawn in the coronal plane, where the slice intersects the pons in the midsagittal plane (Figure 4.9(c)). The ROIs were chosen carefully with expert intervention to ascertain maximum reproducibility of the fiber tracts. Only the fibers passing through these ROIs are chosen for analysis. We had three raters work separately on five normal data sets to test the reliability of the chosen ROIs. The three raters perform three trials on each of the five data sets. The inter-rater and intra-rater reliability analysis was calculated, and the result is listed in Table 4.1. The raters manually delineated the ROIs in DTI space with three trials for each data set (Figure 4.9(a, c)). The kappa values for intra-rater reliability values for the cingulum and fornix are 0.94 and 0.94, respectively. The corresponding inter-rater reliability is 0.93 and 0.94, respectively, for the cingulum and fornix. To test the accuracy of the mapping and registration framework, we include another reliability analysis measure called intermodal reliability. To evaluate the intermodal reliability, ROIs selected on the MRI template are mapped to DTI space and used to track the fibers. The third row in Table 4.1 shows the kappa values for the intermodal reliability calculated for the five datasets, 0.85 for the cingulum and 0.92 for the fornix. From these experiments, it is clear that all values fall in the "almost-perfect" agreement range [127]. We can also observe that operator dependence is minimal and that the statistical significance of the evaluation study is not affected by ROI selection protocol.

Table 4.1: Average kappa values (K) for intra-rater and inter-rater reliability for five data sets. Last row shows the intermodal reliability

	Cingulum bundle	Fornix bundle
Intra-rater (avg.)	0.94 ± 0.043	0.94 ± 0.03
Inter-rater	0.93 ± 0.04	0.94 ± 0.04
Intermodal	0.85 ± 0.02	0.92 ± 0.04

Fiber bundle	Mean volume ratio $\pm$ standard deviation	p-value of t-test
Cingulum (normal)	0.187 ± 0.031	$3.74 \times E-06$
Cingulum (patient)	0.109 ± 0.012	
Fornix (normal)	0.212 ± 0.030	$9.20 \times E-05$
Fornix (patient)	0.159 ± 0.015	

Table 4.2: The mean and standard deviations of the volume ratio (*VR*) values of the normal subjects and the temporal lobe epilepsy patients in the cingulum (a) and the fornix (b) fiber bundles.

4.3.3 Anisotropy Analysis

The anisotropy was quantified using the volume ratio *VR* feature,

$$VR = 1 - \frac{27\lambda_1\lambda_2\lambda_3}{(\lambda_1+\lambda_2+\lambda_3)^3}, \tag{4.9}$$

defined as the ratio of ellipsoid volume over the volume of the sphere. This equation measures the ratio of the isotropic and anisotropic components at each voxel so that a lower *VR* value indicates more isotropy and less diffusion. We then find the mean *VR* values of the voxels belonging to specific fiber bundles. The mean *VR* represents the global measure of the anisotropy. The results were computed through a group analysis based on the Student's *t*-test. For the cingulum bundle in healthy volunteers, this value is around 0.187, whereas for epileptic patients, it is around 0.109. This suggests that the mean *VR* of the cingulum in epileptic patients is 40% less than that of the normal subjects. The fornix bundle has a normal mean *VR* value of 0.212 compared with the epileptic patients that have a mean *VR* value of 0.159, which reflects a 25% decrease. A standard *t*-test on the data shows that the difference between the two groups is statistically significant (p-value < 0.0001). These values are consistent for the cingulum and the fornix across all subjects. The results are listed in Table 4.2.

4.3.4 Shape Analysis

Figure 4.10(a) visualizes the cingulum fiber bundle surface for a normal subject. The bundle surface has a smooth appearance consistent with the anatomy of the fiber. Figure 4.10(b)

shows the same fiber bundle for an epileptic patient. This bundle surface has a more bumpy appearance, which we hypothesize as being atrophied due to the disease. To test our hypothesis, we quantify the shape variations using the Gaussian curvature. Smooth bundles are expected to have a Gaussian curvature close to 0. The procedure is described as follows: The fiber bundle is skeletonized and parameterized from 0 to t to normalize the lengths across the subjects. The Gaussian curvature is sampled along the skeleton using the following equation:

$$C(r, \theta, t) = \int \int G(r, \theta, t) dr d\theta dt, \tag{4.10}$$

where $drd\theta$ is the cross section at the skeleton point dt, and G is the Gaussian curvature at the surface point defined by r and θ. We divide Equation (4.10) by the number of samples to calculate the mean Gaussian curvature of the bundle for a subject. Experiments conducted on 12 normal subjects and 15 epileptic patients measure the mean and standard deviation of the Gaussian curvatures for the two groups. Epileptic patients have a positive mean Gaussian curvature of 0.4355, indicating that it has more convex areas of high curvature. In contrast, the mean Gaussian curvature for the normal subjects is close to 0 (0.0590). Based on the analysis results we can confirm that shape differences in the cingulum fiber bundle is strongly associated with temporal lobe epilepsy.

4.4 Coclustering-Based Evaluation of Cortico-Cortical Fibers

4.4.1 Desired Goals

Cortico-cortical fibers start and end on the cortical surface. Since the *surface ROI mesh* subdivides the surface into 512 separate elements, it is possible to use these elements to create clusters of fibers based on their cortical endpoints. We first group the different elements into a set of anatomical areas. These areas are known as Brodmann areas and are delineated according to their anatomical function. Fiber clusters cannot rely on just the fiber endpoints since fiber bundles tend to diverge as they get closer to the brain surface. So to achieve a successful

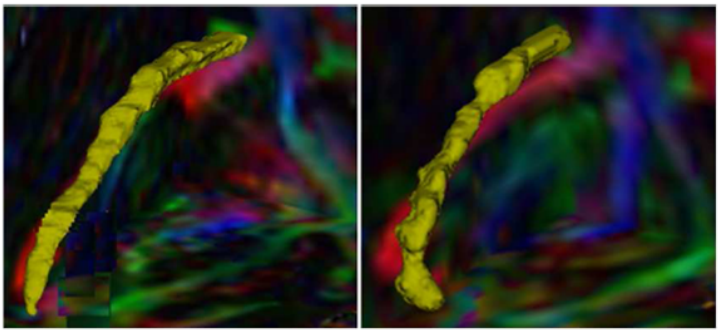

(a) (b)

Figure 4.10: Shapes of a part of cingulum fiber bundle of a normal subject (a) compared with that of an epileptic patient (b).

clustering, we designed a coclustering algorithm that uses both the cortical areas as well as the proximity between the fiber tracts using connectivity traces deep within the white matter structures.

4.4.2 The Coclustering Model

The coclustering model creates a computing model for cortico-cortical connectivity analysis. In this model, the structure of the cortex and cortico-cortical connections are represented as a graph $G = (V, F)$ (see Figure 4.11), where V is the set of cortical voxels and F represents all the pairwise cortico-cortical connections. For each voxel $v \, \varepsilon \, V$, we use $F(v)$ to denote the other voxel that is connected to v. Although not required by our model, the working hypothesis is that each cortical region is strongly connected to another specific cortical region and is weakly connected to other cortical regions. The goal of a coclustering procedure is to group cortical voxels into *K* clusters (where *K* will be determined automatically) while minimizing the cross-connectivity cost between those clusters so that (1) close voxels are within the same cluster, while distant voxels are in different clusters; and (2) each cluster is strongly connected to another cluster called its spouse cluster. While a traditional clustering paradigm does not consider the connection patterns between clusters, our coclustering model considers both the distances and connections between voxels. As a result, our coclustering model can provide several salient

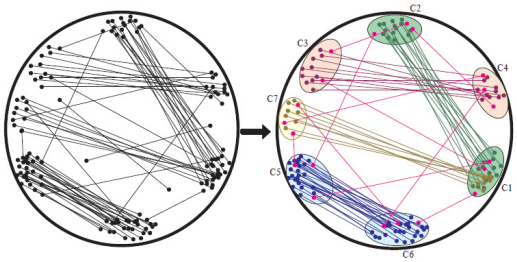

Figure 4.11: The proposed coclustering algorithm.

advantages over traditional clustering in partitioning graphs in general and in cortico-cortical connectivity analysis in particular. Figure 4.12 illustrates the comparison between the partitioning results from our coclustering model and from the traditional clustering paradigm. In Figure 4.12(a), the coclustering result from our model (right) coincides with the traditional clustering results (left), in which objects are grouped into four clusters from C1 to C4, and similar objects are in one cluster, while dissimilar objects are in different clusters. In this coclustering partition, each cluster is strongly connected to its spouse cluster, and each partner cluster coincides with the corresponding spouse cluster. In Figure 4.12(b), while a traditional clustering procedure only considers TWCV groups C2 and C4 into one cluster (left), our clustering model can potentially split that cluster into C2 and C4 by considering that most voxels in C2 are connected to C1 and most voxels in C4 are connected to C3 (right). In Figure 4.12(c), while a traditional clustering procedure might consider v1 and v2 as outliers or classify them as C4 simply because they are closer to C4 (left), our coclustering model can potentially reassign them into C3 by observing that these two voxels, like other voxels in C3, are mainly connected to C1 (right). Finally, in Figure 4.12(d), while a traditional clustering procedure partitions two clusters C3 and C4 as they fall apart to some degree in distances (left), our coclustering model can potentially merge them into one cluster C3 by observing that all voxels in C1 and C2 are connected to C3 (right). Finally, the coclustering algorithm can be formally stated as follows: given a graph $G = (V, F)$, a distance metric d for nodes $v_i \epsilon V$ and $v_j \epsilon V$ $(i \neq j)$, and α as a weight value, partition G into K coclusters, $\langle C_1, SC(C_1)\rangle, ..., \langle C_K, SC(C_K)\rangle$, such that the

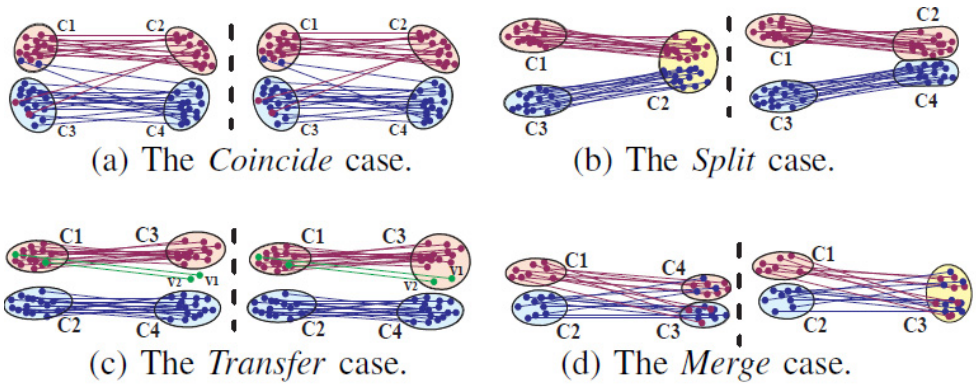

(a) The *Coincide* case. (b) The *Split* case.

(c) The *Transfer* case. (d) The *Merge* case.

Figure 4.12: Compare coclustering with traditional clustering results for the above four cases.

following objective function $OWCV$ is minimized:

$$OWCV(C) = \alpha * TWCV(C) + (1 - \alpha) * TPWCV(PC(C_1), ..., PC(C_K)). \quad (4.11)$$

$OWCV$ is the objective within cluster variation function that minimizes the cross-connectivity cost between clusters. Total within cluster variation ($TWCV$) and total partner within cluster variation ($TPWCV$) are functions that quantify the overall quality of the partition between clusters. Refer to [78] for further details of the objective function and the density-based co-clustering algorithm (BCA) to solve the coclustering problem. We list below the important results from the paper.

4.4.3 Analysis

We present a case study for the cross-subject analysis of cortico-cortical fibers clusters. We analyze pediatric Tourette syndrome cases and conduct comparison studies against a set of normals. We compared the connectivity strength of two major fiber tracts, the arcuate fasciculus (AF) and the major part of the superior longitudinal fasciculus (SLF) between a group of children suffering from Tourette syndrome (TS) and an age-matched control group. TS is a childhood-onset neuropsychiatric disorder characterized by the presence of motor and vocal tics, together with a range of semicompulsive behaviors. Functional disturbances in the frontal-striatal-thalamic circuit [106] are thought to be pivotal in producing TS symptoms; however, it

is likely that the arcuate fasciculus is implicated as well [30]. The arcuate fasciculus connects cortical areas responsible for language comprehension (Wernicke's area) and language generation (Broca's area) in the dominant hemisphere (left hemisphere in right-handed subjects) (see Figure 4.13(a)), and the SLF connects the prefrontal with the parietal cortex and provides information regarding perception of visual space. As both the spatial attention and the regulatory mechanisms for selection and retrieval of spatial information are believed to be normal in TS, we expected that the connectivity strength of AF is an important parameter in differentiating normal and abnormal subjects, while the connectivity strength of the SLF should not differ between the two groups. Initially, coclusters representing the AF and the SLF were selected, and the corresponding connectivity strength (CS) was calculated according to the following equation:

$$CS(|C_i|, |C_j|, N_{C_{ij}}, N_{C_{ji}}) = \frac{(|C_i| + |C_j|)(N_{C_{ij}} + N_{C_{ji}})}{2|C_i||C_j|}, \tag{4.12}$$

where $N_{C_{ij}}$ is the number of fibers from cluster C_i to cluster C_j, and $N_{C_{ji}}$ is the number of fibers from cluster C_j to cluster C_i. $|C_i|$ and $|C_j|$ are the number of voxels in cluster C_i and C_j, respectively. To test our hypothesis, we performed a cross-subject statistical analysis based on our coclustering results. Based on the statistical results on the normals, we identify the normative distribution for both the fiber tracts. The normal variability for AF has a mean of 0.50 with a standard deviation of 0.03. Corresponding variability of SLF has a mean of 0.77 with a standard derivation of 0.07. Any significant difference from this normative distribution is considered abnormal. Significant differences between the connectivity strengths obtained from the two groups were assessed using an independent sample *t*-test. Table 4.3 shows connectivity strength values determined in the two groups. As hypothesized, our results indicate a significantly lower connectivity strength of the left arcuate fasciculus between TS patients and controls (0.30 ± 0.09 $vs.$ $0.50 \pm 0.03, p = 2.2E-5$), but a similar connectivity strength between the two groups in the SLF (0.73 ± 0.09 $vs.$ $0.77 \pm 0.08, p = 0.19$), as shown in Figure 4.13(b)).

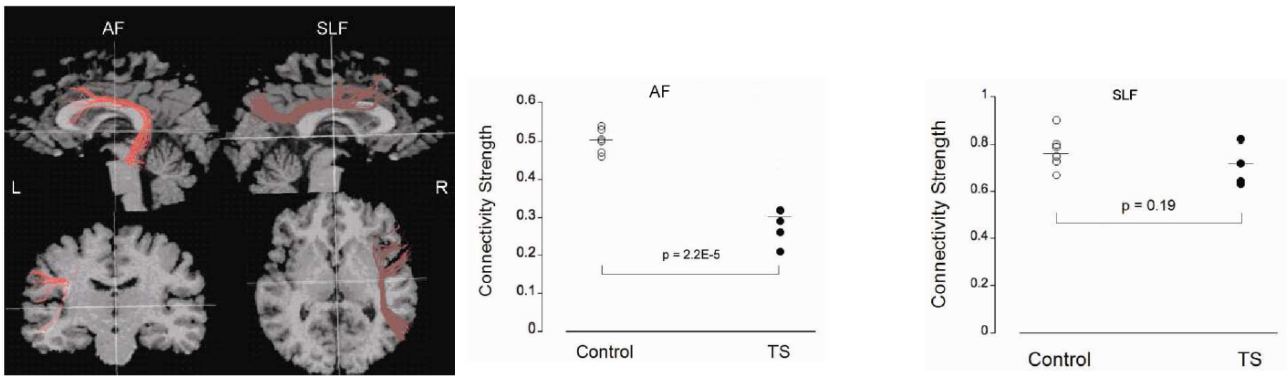

(a) (b)

Figure 4.13: (a) shows the fibers under analysis. (b) shows the results from the sample t-test.

Patient ID	AF	SLF
TS 1	0.21	0.72
TS 2	0.32	0.63
TS 3	0.26	0.64
TS 4	0.29	0.82
TS 5	0.32	0.82

Table 4.3: The connectivity strength of AF and SLF fiber tracts for five TS subjects.

We also validated the coclusters obtained by the clustering algorithm by comparing the two fiber tracts with the same tracts that were derived based on manual definition using anatomical landmarks within the brain. In order to quantify the correlation between the two methods, we determined for each fiber tract the number of fibers originating/terminating in each of the 512 cortical elements. Subsequently, the Pearson's correlation was computed between the two 512 element vectors for both fiber tracts. The results of this correlation analysis are listed as follows: The correlation between the two methods was determined as 0.83 ± 0.09 for the AF, indicating an excellent agreement between the BCA method and manual fiber tract definition. The correlation between the two methods for the SLF was found to be 0.65 ± 0.11. This value is lower, which is consistent with the greater physiological variability of this fiber bundle. These results indicate a very good overall agreement between the two methods.

4.5 Summary

This chapter describes the various quantitative cross-subject analysis experiments that were conducted using different image modalities. The visualization framework was an inherent part of the analysis, and it not only provided the structure for analysis but also displayed results in 3-D space reflecting the significant differences. Visual analysis using scientific visualization tools and efficient statistical computing models was the second main research contribution of this dissertation. The PET analysis results was published in [94]. The analysis described in section 4.2.2 was published in [2]. The coclustering of cortico-cortical fibers (Section 4.4) for analysis of connectivity strengths was published in [78]. The anisotropy and shape analysis results (Section 4.3) were published in *NeuroImage* [93].

CHAPTER 5

COORDINATED VISUALIZATION FOR BRAIN DISORDER STUDIES

In chapter 3, a geometry-based framework for global alignment of brain data sets was designed. The alignment process for mapping brain data sets is essential for building the *surface ROI mesh* that subdivide the brain into homotopic elements. This mesh plays an important part in quantitative analysis, which was covered in chapter 4. Visualization tools were extensively used to project the features in the 3-D space and confirm the significant results from cross-subject analysis. In this chapter, we will explain the roles of visual deduction and analytic processing for the exploration of subtle relationships among different features. We augment this scientific visualization framework with an information visualization interface that will aid in the exploration and coordinated visualization of the complete high-dimensional feature space.

This chapter begins with an introduction and explanation of the purpose behind the design of our coordinated visualization framework. We introduce two innovative views in the following section that will aid in the exploration of salient features and focus on determining the relationships between features. The following sections will explain the various components that form a part of the visualization application design, called BrainFusion. The last section presents case studies highlighting the usefulness of this technique.

5.1 Introduction

The brain is the most advanced organ in the human body. An exquisitely dynamic system, all aspects of human existence are explained by intricate low-level interactions among distinct biological processes. Researchers studying the brain have provided descriptive constructs at the biological and molecular levels. The brain has also been described in terms of its chemical constituents and labeled as a set of psychological concepts. However, the characterization of

these various descriptions is possible only through computational studies of high-level brain function. These functional processes are recorded using advanced scanning devices, which produce high-dimensional and multiresolution functional images. The internal mechanisms of these various processes are abstracted within the information space of each modality. Features extracted from the various modalities quantify the brain states corresponding to motor skills, language, communication, sensory perception, emotions, and sleep. An accurate 3-D depiction of the spatial structure allows scientists to project features accurately and examine their significance for certain behaviors (normal or abnormal), using detailed cross-subject statistical studies.

There is no single image modality that can comprehensively capture the brain's dynamics. It can answer only a handful of questions. To compensate for this limitation, qualitatively disparate protocols were devised for acquiring images that unravel complementary activity in the brain. For example, functional magnetic resonance imaging (fMRI) and single-photon emission computed tomography (SPECT) measure brain responses to routine tasks such as learning and communication. Positron emission tomography (PET) images measure the brain's metabolic rate. Electroencephalography (EEG) readings measure the electrical activity of neurons. Magnetic Resonance Imaging (MRI) measure the detailed structural variability of tissue shape, volume, and density. Diffusion Tensor Imaging (DTI) measures the diffusivity of water molecules in white matter tissue. Susceptibility weighted imaging (SWI) and magnetic resonance angiography (MRA) measure the structural properties of the vasculature. Most of these modalities are intrinsically multidimensional, and they derive a bunch of distinct and equally high-dimensional and multiresolution features (Figure 5.1).

In chapter 4, we examined some of these features for quantitative analysis, and detailed experiments confirmed their significance for the diagnostic testing of abnormal brain behaviors. Composing these different features as a cooperative set of specific functions will augment our knowledge about specific relationships between distinct biological processes. However, this

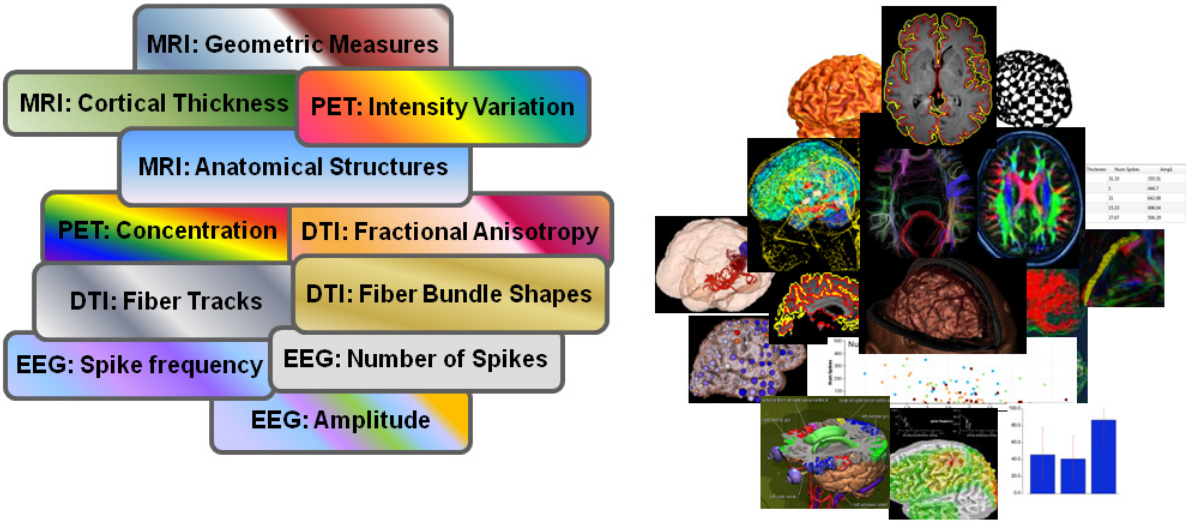

Figure 5.1: Each image modality presents the brain in its own qualitative information space and quantize it as a set of multidimensional features.

task in brain reverse engineering is not as straightforward as one might think. There are two principal reasons for this. Our understanding of the brain, and the seamless working of its various processes, is very limited. Constructing a mathematical model that captures interdependencies between multiple salient features only works for very simples cases (Section 4.2.2). The second reason is that brain disorder studies follow a very traditional and labor-intensive path. Based on the symptoms, scientists explore functional images that encode the abnormality within the feature. Much of the initial speculation comes from past experiments and empirical pieces of evidence from similar studies. Feature selection or derivation may involve some modeling and processing on the researcher's part. After several trial-and-error steps, a hypothesis is generated and tested, using detailed statistical experiments against a normal subject group. The effect size is calculated to determine the number of normal datasets needed. It undergoes the same processing steps to generate similar features for comparison. Domain scientists understand the value of visualization, but the scientific visualization tool is only capable of systematic features generation and quantification and is not actively involved in gathering insights. In most cases, these visualizations are static, and the quantified values are arranged

in a spreadsheet program or a statistical package (Section 4.2.4) for analysis. Data processing preceding the features quantification may be time-consuming and repeated for a given subject group on a per-analysis basis.

Since the model-driven approach does not seem encouraging, we chose to employ a data-driven approach to tackle the brain reverse engineering problem. Humans are well-adapted to consuming visual information, and a strong, visually perceptive design produces much better results when compared with more common statistical techniques [70]. We augment our framework with information visualization paradigms that will aid our analysis process. The immediate goal of this new approach is to reduce the time spent on data processing and free up valuable human resources to more effectively concentrate on the exploration and analytics of the complete, high-dimensional feature space. We leverage human cognition and perception using an interactive visualization system and analyze brain disorders through iterative data-driven exploration of image features.

5.2 The Role of Information Visualization

Information visualization is a technique that relies on the cognitive skills of a human analyst to further the discovery and interpretation of hidden patterns and correlations within a large data source. The main focus is on the creation of approaches and spatial representations of data that convey information intuitively without a steep learning curve. The emphasis on interaction allows the analyst to focus on data exploration rather than data processing. We have chosen two specific spatial representation designs that will aid in the visualization of the high-dimensional feature space and explore the relationships among a selected set of salient features.

5.2.1 The Coordinated Multi-View Table Layout

Features are the most important part of our analysis. The *surface ROI mesh*, first introduced in chapter 3 (Section 3.5), produces a systematic structure for feature derivations. The feature can either be a scalar measure or have high-dimensional components. Since the principal goal is the exploration of saliency among features, all features should be simultaneously viewable

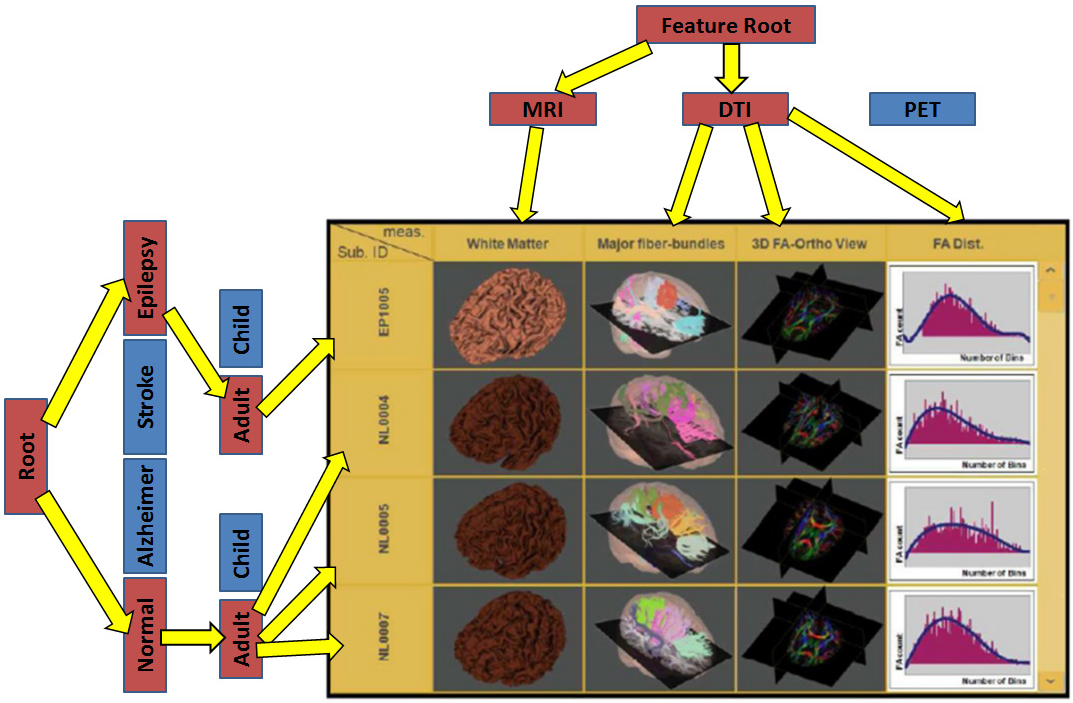

Figure 5.2: The Coordinated Multi-View Table Layout.

on demand across multiple subject groups. The tabular format is the most preferred representation for high-dimensional data points. The dimensions are mapped to columns, and the rows represent the data points. A similar representation is built for visualizing the imaging features. Figure 5.2 shows the multi-view table layout, which is one of these tabular representations. The selected features become the dimensions displayed column-wise within the table, and the data points are the individual subjects organized into groups. Each cell within the table is an interactive 3-D display pane, and each feature is displayed within its own 3-D anatomical area. A selection panel allows the analyst to select specific image modalities and their associated features. Two level-of-detail (LOD) filters offer advanced control over the selection criteria. The first LOD filter sorts the rows based on subject groups. There are various factors defined for further manipulation within each group. These include textual (age, gender, geographic location, and ethnicity), and numeric parameters (count, mean, and variance). The second LOD filter organizes the columns based on the surface ROI element indexes. Different anatomical

labeling schemes are provided for this purpose. The specifications for feature selections can be chosen either for a single subject or for group-based analysis (Section 5.5.3). In both cases, the selections are translated into formal queries and sent to a back-end data management system that assembles the data in a coordinated multi-view table layout. The display panes are interactive and coordinated so that the same anatomical area is under focus in each section. This setting can be changed on a per-column basis. All columns have a feature significance rank that highlights the saliency of each feature. The columns can also be organized based on this feature significance rank (Section 5.5.3). Clicking on the column-heading pane will display the statistical output (Section 5.5.3) as graphical plots. These plots confirm the saliency, detail the statistical algorithm used, and print the quantitative results.

5.2.2 The Mollweide View

A salient feature with a proven hypothesis is an important disease predictor. The feature's significance should be consistently reproduced within its subject group. Multiple features may be significant, but can be anatomically distant. The individual results do not clearly explain any interrelationships. The question naturally arises whether any interdependencies can be predicted between these features. We answer this by using an innovative representation borrowed from cartography, called *Mollweide view*.

The *Mollweide view* serves two purposes. First, it fits a 3-D image of the brain into a 2-D projection space so that the entire brain surface is visible. Second, each relevant feature is coded to visual entities, such as shapes, symbols, or sequential color maps. Figure 5.11 shows the *Mollweide view* for a 3-D brain. Anatomical ROI elements are projected in 2-D as well. The projection space has a vertical line at the center that separates the left and right hemispheres of the brain. The background colors in the 2-D view match the anatomical label colors in 3-D, which helps the analyst identify the area of the brain that he or she is viewing. The projection method is a popular technique used in cartography for the development of global maps. This method sacrifices geometry and shape in favor of an accurate depiction of surface areas. This is

especially useful where the area in question takes precedence over the shape. Since the entire cortical surface is visible in the 2-D projection and the features are encoded to visual entities that are mutually exclusive, it is much easier to predict any interdependency using this method. More details on its construction are given in Section 5.5.3.

5.3 Design

The preliminary design was based on a collaborative effort among computer scientists, medical researchers, and statisticians. The *Mollweide view* was very positively received by our colleagues in the medical research group, because the entire 3-D brain surface could be viewed without occlusion. Mapping visual entities to different features was deemed innovative because the mutual exclusivity of these entities minimized feature overlap. Additional comments on the table layout were about its ease of use and its possibilities as an alternative to static visualizations in analysis. The group also noted the application's capability to interactively scrutinize multiple features involving two or more subjects. Based on the comments received, we focused our attention on building a visual analytical framework that could take advantage of these new representations.

Some important design considerations for our visual analytic framework are listed below.

- *Feature Selection:* An interactive selection interface should allow the analyst to choose any number of features for visualization. Features can be ordered based on rank or some user-generated criteria.

- *Rank Predictors:* To aid exploration, each feature is given a significance ranking. This will be a very useful measure for initial selections within the feature set.

- *Real-Time Visual Queries:* As features are chosen during analysis, the system should interactively update the views with the new required information. Within the data source, selections translate to queries for fast retrieval. These queries also play a role during calculation of the significance ranks.

- *2-D and 3-D Coordination:* As features are mapped to visual entities in the 2-D abstracted view, these features are simultaneously annotated in the 3-D native space to provide anatomical context.

- *2-D Graphical Plots:* Correlation, outlier detection, and clustering among features are important indicators of relationships involving multiple data sources, and they are needed for effective data analysis. Graphical plots map dimensions for two or more features.

Our framework, termed BrainFusion, is the first attempt to use visual analytics for the multimodality integration of high-dimensional medical images. It uses a data-driven approach to explore and confirm significant features that highlight the underlying abnormality of the disease under study. The complete design of our framework is explained in the following sections.

5.4 Data Analysis and Integration

5.4.1 Feature Sampling

The *surface ROI mesh* is reproduced in Figure 5.6 for the resolution level 3. The elements are part of the nominal spatial dimension and is guaranteed to be homotopic (Section 3.5). Each ROI element has a similar surface area distribution as every other ROI element. Since the elements do not have any anatomical meaning, we supply two anatomical labeling schemes, which are the Brodmann area labels (BAL) (Figure 5.3(b)) and the FreeSurfer anatomical labels (FAL) (Figure 5.3(a)), to arrange these elements. Apart from these labels, we can also delineate the brain into different cortical parts called anatomical lobes (AL) (Figure 5.3(c)). The different labels are mapped to qualitative color palettes derived from ColorBrewer [52].

Each ROI element defines a vector of multidimensional features that characterize the particular element. We distinguish three distinct types of features which can be further classified as a structural feature or a functional feature. The three distinct types of features are the spatial point features α, the scalar feature fields β, and the vector feature fields γ. The spatial

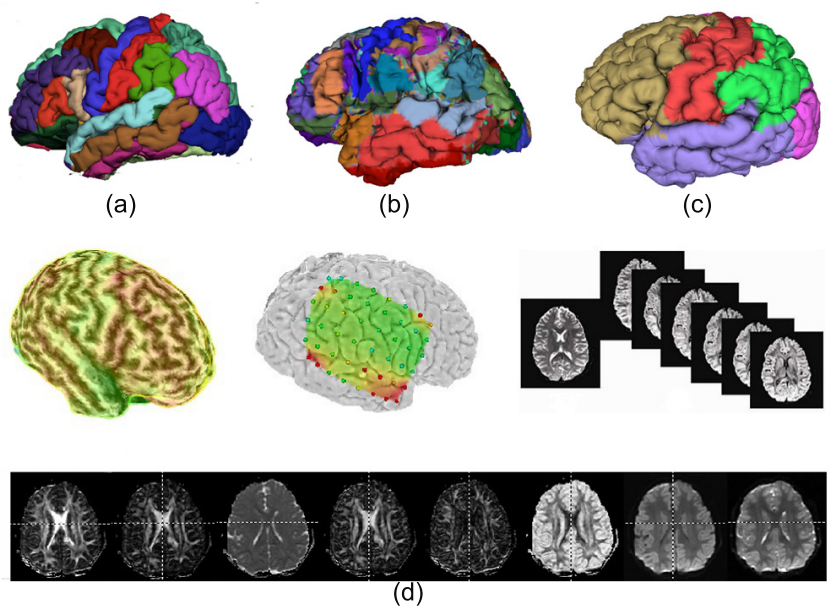

Figure 5.3: (a) shows the FreeSurfer anatomical labels. (b) shows the Brodmann area labels. (c) shows the anatomical lobes. (d) shows the different modalities, The second row visualizes the PET modality overlaid on the MRI, the EEG modality, and the DTI modality. The last row shows the measures extracted from the DTI.

point feature is a scalar value defined at a particular location within the element. This feature also resembles predicate values from observational studies. For example, signal processing on the temporal EEG recordings derive scalar point features defining the electrical spike at each electrode. However, during a seizure episode, the EEG electrodes can be classified as onset, or normal by direct observation. The scalar feature fields are integrated over the gray matter volume (GMV) enclosed within the element. These are visualized as histograms, density maps, or box plots. The scalar fields derived from the structural images define the different features not limited to the curvature of space within the element, thickness distribution of the gray matter, water diffusion properties, and the tissue volume distribution. The vector field features describe the connectivity between the different elements. The vector fields are mostly structural measures and characterizes the space between the element pair. The enclosed space can be defined as surface or volume and added as a measure-valued dimension with an entire list of scalar measures derived for it. The measure-valued dimension is also scalable to chosen

Structural Features						
MRI$CorticalThickness	MRI$MeanCurvature	MRI$GaussianCurvature	MRI$GrayMatterVolume			
MRI$PointThickness	DTI$FiberTract	DTI$FA	DTI$RA	DTI$MD	DTI$VR	DTI$ADiffuse
DTI$TProd	DTI$Surface	DTI$LI	DTI$PI	DTI$Lambda1	DTI$Lambda2	DTI$Lambda3
Functional Features						
PET$MetabolicRate	PET$Hist	EEG$Category	EEG$SpikeFreq	EEG$Amplitude	EEG$Slope	
EEG$Duration	EEG$TSlope	EEG$TDuration	EEG$TAmplitude	PET$AsymIndex		

Figure 5.4: Features listed for four different modalities and grouped as a structural feature and a function feature. The convention used for the name is X$Y, where X is the modality and Y is the feature extracted.

intervals of a feature. We have predominantly been using the EEG, the DTI, the MRI, and the PET modality (Figure 5.3(d)). Figure 5.4 shows a list of all features derived from each of these modalities, organized by type.

The third dimension is the population dimension that organize different subject groups. The classification into groups are mostly based on data available via clinical diagnosis charts, psychological and physical examinations, environmental factors, and age. The explicit details for this dimension are outside the scope of this dissertation. The assumption is that the subject groups are organized as a set of groups based on brain disorders and the normal group.

5.4.2 Automated Analysis and Statistics

The feature vector for each element can be represented directly in the coordinated multi-view table layout and ordered based on significance. The type of statistical algorithm available to the user is based on the feature type and the goal of the analysis. The table layout will generate queries to gather all the relevant features from the different subjects, compute the analysis results, and visualize each feature within the display pane. As explained in the previous section, some features are observational measures and do not need any statistics to highlight their significance. We mostly generate statistics on scalar field measures located at each element or derived from vector feature fields. Depending on the analysis being performed, different

types of statistics are used. We highlight two general statistical testing techniques that depend on the kind of analysis being pursued. If a single patient is being analyzed, the comparative statistics with a normal distribution will test for outliers. As the analysis progresses from a single patient to its subject group, significance testing will use statistical parametric tests. The analysis results can be easily viewed in the table layout giving the analyst ample opportunity for changing the parameters for testing significance or to make conclusions.

5.5 Visual Data Analysis for Brain Disorder Studies

5.5.1 Desired Goals

BrainFusion will equip scientists with tools to explore significant relationships between features, and effectively communicate predictions on brain disorders. Figure 5.5 illustrates one of the shortcomings prevalent in current visualization tools. The PET abnormal areas (Figure 5.5(a)) and the EEG onset electrode locations (Figure 5.5(b)) typically map to different spatial locations. Predicting the unified process behind localization to different anatomical elements naturally draws the user toward understanding the interdependency between these two significant feature outputs. For a single ROI element there are multiple overlapping features. Exploring the relationships between these overlapping features (Figure 5.5(c)) will improve our understanding of the underlying process.

Since all the features are available for display within the table, we can effectively explore the relationships between features, build specific hypotheses, and discover hidden relationships. The requirements of our design is summarized below.

- Identify features that significantly encode the abnormality induced by the corresponding brain disorder.
- Explore the relationships among features within a common anatomical area in a single subject and generate the required statistic to test.
- Compare two or more significant features across multiple spatial elements and identify

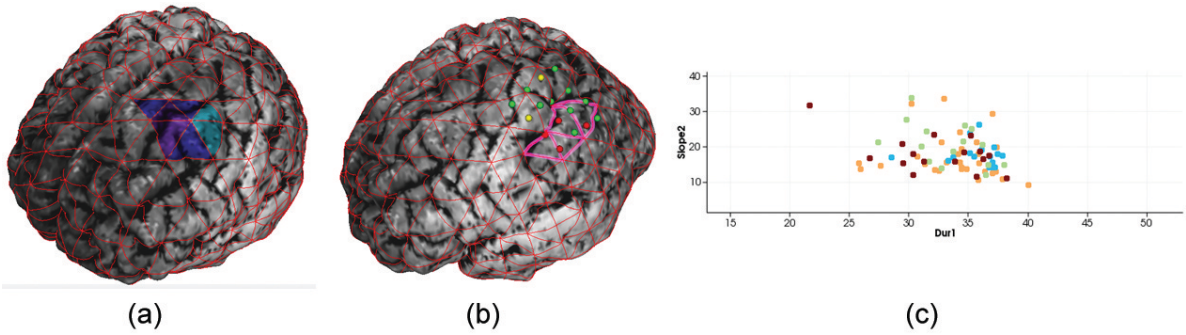

Figure 5.5: (a) and (b) shows the significant PET feature and the EEG onset electrode (red) on the same subject. (c) shows a scatterplot of two spatial point features α. The categorical color label in (c) refers to the grid number the point refers to.

the interdependencies between them.

- Perform statistical analyses to validate and enhance the insights gained from the explorations.

5.5.2 Data Preprocessing

Given the subject brain B and the template brain T (*ICBM*152 atlas brain), the algorithm given in section 3.4.4 generates the geometry-preserving surface shown in Figure 5.6. For the resolution level 3, the element count $N(e)$ is set to 512 distinct elements. The elements $e \in E$ are ordered according to the following two rules. The first rule says that $\{e : e < N(e)/2 \in L \;\&\; e > N(e)/2 \in R\}$, where L represents the set of elements that belong to the left brain hemisphere, R represents the set of elements that belong to the right brain hemisphere ($N(e) = L + R$), and e is an element index mapped to the natural number set starting from zero. The second rule says that for an element $e1 \in L$ in the left hemisphere, its symmetric position on the right hemisphere is identified by the following equality: $e1' = e1 + N(e)/2$. We categorize the elements into three labeling schemes: the BAL(e), which are the Brodmann area labels; the FAL(e), which are the FreeSurfer anatomical labels; and the AL(e), which are the anatomical lobes. The element sequence within each label is organized in ascending order.

Given a subject B, and an anatomical element e, the feature vector Ω is composed of com-

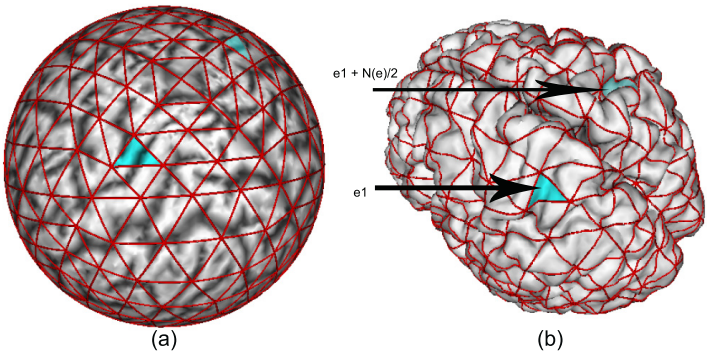

Figure 5.6: The brain surface is mapped to the sphere, which is aligned to the template and is subdivided to the desired subdivision level to generate the SBRP. The element index follows the rule such that e1 and e1+N(e)/2 are symmetric across the left and right hemisphere.

ponents belonging to one of the three feature types $\{\Omega : \Omega_i \in [\alpha, \beta, \gamma]\}$. Each feature also has a rank predictor variable φ, which is a real value associated with each feature component and indicates its significance rank. The value is calculated for each feature type and is mapped to a value between $[0, 100]$. For sampling features in $[\beta, \gamma]$, the GM-WM boundary (Figure 5.7(a)) is extracted using an in-house tissue segmentation tool. The element e is extruded until it intersects the GM-WM boundary (Figure 5.7(b)). The cortex volume enclosed within the extruded element provides the samples Figure 5.7(c) for β. The feature type γ uses only DTI images. We treat the voxels within the cortex volume as seed voxels, and use the probabilistic tracking algorithm [42] to generate the white matter fibers and calculate (Section 4.2.4) the connectivities p_i for each fiber. We retain only those fibers that connect two elements. To give anatomical meaning to the fibers, we use the fiber clustering algorithm [78] to cluster individual fibers into fiber bundles that connect anatomical areas as defined for BAL and FAL. Within each fiber bundle, we also save the connectivity scores between pairwise elements. Finally, for spatial point features α we identify the corresponding element it resides in and specify a neighborhood set $F(\alpha)$ of other spatial point features along with the geodesic distance between them.

All of the features are precomputed for each brain data set and are systematically saved in a database for easy retrieval during analysis.

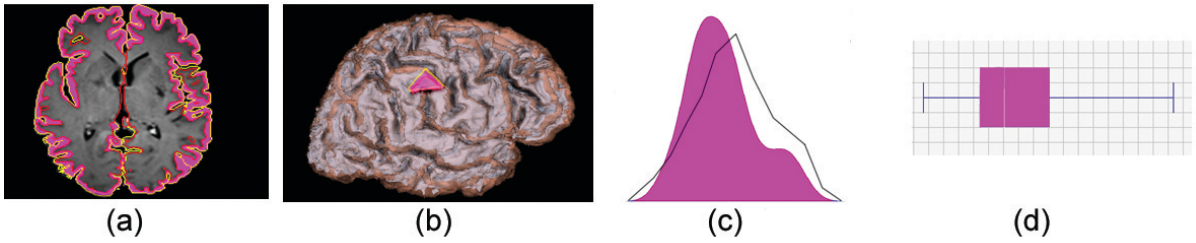

Figure 5.7: The purple shading in (a) shows a cross section of the volume enclosed between the outer GM surface (yellow border) and the inner WM surface (red border). An anatomical element shown in purple in (b) is extruded starting from the GM surface until it intersects the WM surface to recover the cortex volume enclosed within that element. The corresponding scalar field feature β is sampled within this volume to generate the density plot for the element. (c) shows the density plot shaded in purple, with the histogram shown as a line plot. (d) shows the box plot for the corresponding histogram.

5.5.3 Interactive Visualization of Functional and Structural Features

Medical scientists use scientific visualization tools that color-code the significant features onto the brain surface. Figure 5.3(d) shows the EEG modality that generates a heat map of the electrical activity of the brain with respect to the spike frequency. The color maps can be dynamically adjusted to enhance the hidden information within the feature. The visualization does have its limitations. There is no interaction with other features derived from the EEG. Moreover, we cannot visualize multiple features simultaneously, thus, limiting our ability to visualize its relationship. For example, how does the amplitude of the spike correlate with the slope of the spike? Do we see patterns within the data only for high spiking electrodes? Does filtering the electrodes remove noise and enhance the information? Currently, these questions are answered by generating static visualizations and graph plots by scraping the data offline and comparing them side by side. We have designed tools that addresses these limitations.

Visual Representations Using Filtering Thresholds

A substantial amount of information is acquired based on observational data. For example, observational records in epilepsy studies reliably identify the onset EEG electrodes during a seizure event. Currently, the effective treatment for epilepsy is resection surgery. However, the

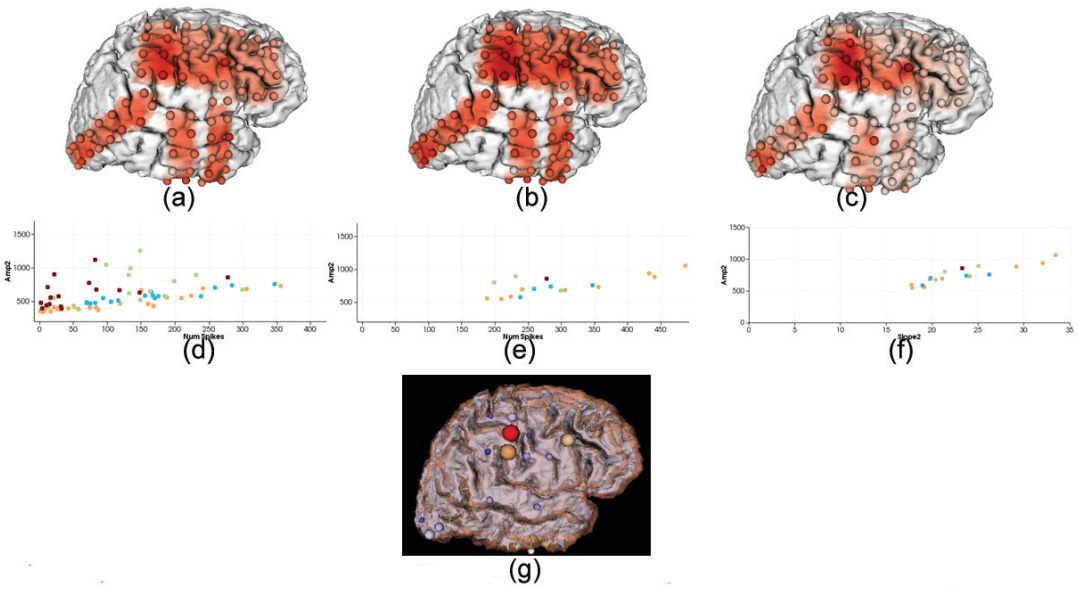

Figure 5.8: (a), (b), and (c) show the heat maps by mapping the spatial point feature EEG$Amp2, EEG$Slope2, and EEG$NumSpikes to each electrode and interpolating the values based on distance. As illustrated in the figure, (c) identifies the high-activity electrodes, whereas (a) and (b) have mostly a similar color distribution over all the electrodes. (d) shows the relationship between the EEG$NumSpikes and the EEG$Amp2. For higher values of EEG$NumSpikes, the correlation between the EEG$Amp2 and EEG$NumSpikes is stronger, after filtering the data on the interval EEG$NumSpikes $\in$ (200,483)(e). (f) shows the correlation between the EEG$Slope2 and EEG$Amp2 on the filtered interval. (g) shows the mapping of features to the size (EEG$Slope2) and color (EEG$Amp2). Only electrodes that have EEG$NumSpikes greater than 200 are shown.

decision about resecting the abnormal brain tissue is crucial for successful rehabilitation of the patient. As previous studies have shown, onset EEG electrodes identify the trigger for seizures but not the origin of the trigger. Hence, electrical activity in the brain needs to be studied in between seizure events. Figures 5.8(a), 5.8(b), and 5.8(c) show heat maps for spatial point features acquired for each electrode over a certain time interval in between seizure events. These visualizations declare the spike frequency Figure 5.8(c) as an important feature that discriminates between the most active electrodes. The heat map for the amplitude (Figure 5.8(a)) and the slope (Figure 5.8(b)) do not show much differences among electrodes. This highlights an important problem. Any information that might be available from the amplitude and slope is likely to be missed in these heat map visualizations.

To give scientists more flexibility to experiment with multiple representations, we provide interactive plots that highlight the relationships between the features. Visual entities such as size and color (Figure 5.8(g)) are mapped to the electrode locations in 3-D. These mappings allow us to look at two features within the same representation. The corresponding 2-D plots (Figures 5.8(d), 5.8(e), 5.8(f)) visualize the feature relationships. For example, in Figure 5.8(d), the graph is more noisy at lower spike frequency values. To adjust the visual representations, an interval is chosen (Figure 5.8(e)) that filter the outputs, reduce the feature space, and clean up the noise such that the dominant relationship is clearly highlighted. These relationships are subtle but very important because it gives researchers a chance to classify spikes based on these relationships and identify common patterns among electrodes within the subject and further devise queries to analyze these relationships across different patients with a similar disease profile.

Visualizing Overlapping Features Within Elements

Quantifying the significance of a single feature was already discussed in chapter 4. Scientists are interested in visualizing other features derived at the same location, especially their behavior and relationship to the significant feature, or identifying a particular linear combination of features at each element such that a distinct diagnostic signature can be predicted within the subject group. Our tool supports these kinds of interactive explorations. The most interesting feature combinations are sorted in ascending order of their rank variable φ. We design the visual representation as follows. A table layout scheme will list the selected element as rows and the overlapping features as columns. Each display pane will display a single feature and visualize it as a histogram, a density plot, or a box plot. At the bottom of each pane, we color-code the rank predictor variable φ for the feature. The φ is calculated as follows: Before the analysis begins, scientists provide selection specifications for choosing the data sets in the normal subject group. During the exploration stage, as the elements and the features are se-

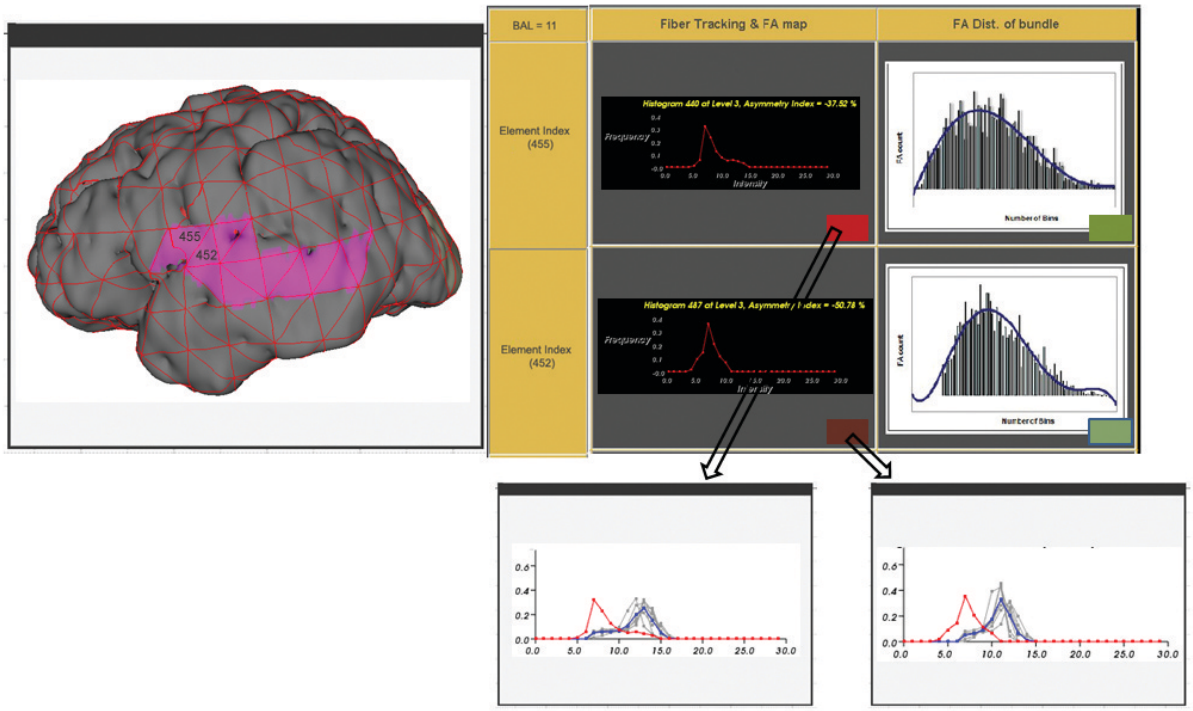

Figure 5.9: For the BAL anatomical label = 11, the figure shows the table layout for two elements, 452 and 455, and shows two features, namely the PET activity histogram and the FA count histogram. at the bottom of each display window, the colored box specifies the rank. Red color indicates a higher value. Clicking on the box will open a new window which shows the same patient histogram, along with the normal histograms. This clearly shows why the system ranked this feature as significant.

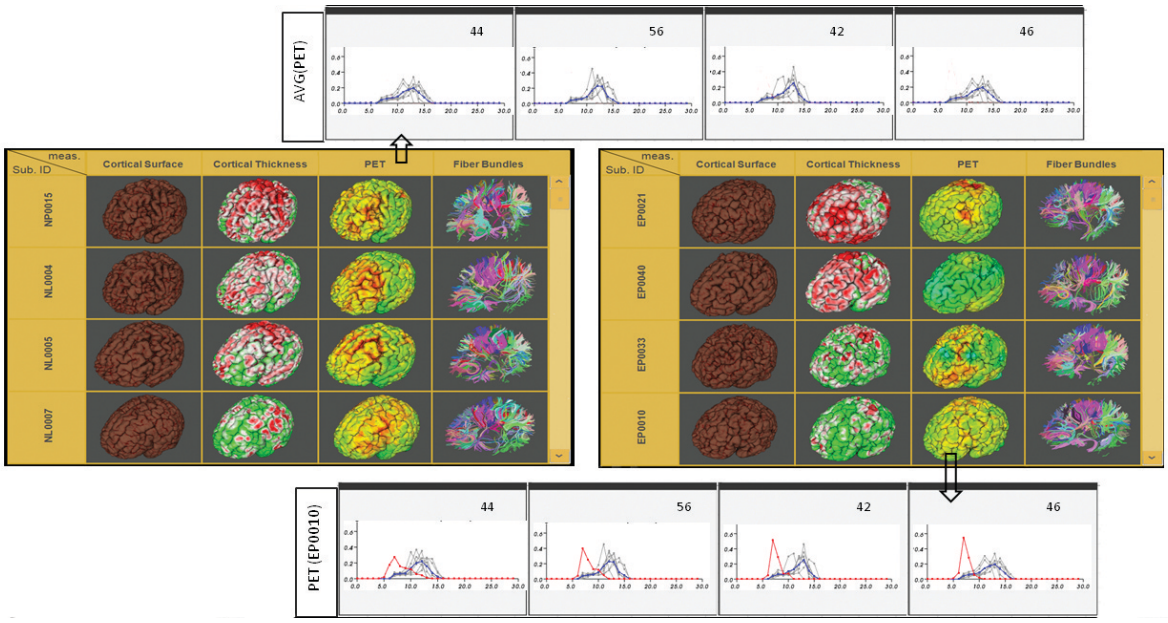

Figure 5.10: The figure shows two tables: the left table is the patient table while the right table is the normal's table. The table is generated after the query for the most salient features output patients with similar disease profile. The normal distribution was selected based on an initial query that specify the criteria for normal subject selection.

lected, the system will generate the statistics and calculate the appropriate rank and map it to a color value. For the histogram-based representation, we use the class consistency measure described in [114]. For two features, we use scatter plots to identify the relationship between them and annotate the representation with the rank variable φ calculated using the formula given in [103]. Figure 5.9 shows the display from the visualization tool for $BAL(e) = 11$.

For γ features, the fiber bundles are selected as measure-valued dimensions. A similar table layout scheme can be used for selecting fiber bundles that are mapped to the rows, and the columns represent the overlapping features extracted from the fiber bundle.

The Coordinated Multi-View Table Revisited: Visualizing Features Across Subject Groups

The exploration of salient features typically starts from a single patient. The significant features are organized according to its anatomical dimension. The spatial locations are filtered initially using the LOD filter, either based on the anatomical labels (BAL or FAL) or the lobes (AL).

The normal subject specification is also selected. This will generate the initial salient feature set that is viewed within the multi-view table layout. To confirm any particular saliency and graduate it to a potential hypothesis, the selected features are formulated as a database query to retrieve, from within the current subject's disease group, a similar pattern for the feature. If a substantial number of patients are found having a similar profile, statistical parametric tests are initiated to confirm whether the hypothesis is true. To verify these insights and exclude patients which do not make sense, scientists will want to view these outputs simultaneously. Figure 5.10 illustrates the result obtained after the formal query is executed, and the results are computed. The figure shows two separate tables. The table on the right lists the patients as a set of rows, with the columns listing the modalities from where the salient features were found for each patient. Each display cell in the table, when in focus, will open a new window that will visualize its salient feature distribution as a 2-D plot and the corresponding normal distribution. Similarly, the table on the left is a table of normal subjects with the same features as columns so that an analyst will also know the source of the normal distribution the patient is compared against. Clicking on the column heading will show the feature distributions of all the subjects in a single window. The analyst has the flexibility to adjust some parameters or reject some of the cases. The application recognizes these changes and recalculates the outputs in real time for immediate reconsideration.

Visualizing Interdependencies between Significant Features

In section 5.5.2 we introduced the Mollweide view for testing the interdependency between features. The details of its construction is described here.

The projection shown in Figure 5.11 is calculated using the equation,

$$x = \frac{2\sqrt{2}}{\pi}\lambda\cos(\theta), y = \sqrt{2}\sin(\theta), \tag{5.1}$$

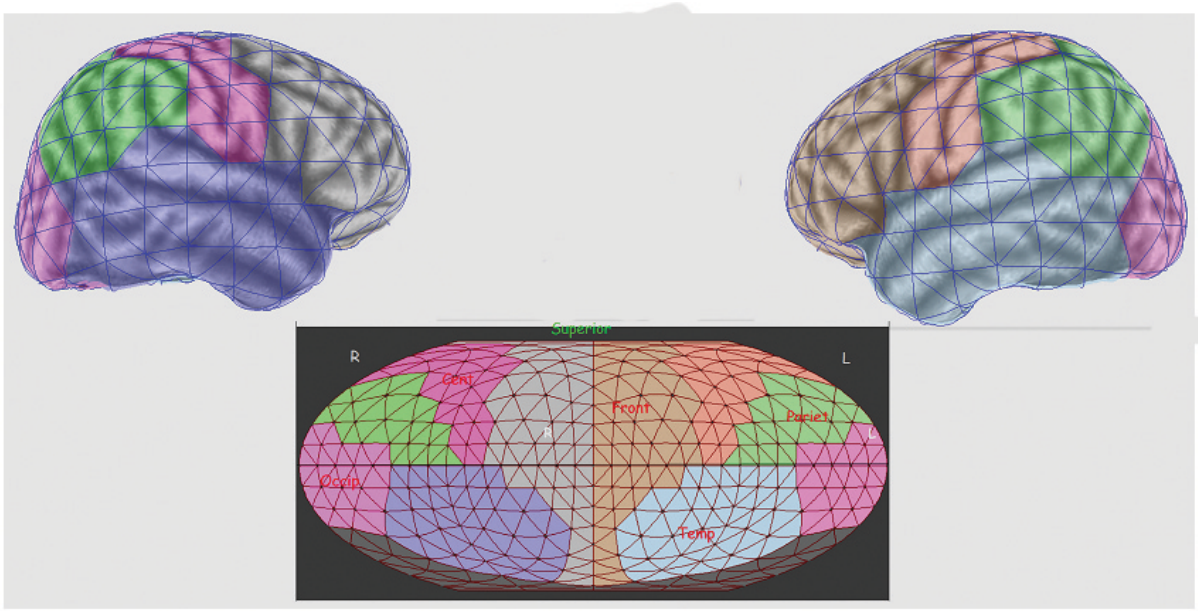

Figure 5.11: The MNI152 brain template which shows the different anatomical lobes differentiated by color. The corresponding Mollweide projection shows the entire brain in the 2-D space. The colors match the corresponding 3-D lobe colors.

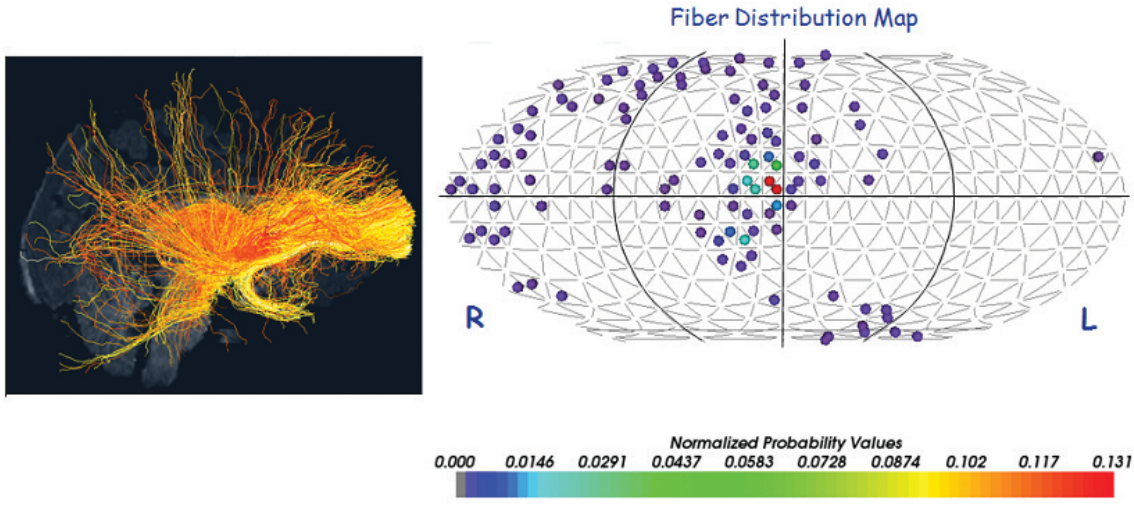

Figure 5.12: Fiber tracts reaching the surface are clustered based on the elements. The fiber distribution map shows the normalized probability score for fibers to reach their corresponding element. The color scale is defined by the color bar below the 2-D map.

where θ is the auxiliary angle defined by

$$2\theta + \sin(2\theta) = \pi sin(\phi), \tag{5.2}$$

and λ and ϕ are the coordinates of a point on the spherical surface. Equation (5.2) is solved iteratively using the Newton-Raphson method to obtain a convergence value for θ as shown:

$$\theta_{n+1} = \theta_n - \frac{(2\theta_n + \sin(2\theta_n) - \pi \sin(\phi))}{2 + 2\cos(2\theta_n)}. \tag{5.3}$$

Figure 5.12, shows an example of the *Mollweide View* that displays neural fibers seeded from voxels within the brain volume that end at the brain surface. The fibers are visually encoded to a sphere placed at the center of the 2-D ROI element. These spheres represent the elements where the fiber terminates. The spherical entities are colored according to the normalized probability values. From the figure, it is clear that the majority of the fibers terminate at the center of the projection where the spherical entities have a reddish hue. Figure 5.17(a) and Figure 5.17(b) show other available encodings used for visualizing features.

5.6 BrainFusion: The Visual Analytics Tool

BrainFusion is a new tool that combines the visual representations and interactions among features described in the previous section. The user interface of BrainFusion is partitioned into several panels (see Figure 5.13). On the left is the *Modality Selector*, for selecting the modalities the analyst wishes to analyze. Next to the *Modality Selector* is a tree view, that lists all the features available for the selected modality. The panel in the middle is the *3-D Brain Viewer* that visualizes the 3-D surface of the brain. There is an option available to switch between the *MPR Slice View* that shows the brain images one slice at a time (see Figure 5.7(a)). The control panel next to the *3-D Brain Viewer* on the right shows a selection panel to choose between one of the three labeling schemes. Underneath the *3-D Brain Viewer* is the *Feature Ribbon View* that shows the features for the selected elements. A slider is connected to the

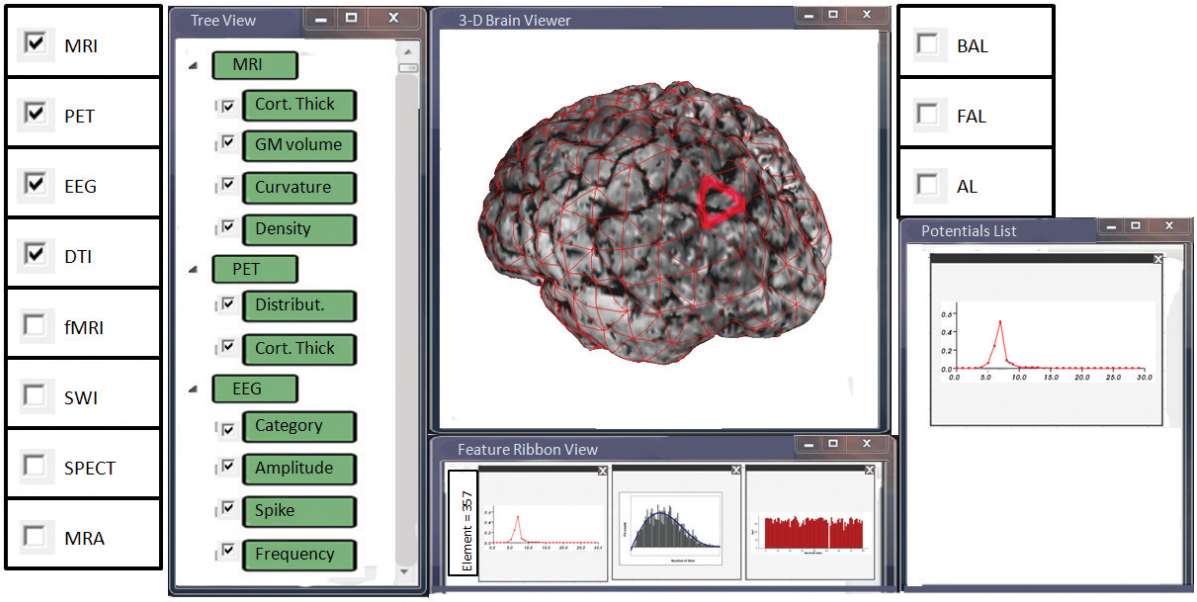

Figure 5.13: The initial BrainFusion window panels are shown.

3-D Brain Viewer that scrolls through the different anatomical labels. As the slider is scrolled, the *Feature Ribbon View* is updated to highlight the selected element features. If no labeling scheme is selected, then the slider will scroll through each individual element. A rubber band widget is provided to dynamically select the elements the analyst wants to focus on instead of the entire anatomical space. Hovering the mouse on any of elements in the 3-D viewer will annotate it with its element index. Features can be easily excluded from the analysis by pressing the **X** button on top of each window in the *Feature Ribbon View*. Interesting features are saved to the *Potentials List* for further scrutiny. A similar interface is constructed for exploring the spatial point features α as shown in Figure 5.14. The different panels in this window are the *3-D Brain Viewer* on the left, with the balls referring to the spatial locations of the α features. The control panel beneath the *3-D Brain Viewer* has multiple options that allow the analyst to select or filter the α features for analysis. The analyst can select the features that are encoded to the size and color of the 3-D balls. The color map widget controls the range of colors assigned to the balls. A color map slider (not shown in the figure) allows the user to update the color range according to his judgment. A summary of the available features is shown in

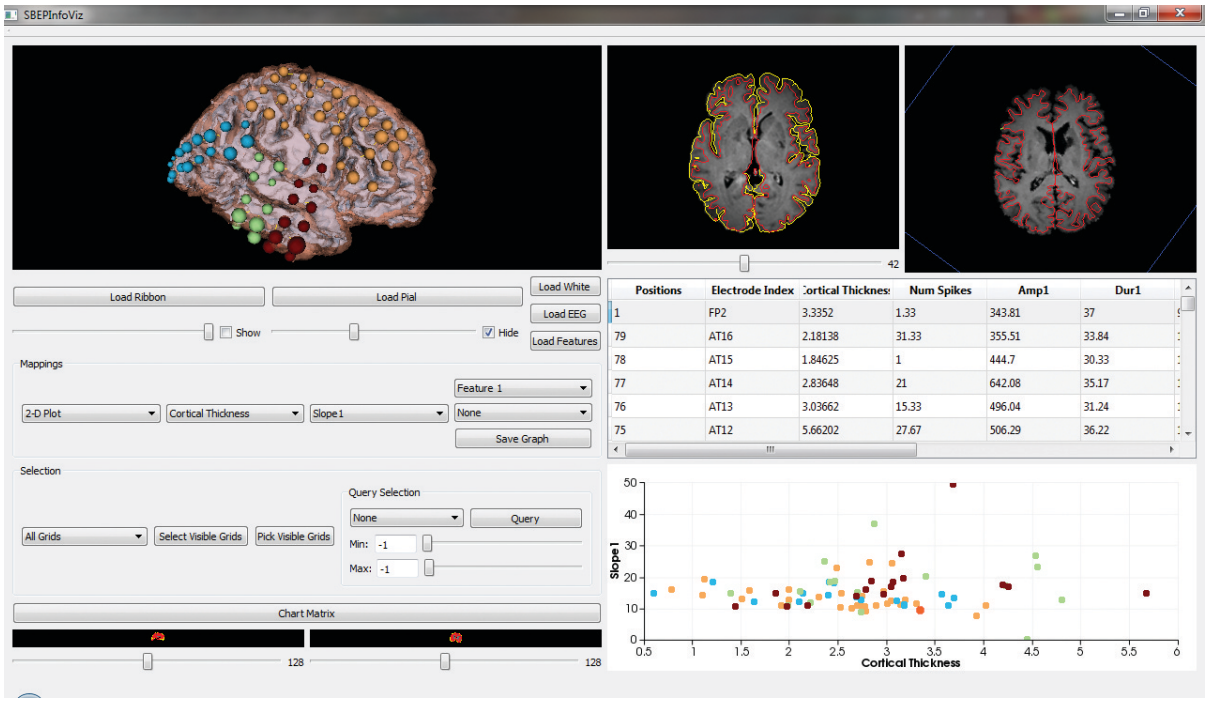

Figure 5.14: The BrainFusion EEG Explorer for analyzing spatial point features α.

the *Information Viewer*. Finally, the *Graph Plot Viewer* shows the different scatter plots for features mapped to the visual encodings. For EEG grids, the plot colors are connected to grid labels that are randomly assigned to each grid. We have four options for visualizing the plots: the histogram distribution, the scatter plots, the scatter matrices, and the parallel coordinate plot. The control panel has a query interface to specify feature intervals that filter the data. The *3-D Brain Viewer*, the *Information Viewer*, and the *Graph Plot Viewer* are coordinated so that the selections in one view updates the other two. When a spatial point is selected, the *Slice View* will show the cortical thickness, and the gray matter density at that location.

5.7 Exploratory Analysis of Correlations Among Features

In this section, we present two case studies where BrainFusion was used for brain disorder studies. The first one shows how BrainFusion identifies the interactions between the features from EEG grid electrodes. The second case study shows how the Mollweide view was used to identify the interdependency between two distinct salient features mapped to different anatom-

ical areas on the brain.

5.7.1 Understanding the ECoG Data Between Seizure Events

Epilepsy is one of the most debilitating diseases in infants and young children under 5 years old. Though most cases can be controlled by strong medications surgery remains the only viable option. Surgeons need to localize the epileptogenic focus of the seizure before they can recommend surgery. The patient is implanted with intracranial EEG grids directly on the brain surface and monitored for at least 24 hours. They record the time of the seizure event and locate the most active electrodes during the event. Based on the observations, the epileptogenic focus is defined, and the decisions are made on the recommended surgical procedure. However, the surgical procedure is not foolproof and may fail to rehabilitate the patient. One frequent cause is that observations failed to locate the secondary focus on the brain surface. To identify this focus we decided to look at the electrical activity of the brain in between seizure events. This data, called the ECoG data, is a set of values that describes the nature of the electrical spikes at each grid: the amplitude, slope, duration, and frequency. The question we posed was: Using the ECog data, can we discover a correlation between electrodes that are classified as seizure onset and the other electrodes?

Analysis

Figure 5.15 and Figure 5.16 show the snapshot of the visualization window that the analyst used to produce the plots for analysis. Figures 5.16(a), 5.16(b), and 5.16(c) show the three scatter plots that have a strong correlation. Figures 5.16(d), 5.16(e), and 5.16(f) show the scatter plots that have the least correlation among them and are excluded from further analysis. As seen in the figure, there is a strong correlation between the amplitude and slope. The frequency vs. amplitude plot shows a correlation at higher frequencies, though at lower frequencies there seem to be some outliers in the plot. This phenomenon was checked within the database, and the table layout visualizes the corresponding results. The analyst does not find these outliers

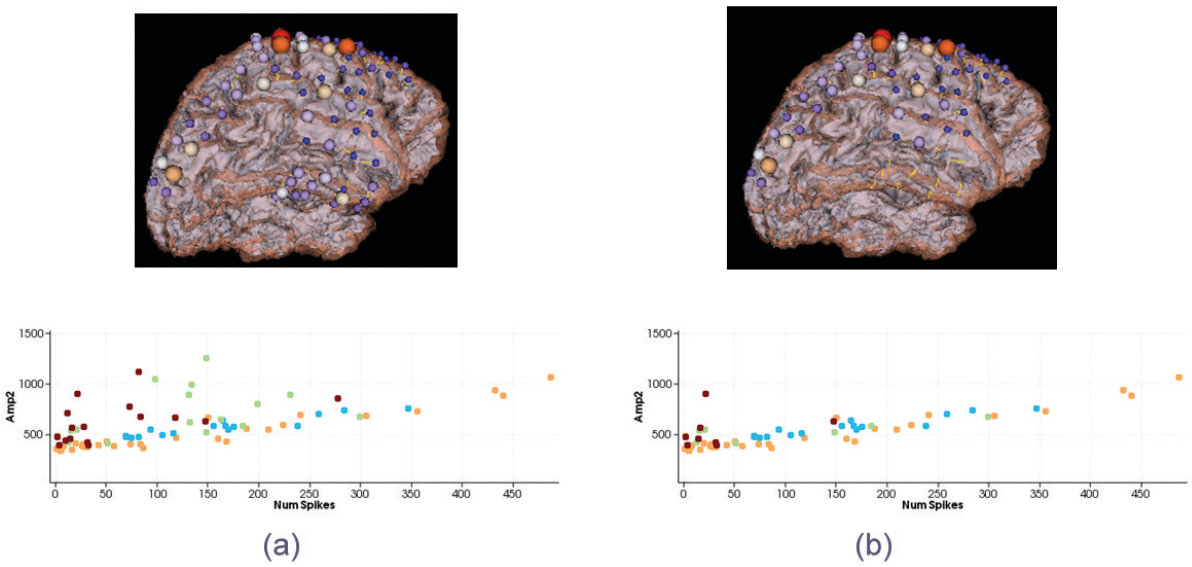

Figure 5.15: (a) shows the initial output between the amplitude and the frequency of the spike. (b) shows the same results after the exclusion of the temporal electrodes from analysis.

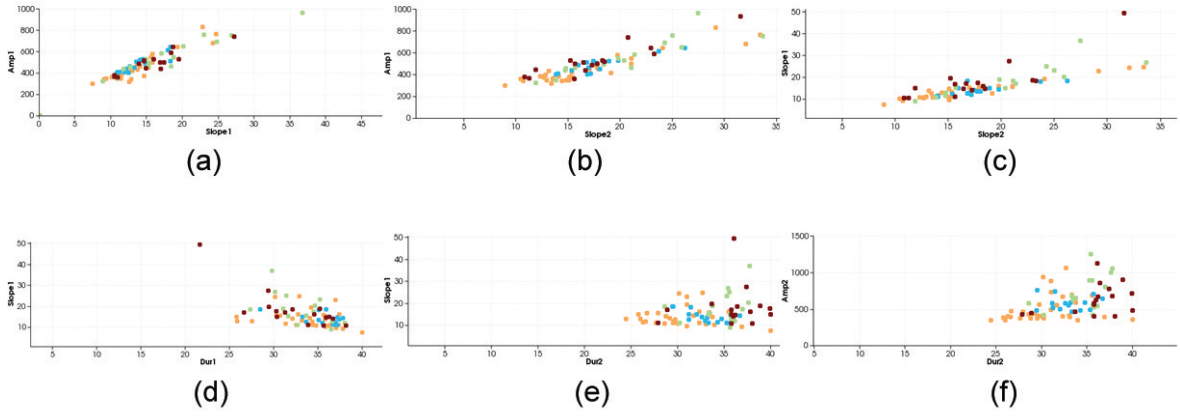

Figure 5.16: The different scatter plot visual representations that show the correlation between different features. The first row of representations has higher correlations values when compared with the bottom row.

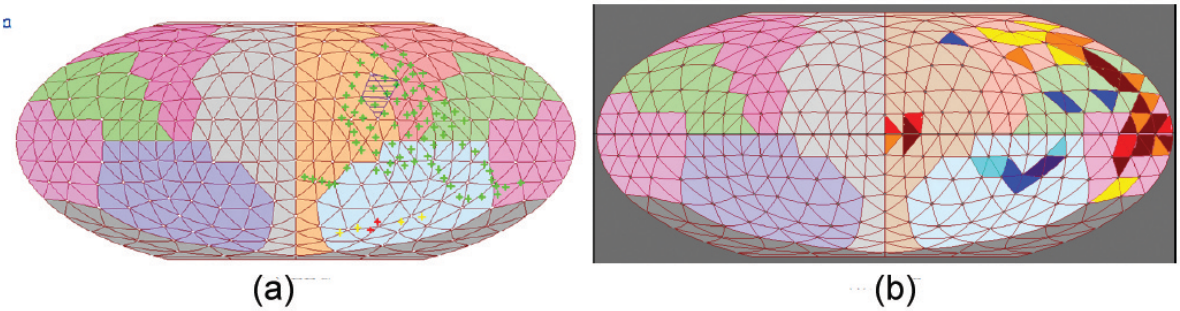

Figure 5.17: (a) and (b) show the projection of the EEG electrodes and the PET abnormalities, respectively.

at lower frequencies. Hence, the analyst looks at one of the patients who did not have the noise at lower frequencies and found that these patients had EEG grids implanted only on the lateral part of the brain surface. The analyst decides to filter the electrodes on the original patient that were not implanted on the lateral part of the brain, as shown in Figure 5.15(b). Once these electrodes were excluded, the result showed a much better correlation between the frequency and the amplitude. When compared with other subjects in the database, the result agreed with most of the subjects with lateral grids. From the analysis, we discover that there is some phenomenon that affects the amplitude for lower spike frequencies along the temporal region. After the specific relationships between the amplitude, slope, and spike frequency was successfully concluded, the seizure category information was selected to identify onset electrodes.

We discovered that electrodes, which are not onset, are very strong candidates for being the secondary focus because they have a similar spike profile. The relationship could not be perceived using the 3-D spatial representation alone and had to be augmented with information visualization schemes .

5.7.2 Analyzing the Interdependency Between PET and EEG Features

Brain disorders such as tumors, concussions, and brain lesions induce seizures in the brain. The abnormalities associated with seizures are measured using PET and EEG modalities. PET

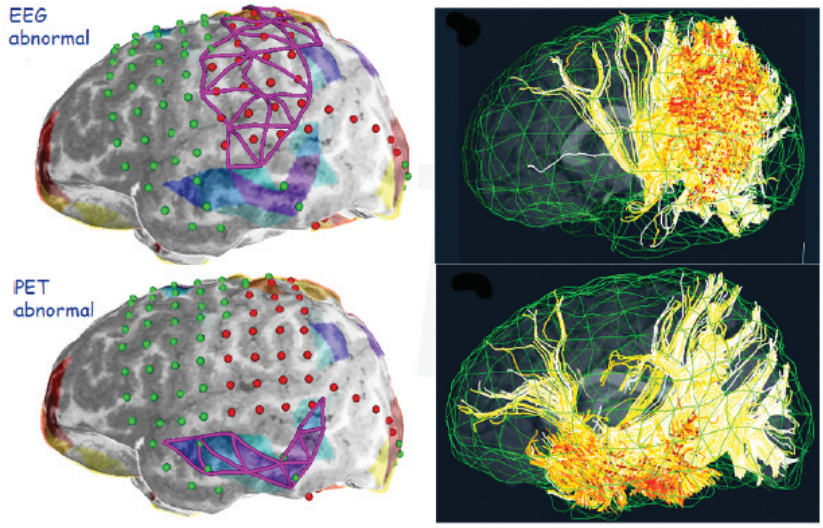

Figure 5.18: Surface rendering of the patient's brain with an extensive epileptic focus in the left central territory and the definition of the ROI elements representing the seizure onset area (a) and the PET abnormality (b). The cortical elements are color-coded based on the number of standard deviations (SD) above (yellow and red) or below (blue and purple) the normative PET tracer concentration derived from the normal group. The PET abnormalities can be assessed with respect to the seizure onset electrodes (red). The cortical elements defined were used as source regions for probabilistic fiber tracking yielding a fiber distribution pattern for the whole of the cortex (b) and (d).

images measure the metabolic activity in the brain and the EEG measures the electrical activity. Both of these images are independent measurements and the significant areas do not necessarily localize in the same anatomical area. There is no clear indication about any relationship between the two outputs. Scientists were eager to use BrainFusion to test whether the DTI image that connects the surface elements via cortico-cortical fibers will identify this relationship. The question we intend to confirm was: Is there any interdependency between the features derived from the PET modality and the features derived from EEG?

Analysis

The analyst loads the patient data and chose the PET image and the EEG image from the *Modality Selector* panel. The analyst then selects a normal subject group with 10 data sets.

This generates the initial table layout that shows the histogram distribution (feature type β) as the most significant feature for PET. The PET abnormalities are selected to be visualized in the 3-D Brain viewer along with the onset feature α derived from EEG. The two features do not correlate anatomically and is suspected to be the result of functional disconnection from ictal involvement [2]. The analyst decides to use the *Mollweide view* to explore any possible interdependencies. It selects the DTI image in the *Modality Selector*, and selects two DTI fiber bundles visualized in Figure 5.18. The first bundle $gamma_1$ uses the PET abnormal elements as the seed voxels, and the second feature $gamma_2$ uses the EEG abnormal elements as the seed voxels. To visualize these features in the *Mollweide view*, the PET feature was encoded to the element color, mapped to the divergent color map range [blue,red] (Figure 5.17(b)). The EEG feature was encoded to the crosshair symbol (Figure 5.17(a)). The crosshair was colored based on the seizure category: red represents the onset electrodes, green represents the spread electrodes, and gray represents the normal electrodes. The fiber end points were encoded as spherical balls and a rainbow color map visualizes the connectivity values for each element.

Figures 5.19 and 5.20 visualize the results. The analyst wanted to check whether fiber distribution patterns for the $gamma_1$ and $gamma_2$ change significantly between the normals and the patient. Figure 5.19 shows the comparison between the patient's cortical fiber distribution pattern of fibers $gamma_2$ that originates in the seizure onset zone and the fiber distribution for the same source region in the normal group. Although the average intraclass correlations were not significantly different ($0.84\ vs\ 0.85,\ p = NS$), individual analysis of anatomical territories showed a significantly lower normalized connectivity score in the patient's frontal lobe as compared to the normal group ($0.0056\ vs.\ 0.023 \pm 0.004,\ p = 0.03$; one sample *t*-test). Similarly, for $gamma_1$ as the source region (Figure 5.20), we found a lower normalized probability score in the patient's frontal lobe as compared to the normalized probability score in the frontal lobe derived from the normal population ($0.0095\ vs.\ 0.0263 \pm 0.006,\ p = 0.04$; one sample *t*-test). In addition, the average intraclass correlation was significantly higher in the

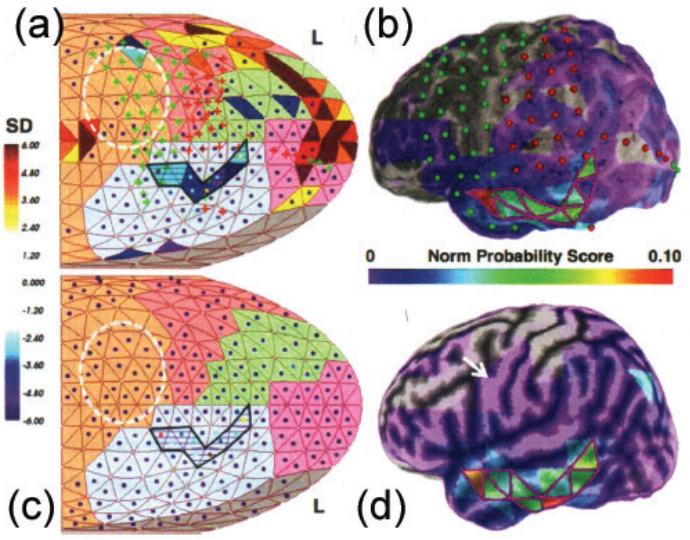

Figure 5.19: An integrative analysis of EEG, PET and DTI data in 2-D. (a) shows the 2-D map of the patient's left hemisphere and shows the proximity of seizure onset (red +) as well as electrophysiologically normal (green +) electrodes to abnormally decreased (blue and purple) and increased (yellow and red) PET tracer concentrations. Seizure onset electrodes are depicted as a black-boarded area, the source for probabilistic fiber tracking. The obtained normalized probability score values are rendered as small dots in the center of the finite elements and color-coded in the range [0-0.12]. (b) shows the corresponding surface view of the source elements used for probabilistic fiber tracking and the normalized probability score rendered onto the cortical surface together. (c) shows the 2-D representation of the average distribution pattern of the normalized probability score derived from the normal group. Statistical analysis revealed a significantly higher probability score to the frontal lobe in the normal group (white broken circle, see text for details). (d) shows the corresponding surface view similar to (b). Increased number of finite elements with nonzero probability score in the frontal lobe can be seen (white arrow).

normal group when compared to the patient ($0.87\ vs\ 0.77,\ p = 0.03$), indicating an abnormal fiber projection pattern from the patient's temporal lobe. To identify whether these patterns were consistent among other patients suffering from a similar ailment, the analyst queried the database to list cases with a similar thinning of fibers in the frontal lobe, and found six older cases. This discovery was significant and can be directly tested in newer cases by adding it as a measure-valued dimension in BrainFusion. We could successfully identify an interdependency that failed to show up in the 3-D spatial representation.

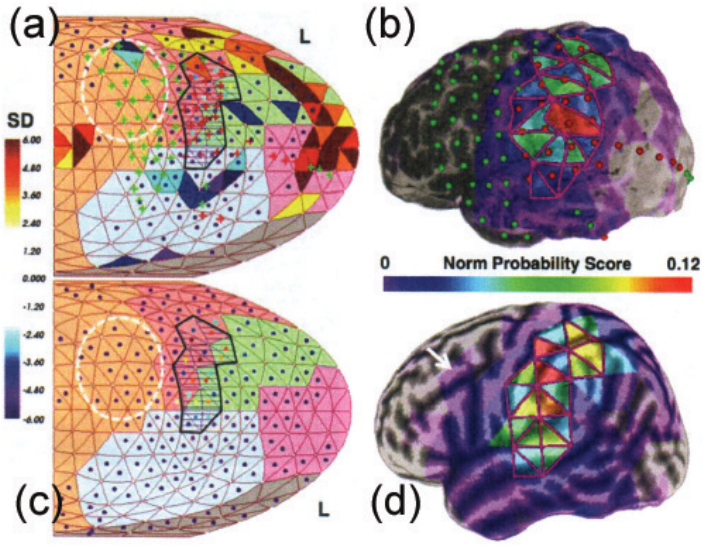

Figure 5.20: Similar display to Figure 5.19, but showing the normalized probability score distribution pattern of a source region characterized by abnormally decreased PET concentration (black-boarded area in (a) and (c)). (a) shows the 2-D map of the patient's left hemisphere showing the distribution pattern of normalized probability scores originating from the PET abnormality. (b) shows the corresponding surface view showing all source elements used for probabilistic fiber tracking and the normalized probability score rendered onto the cortical surface. (c) shows the 2-D representation of the average distribution pattern of the normalized probability score values derived from the normal group. Statistical analysis revealed a significantly higher probability score to the frontal lobe in the normal group as was determined for the patient (white broken circle). (d) corresponds to the surface view similar to (b). Again, an increased number of finite elements with nonzero probability score in the frontal lobe was observed (white arrow).

5.8 Evaluation of Brain Electrophysiology via Temporal Spike Events

EEG is the benchmark modality for electrophysiological analysis in the brain. Seizure activity is always debilitating, affecting the quality of life. Resection surgery is the only viable option available with a success rate of approximately 60%. The low prognosis outcome is mainly attributed to the difficulties associated with information that is not apparent during seizure episodes - for example, the emergence of the secondary epileptic focus after the resection of the seizure onset locations. Although seizure events actively delineate locations of seizure

onset and spread, noticeable spike discharges are recorded in between seizure events. ECoG reports the spike profile at each channel. We have compared ECoG features (section 5.7.1) and found interesting correlations among them. A glaring omission is the transfer of spike discharge across electrode channels over certain time intervals. These spike propagation events maintain the state of the brain before seizure. Neuroscientists speculate the possibility of mapping the affinity of prolific spike propagations to the seizure onset areas. We also want to ascertain the role of the brain surface structure and tissue variation to influence the propagation path. The following sections evaluate optimized visual representations for presenting this data.

5.8.1 2-D Visual Representation for Encoding Propagation

Spikes are detected by an in-house DSP script written in Matlab. An expert neuroanatomist will choose certain time intervals of high spike discharge and record atleast three levels of spike propagation; each level represents an electrode channel. Any propagation past the third level loses enough energy to be prone to diffusion and is typically ignored. A typical visualization of the propagation events, as connecting lines, on the brain surface does not reveal any information because of overlap. Moreover, the occlusion makes identifying the most common propagation pattern very difficult. We devised a 2-D representation that reveals this information clearly and provides a filter to segregate the interesting patterns. We illustrate the visual representations (seen in Figure 5.20) that encode the propagation events and evaluate its usefulness.

Projections

Figure 5.21(b) is a layout that was inspired from the Parallel Sets technique first detailed in the paper by Kosara et al. [74]. The visualization only shows propagation at three levels. The dimensions are depicted as horizontal lines, and they all represent electrode channels. However, the meaning of the dimensions differ at each level. The top-level dimension is called the *Initiation* and it arranges electrodes according to the number of spikes that originate from

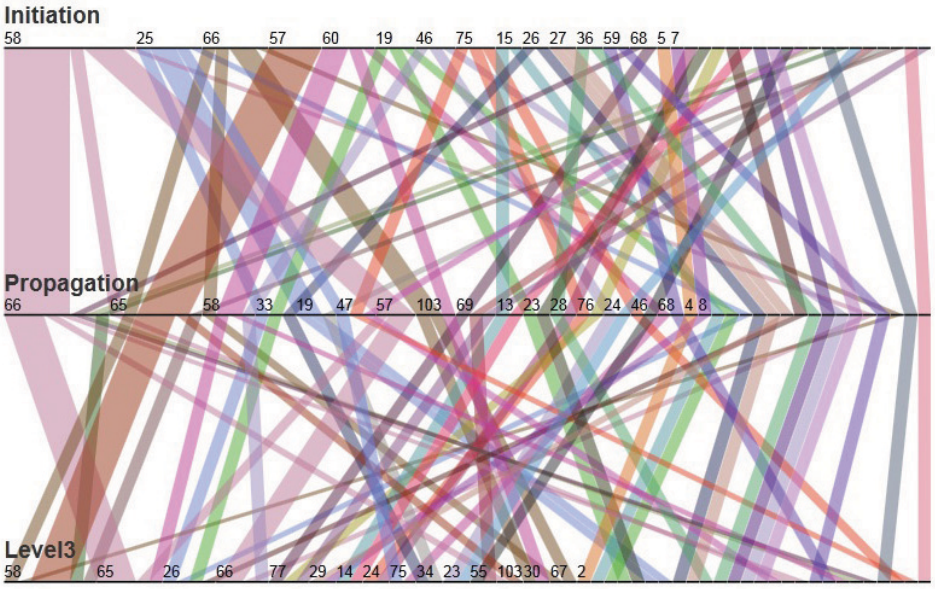

Figure 5.21: Visualization inspired by Parallel Sets.

that electrode. The second dimension is called the *Propagation*, and it orders the electrodes according to the number of spikes that the electrode receives. The last dimension is called the *Level3*, and it orders the electrodes according to the number of spikes it receives from the *Propagation* dimension. The direction of the propagation is from top to bottom. The top-level electrodes are categorized by distinct colors, and these colors are used to encode the propagation events that start from the corresponding electrode and spread to the other two levels. For example, electrode number 58 initiates five spikes that propagate to electrode 66 and bifurcate into three separate paths, three spikes going to electrode 65 and the rest splitting between 103 and 73. The path is labeled with a pinkish hue. The width of the links between the dimensions are encoded with the percentage of total spikes. Each electrode is represented by a line within its dimension, and its length is encoded to either the originating spike frequency for the *Initiation* level or by the number of spikes received for the *Propagation* and the *Level3* dimensions. The visualization is interactive, and every action reveals important information about the data. For example, the electrodes within each dimension can be ordered in ascending as well as descending order. The drag and drop events allows the user to manually arrange

the electrodes within each dimension. The mouseover function annotates each electrode with the spike frequency and the percentage of total spike values and the connection paths with information about the origin, destination, and the number of spikes traveling between them. If a particular connecting path is directly under the mouse pointer, the visualization will fade out the other paths as a means to highlight the path in focus and reduce occlusion.

Response

We conducted a user study to qualitatively determine the effectiveness of the Parallel Sets representations and gauge the response regarding its usability. The comments were as follows: The Parallel Sets technique was unanimously selected by all participants because it clearly visualizes all the paths. All the paths are differentiated by colors and perceived clearly even when there is an overlap between them. The thickness of the paths and the dimension ordering clearly visualize significant events, and the direction of the spike is also implicitly encoded. The scalability was not an issue since more levels can be added as needed. The user study results skewed very strongly toward the Parallel Sets representation.

5.8.2 3-D Spatial Brain Representation for Encoding Propagation

The 2-D Parallel Sets representation draws attention toward the following patterns listed below:

1. Some electrodes are active spike initiators and discharge more often compared with other electrodes.

2. Some electrodes actively accumulate spike discharges from multiple initiators.

3. The most active initiators and accumulators have prominent cross talk with each other.

These patterns are an interesting find, but the lack of anatomical context does not make it very beneficial for analysis in the 2-D representation. The goal is to gain an understanding of the pattern in the physical brain surface, thus examining the structural details and its relation to the

spike propagation. We built a representation that will allow the user to navigate through the different patterns in the 3-D physical space. Figure 5.22 shows the 3-D visualization, enhanced for presenting the selected patterns. Three different surfaces are used. The first surface is the smooth textured surface for projection of the EEG grids. The pial surface is the high-resolution brain surface that shows the different folds on the brain surface, namely, the sulcus and the gyrus. The white matter surface is the visualization of the boundary between the white matter tissue and the gray matter tissue. Together, the white matter and the pial surface decode the thickness of the gray matter along the surface. The pial surface parameterizes the true distance between two points on the brain surface and helps calculate the true propagation distance. On the brain surface itself, propagation events are visualized using pointed arrows. The arrows are colored based on whether the user wants to focus on the initiator (green) or the accumulator (red). The arrows can be either straight or curved and the width of the arrow can be encoded to the number of spikes. For any particular path, the initiator electrodes are always visualized by a bluish green hue as shown in the figure. Accompanying the 3-D representation, we provide a table view that lists the current propagation events being visualized, along with a selection query interface that allows us to select propagation events based on the number of originating spikes, number of spikes received, or the percentage of total. Individual events can also be selected, and there is no restriction on the number of events visualized at a given time.

5.8.3 Graphical Layouts for Analysis

The 3-D representation is supplemented with graphical plots that are specifically designed to make it easy for the user to perceive the structure surrounding the selected electrodes. ECoG features along propagation paths can also be encoded within the plots to look for specific comparisons to the structure. Figure 5.23 illustrates the various plots. The first plot, Figure 5.23(a), is the parallel coordinate representation. All three dimensions are encoded to the same measure, though the values for each dimension refer to the propagation path. The measure can be dynamically selected by the user and can be either the cortical thickness value or one of the

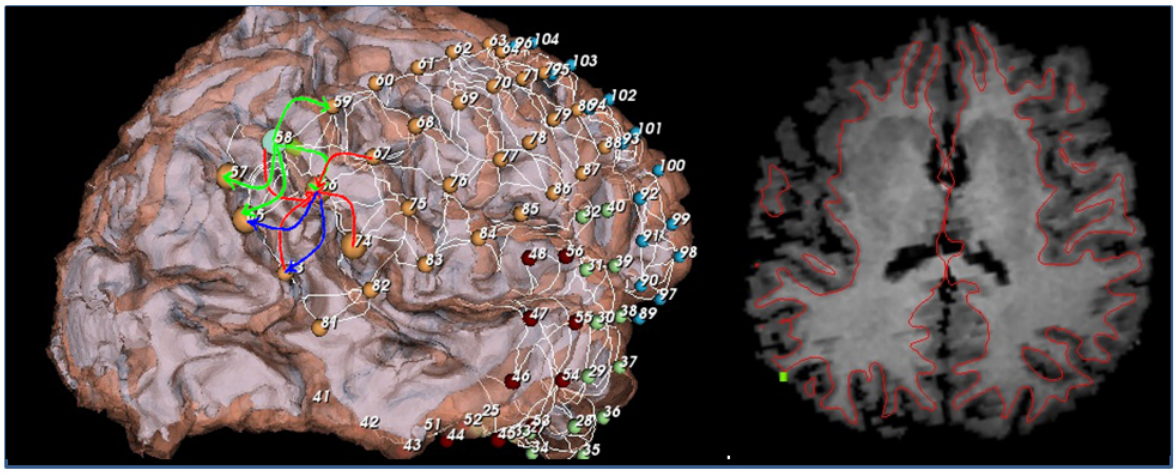

Propagation Events	Number of Spikes	% of Spikes
58-66-73	39	8
58-66-65	20	6
58-59-60	5	2

Figure 5.22: Illustration of a 3-D representation of a propagation event starting at 58. The arrows starting from the initiator 58 are colored green. The user can choose to concentrate on the accumulator. The figure shows event paths for accumulator 66, which are colored red. The white lines in between electrodes is the geodesic distance between them. The cortical thickness under the electrode is shown using the green tube on the 3-D surface and also on the slice as shown in the figure on the left for electrode 58. The table below lists the links that are visualized on the surface, at any given point.

ECoG features. The second plot, Figure 5.23(b), is a distance plot which is a variant of the area plot. The X axis is plotted from 0 to 1 and refers to the parameterization of the geodesic curve between adjacent electrodes. Along this curve, the thickness values are sampled and represented as an area distribution across the X axis. Each electrode has, at most, eight such area plots corresponding to its adjacent electrodes. Each area plot is annotated with the electrode index on the left and right. The area plots are visualized in a hierarchical pattern following the propagation. The area plots can be shaded with one of the ECoG features that encode the interpolation of that feature along the path. The third plot, Figure 5.23(c), is the multidimensional scaling (MDS) plot that projects the grids in 2-D space based on the geodesic distances between adjacent electrodes. The propagation event currently visualized in 3-D is connected

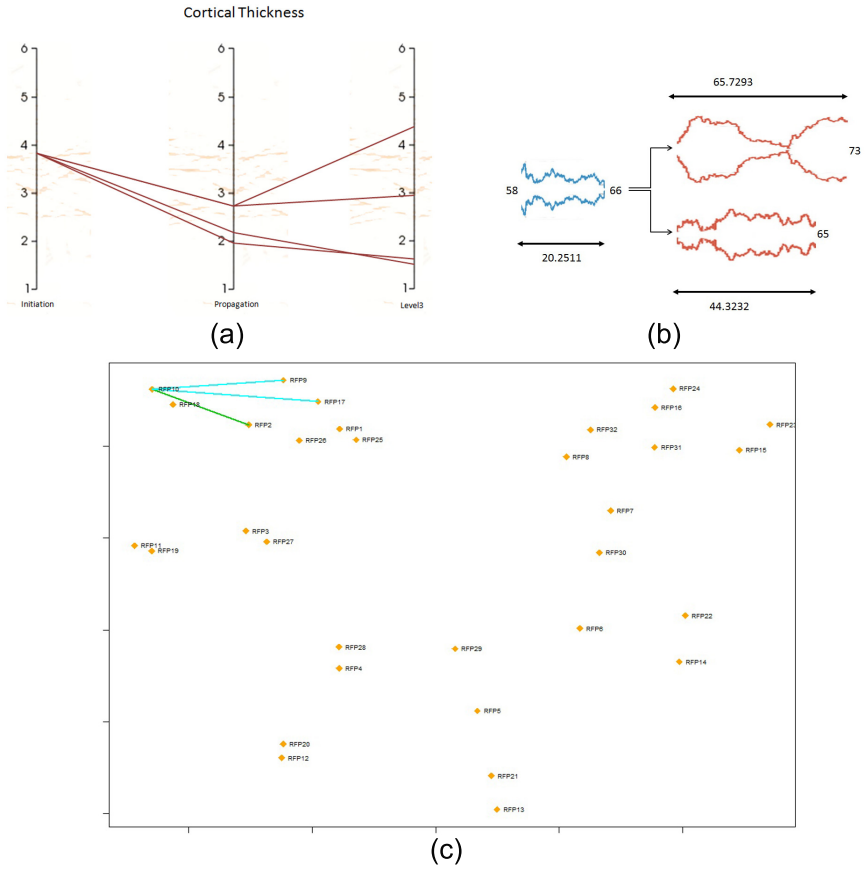

Figure 5.23: (a) Parallel coordinate representation for cortical thickness. (b) Area plots for visualizing geodesic distances. (c) MDS plot for the EEG grid. The connected lines denote the propagation events, with the line color differentiating between electrodes either on the gyrus (olive) or across the gyrus (light blue).

using line segments. The lines are annotated with the geodesic distance, and the line color is chosen depending on whether it is at grid length (olive), on the same gyrus (orange), and across the sulcus (light blue).

5.8.4 Evaluation Study

We conducted a user study to determine the effectiveness of our information visualization interface designed for the analysis of spike propagation events. We want to rate the different representations of data in terms of its efficiency, performance benefits, and ease of use. We have designed certain tasks to test whether the visualizations help the user to clearly display

spike propagation data within the context of the brain surface features. In other words, we aim to understand whether the visualization interface improves or optimizes the information content for making decisions with higher confidence. To successfully complete our study, we took the help of medical practitioners who are well trained in brain anatomy. We also chose to work with real subject data so that we get a sense of any external factors that may affect the visualization.

Hypotheses

Our hypotheses for the user study were:

- **H1:** The combination of 2-D and 3-D representation results in the most effective mechanism for filtering and displaying the most frequent spike propagation events.
- **H2:** The cortical thickness area plot along the geodesic distance results in fewer errors for pairwise electrode selection that cross sulcal boundaries.

User Interface

The apparatus for the study involved the use of a Windows 7 desktop. The prototype application for the study was built using a fork from the BrainFusion application that visualizes EEG grids. We used the data from an adult patient afflicted with epilepsy. The CT imaging data was used to extract the electrodes, which were transfered onto the MRI using a 3-D projection algorithm. The smooth brain surface extracted from the MRI was visualized alongside the projected electrodes and labeled based on the grid locations. The pial and white matter surface was extracted from the MRI image to generate the cortical thickness distribution. The 2-D representation was developed in OpenGL-ES and SVG and displayed in a browser and the 3-D representation was displayed in a Qt Viewer developed in-house using VTK, Visual Studio, and C++ as the programming environment. Apart from the application itself, the participant is allowed use of other tools for completing the tasks successfully. Some tasks ask for the

participant to use common Windows applications, but he has a choice to decide which one to use. For manual processing, we provided participants with pen, paper, and calculator as requested by the participant. We recorded the time taken by each participant to complete a given task. At then end of the task we quizzed the user so as to gather their inputs on the visualization style, their preferred visualization output, and other comments and feedback regarding the application.

Participants

We decided to have a varied background for the participants included in the study. Since the study will require medical literacy and knowledge of brain anatomy and disease, we only included participants who are either trained to be medical experts in brain anatomy and disease, or have atleast the basic knowledge to fully understand the tasks that need to be performed. There is no bias regarding the visualizations that will be used in the study because the technique presented here is not part of standard practice. Six personnel participated in the study. The list included two medical researchers, one advanced graduate student, a first year student, and a postdoc. One participant was chosen who did not have a medical background, but has worked in the medical domain for several years. The participants were given a demonstration of the software environment and some background material about the usage and details about the study. Once the participants were ready, we gave instructions for performing each task. After the end of each task, we measured the time taken to complete the task and also accessed the responses to each task.

5.8.5 Tasks and Procedures

We have different tasks for each hypothesis. We briefly describe the tasks in the sections below.

Experiment 1

For the first experiment, we designed three tasks for each participant to perform. We recorded the time taken to perform each task, and accessed the difficulty level of each task through verbal responses at the end of the task. For the first task *T1.1*, the electrode labels and the propagation data was provided as a tabulated file and the participants were asked to use their tool of choice to sort the data in ascending order, starting with the most prolific spikes. We suggested certain tools for the sorting task, namely Microsoft Excel, GNU R, and Data Wrangler [67]. They were also given the choice to use pen and paper to sort the propagation events. After the sorting, the user has to identify the electrodes on the 3-D brain. A 3-D brain viewer, displaying the brain surface and the electrodes, was provided with a click and select option. The user selects the electrodes based on the output of the sorting. For the second task *T1.2*, the participants were allowed the use of the 2-D representation (Figure 5.21). They could load the data into the 2-D browser and use the interaction tools to sort the electrodes based on size, as described in section 5.8.1. The use of 3-D environment was still restricted to a click and select option as described for the first task. The final task *T1.3* allowed the use of both the 2-D and the 3-D representation (Section 5.8.2). The representations are coordinated to each other and the selections can be interactively seen in 2-D and 3-D simultaneously.

Experiment 2

For the second experiment, the participants were given two tasks to perform. In the first task *T2.1*, a 3-D viewer displays the brain surface with electrodes. The electrodes are indexed with channel numbers and the participants were asked to record an adjacent electrode pair crossing the sulcal boundary. For each observation, the participant will also record the confidence regarding his choice. In the second task *T2.2*, for every pair of adjacent electrodes, the user can query the system and visualize its corresponding cortical thickness area plot (Figure 5.23(b)). The distance between the two electrodes can either be based on the linear distance or the

Experiment 1	Mean
T1.1 (no 2-D / no 3-D)	45 minutes
T1.2 (2-D / no 3-D)	10 minutes
T1.3 (both 2-D and 3-D)	2.5 minutes

(a)

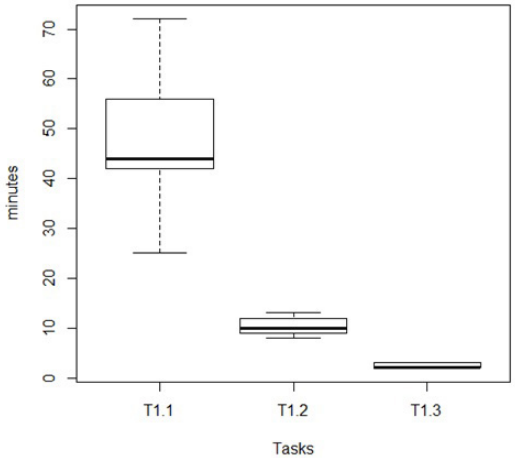

(b)

Figure 5.24: (a) Table displays the average time for each task in experiment 1. (b) A box plot representing the distribution of the time-to-complete for experiment 1.

geodesic distance. A very good indicator of the sulcal boundary is an apparent thinning of the cortical thickness, which acts as a strong indicator that can influence the selection criteria. The goal of this task is to use the area plots as an additional resource for selecting adjacent electrode pairs with a sulcal boundary in between. The participants record the confidence level for the selection for this task too. At the end of both the tasks, participants were asked specific questions regarding the usefulness of the plot.

5.8.6 Results

Efficiency

On average, for experiment 1, the participants spent the most time for the task *T1.1* $(mean = 45minutes)$, and the least time on the task *T1.3* $(mean = 2.5minutes)$. For the task *T1.1*, we also noticed that most participants used Microsoft Excel for their calculations mainly because of its familiarity. One participant chose to use GNU R and finished *T1.1* in under 25 minutes. One participant chose to do it manually and took the most time. He also made an error in his calculation, which caused him to choose wrong electrodes in the 3-D view. The time spent in identifying the electrodes in the 3-D view was roughly the same across all participants

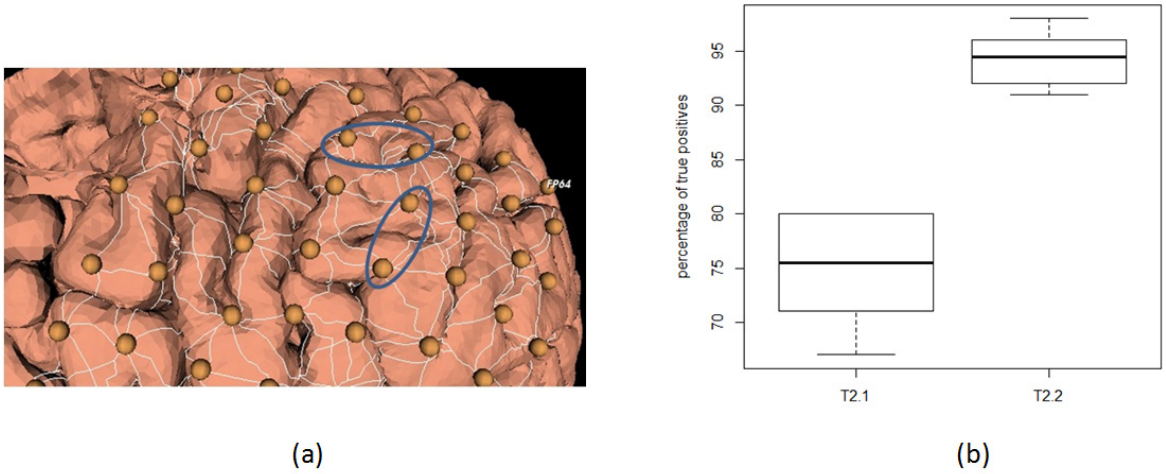

Figure 5.25: (a) The blue circles indicate instances where electrode pairs are wrongly classified as crossing a sulcal boundary (b) A box plot representing the true positives distribution for each task in experiment 2.

$(mean = 8minutes)$. Maximum time was spent on locating the electrodes in 3-D using the mapping information provided in the file.

For the task *T1.3*, a couple of participants decided to start from the 3-D representation. They used the query interface to filter the initiation electrodes with the highest spike count, but could not choose all relevant paths until they referred to the propagation data in the 2-D browser. All the participants noted in their comments section about the benefits of having a 2-D as well as a 3-D representation for displaying the most frequent spike propagation data. In Figure 5.24(a), we list the mean time-to-complete for each task. Figure 5.24(b) shows the time distribution as a box plot, with the error bars indicating the maximum and minimum time for completion.

Accuracy

For experiment 2, we found that on average 77% of electrode pairs crossing sulcal boundaries were identified correctly for task *T2.1*. Advanced participants, because of their medical expertise, overall fared much better when identifying the correct pairs. However, we found that with

the addition of the cortical thickness area plot in task $T2.2$, the accuracy increased to nearly 94%. This was due to the increased confidence in the participants selection. The areas plots clearly allowed the participant to look at the cortical thickness along the geodesic path. It is well-known that the thickness between gray matter and white matter is minimal at the sulcal boundary. This additional information increases the confidence level of the choice. It also allowed us to eliminate false positives in some cases where the folding structure incorrectly perceived itself as crossing a sulcal boundary, as shown in Figure 5.25(a). For the tasks *T2.1* and *T2.2*, we show the box plot indicating the true positives distribution (Figure 5.25(b)) across participants. The bars indicate the maximum and minimum percentage of the distribution.

5.8.7 Discoveries

We use our visualization program to focus on two adult epileptic subjects with an intent to highlight any interesting patterns. Specifically, we wanted to confirm the following two questions. The first question was: Do spikes propagate more between electrodes on the same gyrus, or it prefers a path that crosses the sulcal boundary between two electrodes? We second question was: Do any of the ECoG feature influence the spike propagation path?

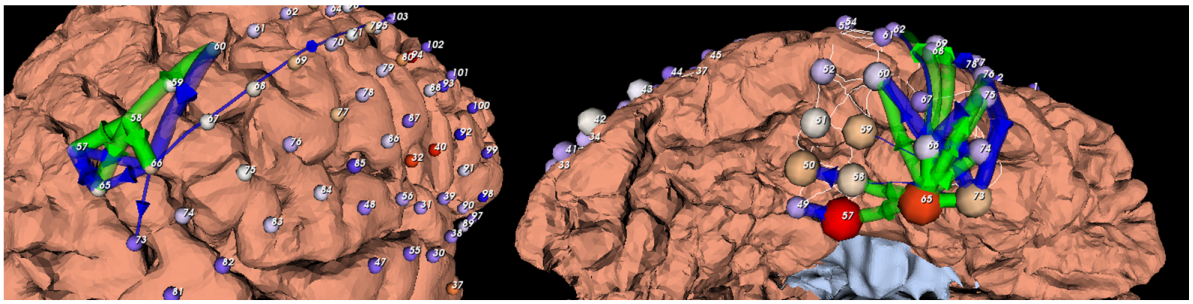

(a) (b)

Figure 5.26: Propagation of EEG spike events for two representative patients.

Figure 5.26 displays the snapshot of two brain data sets. The propagation paths are visualized for an electrode that has the highest number of spike initiations. The left figure indicates that the spikes tend to propagate along the electrode within the first neighborhood set. The

MDS plot shows no preference for paths traveling across a sulcal boundary or moving within a gyrus. We decided to map the spike count to the width of the propagating line segments. We found that the number of spikes propagating to an electrode is higher when the electrodes are on the same gyrus. For example, electrodes 58 and 66 lie on the same gyrus and have a larger spike count between them. The other electrodes that receive the spike from 58 have a lower path value. Another observation for the data set on the left is that there is no propagation between electrodes 58 and 67 even though they are adjacent and belong on the same gyrus, a phenomenon we cannot explain.

The right figure was interesting because the spike paths tend to propagate past the second neighborhood, with the same intensity. We speculate whether any of the ECoG features was responsible for this pattern. We load the ECoG features and found that the amplitude of the spike was very high in this area. This indicates an influence of the amplitude on the spread of the spikes as shown in the figure. Both cases show that the propagation always prefers a path in descending order of the amplitude.

5.9 Summary

BrainFusion presents medical scientists with a tool that combines different visual components and enhance their ability to navigate and explore the entire high-dimensional space of the image modalities. We explained the framework in detail and illustrated some of our analysis using case studies. The *Mollwiede view* was very well received by the clinical staff because the 3-D brain could be visualized in 2-D. Representing different features by encoding it to visual entities helped uncover patterns which were not perceivable before. The coordinated multi-view table layout visualized all the high-dimensional features in one convenient location. The display panes were interactive and highlighted the significance of all the features, including the statistical output.

CHAPTER 6

CONCLUSION

Medical image analysis is currently at the forefront of human brain research because of rapid advances in hardware acquisition and storage, and it produces high-dimensional and multiresolution functional and structural images. The human brain is an intricate system of complementary biological processes, and each modality qualitatively abstracts certain aspects of these varied processes and characterizes them as high-level brain functions. Brain disorder studies apply computing models for feature selection and extraction from within the images, but it is labor-intensive and time-consuming to identify and analyze a significant set of features that describes abnormal behavior. Visualization tools provide the 3-D spatial context for representing features in the physical domain and are used for effective knowledge transfer through an insightful visual representation of the significant results. As the dimensionality and the data set size increase beyond the point of the cognitive threshold, the feature exploration step needs a more data-driven approach for accurate hypothesis generation. Our visual analytic framework addresses these shortcomings through a systematic and interactive process of identifying features and their interdependencies and helps discover and confirm new hypotheses on demand. This approach involves human insight at both the exploration level as well as the verification level, as knowledge acquired translates to the domain-level significance prevalent among subject groups. We list the research contributions that we have designed and developed that present a systematic methodology for multi-modality integration. We conclude this chapter with a section on the future direction within the field.

6.1 Contributions

In this dissertation, we first derive a rigorous angle preserving, surface matching algorithm for the robust alignment of brain surfaces. The unit of analysis is generated by a categorical

subdivision of anatomical elements, and it forms the spatial dimension for structuring multiple features extracted from multiple modalities not limited to DTI, EEG, and PET. Pooling the different data sources across subject groups and analyzing for abnormalities provide domain-level significance. As overlapping features are composed into a high-dimensional vector, analytical processing frameworks provide the necessary tools for exploring the significant relationships and acquire knowledge. Our contributions are listed and briefly summarized below:

1. Developed the *SCBM* model for surface registration and the *surface ROI mesh* for analysis: The motivation and the mathematical description of the *SCBM* was described in chapter 3 and published in [93]. The *SCBM* was used as the template model for mapping individual brain surfaces to each other. The conformal parameterization approach for geometry preserving mapping and the various constraints defined for accurate registration were explained too. Moreover, we also evaluated the accuracy of the mapping using qualitative tests. We extended the surface registration framework to include the volumetric alignment of subcortical structures [93].

2. SCBM-based quantitative cross-subject analysis of features extracted from imaging modalities: In chapter 4, we analyze different features extracted from functional modalities like PET and EEG and quantify their significance through hypothesis testing. Scientific visualization tools provide support for effective spatial localization of features and visual confirmation of the analysis results. Practical examples of functional analyses [94] [2] was included in the chapter, and it confirms the usability of the technique in clinical diagnosis. We also focus on developing new algorithms for processing vector-valued diffusion images. We derived intuitive measures for analyzing connectivity between different anatomical areas. Clustering individual fibers into bundles [78] allowed us to measure connection strengths between cortical areas and analyze atrophy among fiber bundles. We applied our algorithm to multiple neurological cases and quantified the differences using anisotropy, connectivity, and curvature measures [92] [93].

3. Visual analytics framework for understanding brain disorders: Chapter 5 introduced the two spatial representations for information visualization and analysis of the high-dimensional feature space [91]. The two representations were the coordinated multi-view layout table and the *Mollweide view*. The table layout was designed to visualize selected features across subject populations in an interactive application such that the most significant features will be viewed simultaneously. It provides an interface to explore feature relationships in an interactive setting. The *Mollweide view* integrates multiple image modalities by mapping image features to visual attributes like color and shape. We could easily discover the interdependencies between results obtained independently from individual features, but not visible in the physical space. BrainFusion was built on the idea of using the information space for analytical processing of features across the complete imaging space. The anatomical dimension was the basis for the creation of the high-dimensional feature vector. Within this structured space, the framework was built to assist the user with his exploration of multiple features through an interactive interface [10]. Ranking measures highlighted the significance of certain features, and the different selections were complemented with graphic plots and an efficient query interface for reliable management, retrieval and presentation of the data. The human insight was transformed to accurate analysis models that provided on-demand confirmation of the user's choices. Coordinated display views presented a visual picture of the choices during the exploration process as well as the final results.

6.2 Future Work

The analytic framework is still at its very early stages, and there are multiple avenues available for further research. We list a couple of them below:

1. ***DTIInsight*: whole brain fiber bundle analysis:** Probabilistic white matter tractography of the whole brain takes an inordinately long time to compute. To speed up analysis,

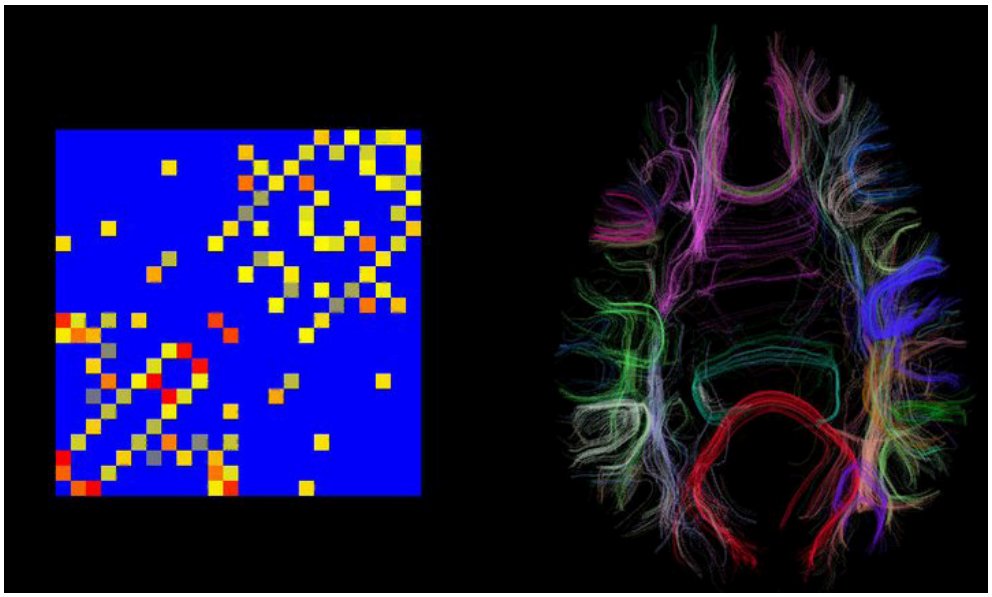

(a) (b)

Figure 6.1: (a)Mean FA distribution of fiber bundles arranged as a 2-D matrix of colors. (b) The cortico-cortical fiber bundles.

most researchers tend to concentrate on specific fiber structures only. This is a pragmatic approach for neurological cases where the location of the abnormality is roughly known or identified using a complementary measure. The second assumption among researchers is the reliability of the measure chosen for analysis. Most researchers tend to limit their analysis only to popular anisotropy measures. But as Pagani [89] describes in his paper, tissue heterogeneity causes different anatomical locations to be sensitive to different anisotropy and orientation measures, and these differences reflect on the fibers too. Hence, popular measures may or may not be applicable for the current fiber bundle under evaluation. Simultaneously identifying the bundle of interest as well as the sensitivity of the fiber bundle to a particular measure can be a labor-intensive process and will benefit from an interactive analytical processing framework. Each individual subject is clustered into individual fiber bundles that encompass the entire brain surface. We have identified 58 such fiber bundles as shown in Figure 6.1. Diffusion measures, such as the mean FA value acquired for each bundle, are arranged as a matrix image as shown is

Figure 6.1(a). Consistency measures rank the similarity of this image within and across subject groups. For example, an uncertainty rank predictor -for example, an entropy-based measure- can record the similarity within its subject groups. Similar rank values can be predicted across multiple measures that are derived from either the DTI image or other diffusion images such as HARDI. Some insights that may be worth exploring are listed as follows:

- The uncertainty rank should generate a maximal value for similar global distributions irrespective of the magnitude of the measure at each anatomical location. If true, any patient under study can be compared with the normal group and whichever generates a lower rank can be further scrutinized for local variability, which will direct the analyst to the significant fiber bundle.
- Ordering the fiber bundles in a matrix based on its magnitude will cluster bundles with similar measurements to each other. If these clusters are found to be consistent mostly among the normal group, any variance in a particular fiber bundle might also affect another bundle within the cluster because of similar diffusion profiles.
- If we define these fiber bundles as an anatomical dimension with the measures as attributes, we can define a high-dimensional vector similar to the one described for BrainFusion and perform a sub-space clustering or any other mining method to identify the best cluster of measures, along with the fiber bundles, with the most variance among them.

These new dimensions can be added to the BrainFusion framework for comparison with other image modalities.

2. **Extension of BrainFusion for volume visualization and micro-scale visualization:** The most obvious limitation of BrainFusion is that it is currently designed only for visual analytics of brain disorders that affect the cortical surface of the brain. The main

challenge will be in finding an efficient structure to represent the features in the subcortical areas of the brain. The second limitation that we do not address in BrainFusion is a more effective analysis of the vector field features γ. For most of our analysis, γ features are treated as measure-valued dimensions so that only scalar measures derived from γ are analyzed. Analyzing vector measures directly might help us understand the internal networks at the functional or neural level. It will also lead to the involvement of more complex tensor measures such as structure and metric tensors. The third and final limitation is the exclusion of genomics and proteomics data for our analysis. These are biological processes that happen at microscale, and until now, no relationships can be constructed between the imaging space and the genomic space. Since visual analysis has been very prolific at the genetic level, identifying the interdependencies between features found at the imaging, genetic, and molecular levels will be a very interesting area of research.

The knowledge and experience gained through the research listed in this dissertation is a an excellent precursor to visualization research in the medical field.

6.3 List of Publications

Journals

1. Daniel Barkmeier, Danielle Senador, Karine Leclercq, Darshan Pai, Jing Hua, Nash Boutros, Rafal Kaminski, and Jeffery Loeb. "Electrical, molecular and behavioral effects of interictal spiking in the rat", Neurobiology of Disease 47, 1(2012), 92-101.

2. Vahid Taimouri, Xin Liu, Zhaoqiang Lai, Chang Liu, Darshan Pai, and Jing Hua, "Colon Segmentation for Prepless Virtual Colonoscopy", IEEE Transactions on Information Technology in Biomedicine 15, 5(2011), 709-715.

3. Darshan Pai, Hamid Soltanian-Zadeh, and Jing Hua. "Evaluation of Fiber Bundles across

Subjects through Brain Mapping and Registration of Diffusion Tensor Data", NeuroImage 54, S1(2010), 165-175.

4. Cui Lin, Darshan Pai, Shiyong Lu, Otto Muzik, and Jing Hua, "Coclustering for Cross-Subject Fiber Tract Analysis through Diffusion Tensor Imaging", IEEE Transactions on Information Technology in Biomedicine 14, 2(2010), 514-525.

5. Cui Lin, Shiyong Lu, Xubo Fei, Artem Chebotko, Darshan Pai, Zhaoqiang Lai, Farshad Fotouhi, and Jing Hua, "A Reference Architecture for Scientific Workflow Management and the VIEW SOA Solution", IEEE Transactions on Service Computing 2, 1(2009), 79-92.

6. Michael E. Behen, Otto Muzik, Anita S.D. Soporta, Benjamin J. Wilson, Darshan Pai, Jing Hua, and Harry Chugani, "Abnormal Fronto-striatal Connectivity in Children with Histories of Early Deprivation: A Diffusion Tensor Imaging Study", Brain Imaging and Behavior 3, 3(2009), 292-297.

Conferences

1. Zhaoqiang Lai, Jiaxi Hu, Chang Liu, Vahid Taimouri, Darshan Pai, Jiong Zhu, Jianrong Xu, and Jing Hua, "Intra-patient Supine-Prone Colon Registration in CT Colonography Using Shape Spectrum", In Proceedings of the 13th International Conference on Medical Image Computing and Computer Assisted Intervention 13, 1(2010), pp. 332-339.

2. Cui Lin, Shiyong Lu, Xubo Fei, Darshan Pai, and Jing Hua, "A Task Based Abstraction and Mapping Approach to the Shimming Problem in Scientific Workflows", In Proceedings of the 6th IEEE International Conference on Services Computing (2009), pp. 284-291.

3. Darshan Pai, Jing Hua, and Hamid Soltanian-Zadeh, "Evaluation of specific fiber bundles

using brain mapping and registration of diffusion tensor data", In Proceedings of the Sixth annual Congress for Brain Imaging and Image Guided Therapy (2009).

4. Darshan Pai, Otto Muzik, and Jing Hua, "Quantitative analysis of diffusion tensor images across subjects using probabiistic tractography", In Proceedings of International Conference on Image Processing (2008), pp. 1448-1451.

5. Otto Muzik, Darshan Pai, Malek Makki, Anita Dias, Jing Hua, and Harry Chugani, "Application of Probabilistic Fiber Tracking for the Quantitative Assessment of the Connectivity Pattern between basal gangalia and frontal cortex in children with tourette syndrome", In Proceedings of 2008 Annual Meeting of International Society for Magnetic Resonance in Medicine (2008), pp. 2070.

6. Darshan Pai, Guangyu Zou, Jing Hua, Ming Dong, Xianfeng Gu, and Otto Muzik, "A Conformal and Statistical Surface Mapping Method for 3D-PET Analysis", In Proceedings of the Ninth International Conference on Computer Graphics and Imaging (2007), pp. 120-125.

7. Darshan Pai, Jiafeng Jiang, Jing Hua, Ye Duan, and Otto Muzik, "Segmentation of Brain Structures Using PDE-Driven Dynamic Growing", In Proceedings of the Annual Meeting of the North American Fuzzy Information Processing Society (2005), pp. 424-428.

8. Otto Muzik, Jing Hua, Darshan Pai, Guangyu Zou, Diane Chugani, Eishi Asano, and Harry Chugani, "EPITOOL- A Multimodality framework for integrative analysis of functional, anatomical and electrophysical data in epilepsy", In Proceedings of the 23rd International Symposium on Cerebral Blood Flow, Metabolism and Function and the 8th International Conference on Quantification of Brain Function with PET (2007).

Papers under Review

1. Darshan Pai, Otto Muzik and Jing Hua, “BrainFusion: A Visual Analytics Tool to Understanding Brain Disorders” ACM Transactions on Interactive Intelligent Systems.

2. Darshan Pai and Jing Hua, “EEGExplorer: A Visual Data Analysis Tool for EEG Spike Propagation” IEEE Transactions on Visualization and Computer Graphics.

REFERENCES

[1] ALEXANDER, D., PIERPAOLI, C., BASSER, N., AND GEE, J. Spatial Transformations of Diffusion Tensor Magnetic Resonance Images. *IEEE Transactions on Medical Imaging 20* (2001), 1131–1139.

[2] ALKONYI, B., JUHASZ, C., MUZIK, O., ASANO, E., SAPORTA, A., SHAH, A., AND CHUGANI, H. Quantitative brain surface mapping of an electrophysiological/metabolic mismatch in human neocortical epilepsy. *Epilepsy Research 87* (2009), 77–87.

[3] ANKERST, M., BERCHTOLD, S., AND KEIM, D. A. Similarity Clustering of Dimensions for an Enhanced Visualization of Multidimensional Data. In *Proceedings of the 1998 IEEE Symposium on Information Visualization* (Washington, DC, USA, 1998), IEEE Computer Society, pp. 52–60.

[4] ANTICEVIC, A., DIERKER, D., GILLESPIE, S., REPOVS, G., CSERNANSKY, J., ESSEN, D. V., AND BARCH, D. Comparing surface-based and volume-based analyses of functional neuroimaging data in patients with schizophrenia. *NeuroImage 41*, 3 (2008), 835–848.

[5] ASHBURNER, J. *Brain Warping*. New York: Academic, 1999, ch. Spatial Normalization, pp. 27–44.

[6] ASHBURNER, J., AND FRISTON, K. J. Voxel-Based Morphometry – The Methods. *NeuroImage 11*, 6 (2000), 805 – 821.

[7] ASHBURNER, J., HUTTON, C., FRACKOWIAK, R., JOHNSRUDE, I., PRICE, C., AND FRISTON, K. Identifying Global Anatomical Differences: Deformation-Based Morphometry. *Human Brain Mapping 6* (1998), 348–357.

[8] ASIMOV, D. The grand tour: a tool for viewing multidimensional data. *SIAM Journal on Scientific and Statistical Computing 6*, 1 (1985), 128–143.

[9] AVANTS, B., AND GEE, J. Shape averaging with diffeomorphic flows for atlas creation. In *IEEE International Symposium on Biomedical Imaging: Nano to Macro, 2004.* (April 2004), vol. 1, pp. 595 – 598.

[10] BARKMEIER, D., SENADOR, D., LECLERCQ, K., PAI, D., HUA, J., BOUTROS, N., KAMINSKI, R., AND LOEB, J. Electrical, molecular and behavioral effects of interictal spiking in the rat. *Neurobiology of Disease 47*, 1 (2012), 92–101.

[11] BASSER, P., MATTIELLO, J., AND LEBIHAN, D. Estimation of the Effective Self-Diffusion Tensor from the NMR Spin Echo. *Journal of Magnetic Resonance, Series B 103*, 3 (1994), 247–254.

[12] BEHEN, M., MIZIK, O., SAPORTA, A., WILSON, B., PAI, D., HUA, J., AND CHUGANI, H. Abnormal fronto-striatal connectivity in children with histories of early deprivation: A diffusion tensor imaging study. *Human Brain and Behavior 3*, 3 (2009), 292–297.

[13] BOOKSTEIN, F. L. Principal Warps: Thin-Plate Splines and the Decomposition of Deformations. *IEEE Transactions on Pattern Analysis and Machine Intelligence 11*, 6 (1989), 567–585.

[14] BORG, I., AND GROENEN, P. *Modern Multidimensional Scaling: theory and applications*. Springer-Verlag, New York, 2005.

[15] BORKIN, M., GAJOS, K., PETERS, A., MITSOURAS, D., MELCHIONNA, S., RYBICKI, F., FELDMAN, C., AND PFISTER, H. Evaluation of Artery Visualizations for Heart Disease Diagnosis. *IEEE Transactions on Visualization and Computer Graphics 17*, 12 (Dec. 2011), 2479–2488.

[16] BREHENS, T., WOOLRICH, M., JENKINSON, M., JOHANSEN-BERG, H., NUNES, R., CLARE, S., MATTHEWS, P., BRADY, J., AND SMITH, S. Characterization and Propogation of Uncertainty in Diffusion-Weighted MR Imaging. *Magnetic Resonance in Medicine 50*, 5 (2003), 1077–1088.

[17] BRUGGEMANN, J. M., SOM, S. S., LAWSON, J. A., HAINDL, W., CUNNINGHAM, A. M., AND BYE, A. M. E. Application of statistical parametric mapping to SPET in the assessment of intractable childhood epilepsy. *European Journal of Nuclear Medicine and Molecular Imaging 31*, 3 (2004), 369–77.

[18] BUSS, S. R., AND FILLMORE, J. P. Spherical Averages and Applications to Spherical Splines and Interpolation. *ACM Transactions on Graphics 20*, 2 (2001), 95–126.

[19] CASELLES, V., CATTÉ, F., COLL, T., AND DIBOS, F. A geometric model for active contours in image processing. *Numerische Mathematik 66*, 1 (Dec. 1993), 1–31.

[20] CASELLES, V., KIMMEL, R., AND SAPIRO, G. Geodesic Active Contours. *International Journal of Computer Vision 22* (1995), 61–79.

[21] CHAMBERS, J., CLEVELAND, W., TUKEY, P., AND KLEINER, B. *Graphical Methods for Data Analysis*. Duxbury Press, Boston, MA, 1983.

[22] CHEN, W., DING, Z., ZHANG, S., MACKAY-BRANDT, A., CORREIA, S., QU, H., CROW, J. A., TATE, D. F., YAN, Z., AND PENG, Q. A Novel Interface for Interactive Exploration of DTI Fibers. *IEEE Transactions on Visualization and Computer Graphics 15*, 6 (2009), 1433–1440.

[23] CHERNOFF, H. The Use of Faces to Represent Points in k-Dimensional Space Graphically. *Journal of the American Statistical Association 68*, 342 (1973), 361–368.

[24] CHRISTENSEN, G., JOSHI, S., AND MILLER, M. Volumetric Transformation of Brain Anatomy. *IEEE Transactions on Medical Imaging 16*, 6 (Dec. 1997), 864 –877.

[25] CHRISTENSEN, G., RABBITT, R., AND MILLER, M. Deformable Ttemplates Using Large Deformation Kinematics. *IEEE Transactions on Image Processing 5*, 10 (Oct 1996), 1435 –1447.

[26] CHUA, C. S., AND JARVIS, R. Point Signatures: A New Representation for 3D Object Recognition. *International Journal of Computer Vision 25*, 1 (Oct. 1997), 63–85.

[27] COHEN, L., AND KIMMEL, R. Global minimum for active contour models: A minimal path approach. *International Journal of Computer Vision 24* (1997), 57–78.

[28] COOK, D., BUJA, A., CABRERA, J., AND HURLEY, C. Grand Tour and Projection Pursuit. *Journal of Computational and Graphical Statistics 4*, 3 (1995), 155–172.

[29] COOTES, T. F., TAYLOR, C. J., COOPER, D. H., AND GRAHAM, J. Active Shape Models-Their Training and Application. *Computer Vision and Image Understanding 61*, 1 (Jan 1995), 38–59.

[30] DE NIL, L., SASISEKARAN, J., VAN LIESHOUT, P., AND SANDOR, P. Speech disfluencies in individuals with Tourette syndrome. *Journal of Psychosomatic Research 58*, 1 (2005), 97–102.

[31] DUNCAN, J., AND AYACHE, N. Medical image analysis: progress over two decades and the challenges ahead. *IEEE Transactions on Pattern Analysis and Machine Intelligence 22*, 1 (Jan 2000), 85 –106.

[32] DURRLEMAN, S., PENNEC, X., TROUVÉ, A., AND AYACHE, N. Measuring Brain Variability via Sulcal Lines Registration: a Diffeomorphic Approach. In *Proceedings of the 10th international conference on Medical Image Computing and Computer-Assisted Intervention* (Berlin, Heidelberg, 2007), MICCAI'07, Springer-Verlag, pp. 675–682.

[33] DURRLEMAN, S., PENNEC, X., TROUVÈ, A., THOMPSON, P., AND AYACHE, N. Inferring brain variability from diffeomorphic deformations of currents: an integrative approach. *Medical Image Analysis 12*, 5 (2008), 626–637.

[34] ELMQVIST, N., DRAGICEVIC, P., AND FEKETE, J.-D. Rolling the Dice: Multidimensional Visual Exploration using Scatterplot Matrix Navigation. *IEEE Transactions on Visualization and Computer Graphics 14*, 6 (Nov.-Dec. 2008), 1539–1148.

[35] ESSEN, D. V., DRURY, H., DICKSON, J., HARWELL, J., HANLON, D., AND ANDERSON, C. An Integrated Software Suite for Surface-based Analyses of Cerebral Cortex. *Journal of the American Medical Informatics Association 8*, 5 (2001), 443–459.

[36] EVANS, A., COLLINS, D., MILLS, S., BROWN, E., KELLY, R., AND PETERS, T. 3D statistical neuroimaging models from 305 MRI volumes. In *IEEE Nuclear Science Symposium and Medical Imaging Conference* (1993), vol. 3, pp. 1813–1817.

[37] FILLARD, P., ARSIGNY, V., PENNEC, X., HAYASHI, K., THOMPSON, P., AND AYACHE, N. Measuring brain variability by extrapolating sparse tensor fields measured on sulcal lines. *NeuroImage 34*, 2 (2007), 639–650.

[38] FISCHL, B., SALAT, D., BUSA, E., ALBERT, M., DIETERICH, M., HASELGROVE, C., KOUWE, A., KILLIANY, R., KENNEDY, D., KLAVENESS, S., MONTILLO, A., MAKRIS, N., ROSEN, B., AND DALE, A. Whole Brain Segmentation: Automated Labeling of Neuroanatomical Structures in the Human Brain. *Neuron 33*, 3 (2002), 341–355.

[39] FISCHL, B., SERENO, M. I., AND DALE, A. M. Cortical Surface-Based Analysis II: Inflation, Flattening, and a Surface-Based Coordinate System. *NeuroImage 9*, 2 (1999), 195–207.

[40] FISCHL, B., SERENO, M. I., TOOTELL, R. B., AND DALE, A. M. High-resolution intersubject averaging and a coordinate system for the cortical surface. *Human Brain Mapping 8* (1999), 272–284.

[41] FRIEDMAN, J. H., AND TUKEY, J. W. A Projection Pursuit Algorithm for Exploratory Data Analysis. *IEEE Transactions on Computers 23*, 9 (1974), 881–890.

[42] FRIMAN, O., FARNEBÄACK, G., AND WESTIN, C.-F. A Bayesian Approach for Stochastic White Matter Tractography. *IEEE Transactions on Medical Imaging 25*, 8 (2006), 965–978.

[43] FRISTON, K. J., HOLMES, A. P., WORSLEY, K. J., POLINE, J.-P., FRITH, C. D., AND FRACKOWIAK, R. S. J. Statistical Parametric Maps in Functional Imaging: A General Linear Approach. *Human Brain Mapping 2*, 4 (1995), 189–210.

[44] GARG, S., NAM, J. E., RAMAKRISHNAN, I. V., AND MUELLER, K. Model-driven Visual Analytics. In *IEEE Symposium on Visual Analytics Science and Technology* (2008), IEEE, pp. 19–26.

[45] GIBBS, P., BUCKLEY, D., BLACKBAND, S., AND HORSMAN, A. Tumour volume determination from MR images by morphological segmentation. *Physics in Medicine and Biology 41*, 11 (1996), 2437–2446.

[46] GIBSON, E., KHAN, A. R., AND BEG, M. F. A Combined Surface and Volumetric Registration (SAVOR) Framework to Study Cortical Biomarkers and Volumetric Imaging Data. In *Proceedings of the 12th International Conference on Medical Image Computing and Computer-Assisted Intervention: Part I* (Berlin, Heidelberg, 2009), MICCAI '09, Springer-Verlag, pp. 713–720.

[47] GLAUNÈS, J., VAILLANT, M., AND MILLER, M. I. Landmark Matching via Large Deformation Diffeomorphisms on the Sphere. *Journal of Mathematical Imaging and Vision 20* (Jan 2004), 179–200.

[48] GU, X., WANG, Y., CHAN, T. F., THOMPSON, P. M., AND YAU, S.-T. Genus Zero Surface Conformal Mapping and Its Application to Brain Surface Mapping. *IEEE Transactions on Medical Imaging 23*, 8 (2004), 949–958.

[49] GUO, D. Coordinating computational and visual approaches for interactive feature selection and multivariate clustering. *Information Visualization 2*, 4 (2003), 232–246.

[50] HAN, C., HATSUKAMI, T., HWANG, J.-N., AND YUAN, C. A fast minimal path active contour model. *IEEE Transactions on Image Processing 10*, 6 (Jun 2001), 865 –873.

[51] HARALICK, R., AND SHAPIRO, L. Image segmentation techniques. *Computer Vision, Graphics, and Image Processing 29*, 1 (1985), 100–132.

[52] HARROWER, M. A., AND BREWER, C. A. Colorbrewer.org: An Online Tool for Selecting Color Schemes for Maps. *The Cartographic Journal 40*, 1 (2003), 27–37.

[53] HE, Y., GU, X., AND QIN, H. Rational spherical splines for genus zero shape modeling. In *Proceedings of the International Conference on Shape Modeling and Applications* (2005), pp. 82–91.

[54] HECKENBERG, G., XI, Y., DUAN, Y., AND HUA, J. Brain Structure Segmentation from MRI by Geometric Surface Flow. *International Journal of Biomedical Imaging* (2006), 1–6.

[55] HELLIER, P., BARILLOT, C., COROUGE, I., GIBAUD, B., GOUALHER, G. L., COLLINS, D. L., EVANS, A., MALANDAIN, G., AYACHE, N., CHRISTENSEN, G. E., AND JOHNSON, H. J. Retrospective Evaluation of Intersubject Brain Registration. *IEEE Transactions on Medical Imaging 22*, 9 (2003), 1120–1130.

[56] HUBER, P. J. Projection Pursuit. *The Annals of Statistics 13*, 2 (1985), 435–475.

[57] HURDAL, M., STEPHENSON, K., BOWERS, P., SUMNERS, D., AND ROTTENBERG, D. Coordinate Systems for Conformal Cerebellar Flat Maps. *NeuroImage 11*, 5 (2000), S467.

[58] INSELBERG, A., AND DIMSDALE, B. Parallel coordinates: a tool for visualizing multi-dimensional geometry. *Visualization '90., Proceedings of the First IEEE Conference on* (Oct 1990), 361–378.

[59] IRIMIA, A., CHAMBERS, M., TORGERSON, C., AND HORN, J. Circular representation of human cortical networks for subject and population-level connectomic visualization. *NeuroImage 60*, 2 (2012), 1340–1351.

[60] JENKINSON, M., AND SMITH, S. A global optimisation method for robust affine registration of brain images. *Medical Image Analysis 5*, 2 (2001), 143–156.

[61] JIANU, R., DEMIRALP, C., AND LAIDLAW, D. Exploring 3D DTI Fiber Tracts with Linked 2D Representations. *IEEE Transactions on Visualization and Computer Graphics 15*, 6 (2009), 1449–1456.

[62] JOHANSSON, S., AND JOHANSSON, J. Interactive Dimensionality Reduction Through User-defined Combinations of Quality Metrics. *IEEE Transactions on Visualization and Computer Graphics 15*, 6 (2009), 993–1000.

[63] JONES, D., GRIFFIN, L., ALEXANDER, D., CATANI, M., HORSFIELD, M., HOWARD, R., AND WILLIAMS, S. Spatial Normalization and Averaging of Diffusion Tensor MRI Datasets. *NeuroImage 17*, 2 (2002), 592–617.

[64] JOSHI, A., SHATTUCK, D., THOMPSON, P., AND LEAHY, R. A Framework for Registration, Statistical Characterization and Classification of Cortically Constrained Functional Imaging Data. In *Information Processing in Medical Imaging*, G. Christensen

and M. Sonka, Eds., vol. 3565 of *Lecture Notes in Computer Science*. Springer Berlin / Heidelberg, 2005, pp. 83–101.

[65] JOSHI, A., SHATTUCK, D., THOMPSON, P., AND LEAHY, R. Surface-Constrained Volumetric Brain Registration Using Harmonic Mappings. *IEEE Transactions on Medical Imaging 26*, 12 (dec. 2007), 1657 –1669.

[66] JOSHI, A., SHATTUCK, D. W., THOMPSON, P. M., AND LEAHY, R. M. Thin Plate Spline Registration in the Intrinsic Geometry of the Cortical Surface. *Human Brain Mapping* (2005).

[67] KANDEL, S., PAEPCKE, A., HELLERSTEIN, J., AND HEER, J. Wrangler: Interactive Visual Specification of Data Transformation Scripts. In *Proceedings of the SIGCHI Conference on Human Factors in Computing Systems* (New York, NY, USA, 2011), CHI '11, ACM, pp. 3363–3372.

[68] KAUS, M., WARFIELD, S., NABAVI, A., BLACK, P., JOLESZ, F., AND KIKINIS, R. Automated Segmentation of MR Images of Brain Tumors. *Radiology 218* (2001), 586–591.

[69] KAZHDAN, M., FUNKHOUSER, T., AND RUSINKIEWICZ, S. Rotation Invariant Spherical Harmonic Representation of 3D Shape Descriptors. In *Proceedings of the 2003 Eurographics/ACM SIGGRAPH symposium on Geometry processing* (Aire-la-Ville, Switzerland, Switzerland, 2003), SGP '03, Eurographics Association, pp. 156–164.

[70] KEIM, D. A. Information Visualization and Visual Data Mining. *IEEE Transactions on Visualization and Computer Graphics 8* (Jan 2002), 1–8.

[71] KEIM, D. A., AND KRIEGEL, H.-P. VisDB: Database Exploration Using Multidimensional Visualization. *IEEE Computer Graphics and Applications 14*, 5 (1994), 40–49.

[72] KIM, Y., LEE, D., LEE, S., CHUNG, C., CHUNG, J., AND LEE, M. 18F-FDG PET in Localization of Frontal Lobe Epilepsy: Comparison of Visual and SPM analysis. *Journal of Nuclear Medicine 43*, 9 (2002), 1167–1174.

[73] KOHONEN, T., SCHROEDER, M. R., AND HUANG, T. S., Eds. *Self-Organizing Maps*, 3rd ed. Springer-Verlag New York, Inc., Secaucus, NJ, USA, 2001.

[74] KOSARA, R., BENDIX, F., AND HAUSER, H. Parallel Sets: Interactive Exploration and Visual Analysis of Categorical Data. *IEEE Transactions on Visualization and Computer Graphics 12*, 4 (July 2006), 558–568.

[75] KOSARA, R., HAUSER, H., AND GRESH, D. An Interaction View on Information Visualization. In *EUROGRAPHICS* (2003), pp. 123–137.

[76] LEBLANC, J., WARD, M. O., AND WITTELS, N. Exploring N-dimensional databases. In *Proceedings of the 1st conference on Visualization '90* (Los Alamitos, CA, USA, 1990), VIS '90, IEEE Computer Society Press, pp. 230–237.

[77] LEVENTON, M., GRIMSON, W., AND FAUGERAS, O. Statistical Shape Influence in Geodesic Active Contours. In *5th IEEE EMBS International Summer School on Biomedical Imaging, 2002.* (June 2002), p. 8 pp.

[78] LIN, C., PAI, D., LU, S., MUZIK, O., AND HUA, J. Coclustering for Cross-subject Fiber Tract Analysis Through Diffusion Tensor Imaging. *Transactions on Information Technology in Biomedicine 14* (March 2010), 514–525.

[79] LITKE, N., DROSKE, M., RUMPF, M., AND SCHRÖDER, P. An Image Processing Approach to Surface Matching. In *Proceedings of the Eurographics Symposium on Geometry Processing (SGP'05)* (2005), pp. 207–216.

[80] LOHMANN, G. Extracting line representations of sulcal and gyral patterns in MR images of the human brain. *IEEE Transactions on Medical Imaging 17*, 6 (1998), 1040 –1048.

[81] MAINTZ, J. B. A., AND VIERGEVER, M. A. A Survey of Medical Image Registration. *Medical Image Analysis 2* (1998), 1–36.

[82] MANGIN, J. F., RIVIÈRE, D., CACHIA, A., DUCHESNAY, E., COINTEPAS, Y., PAPADOPOULOS-ORFANOS, D., COLLINS, D. L., EVANS, A. C., AND RÈGIS, J. Object-Based Morphometry of the Cerebral Cortex. *IEEE Transactions on Medical Imaging 23*, 8 (2004), 968–982.

[83] MCINERNEY, T., AND TERZOPOULOS, D. T-snakes: Topology adaptive snakes. *Medical Image Analysis* (2000), 73–91.

[84] MCINERNEY, T., AND TERZOPOULOS, D. *Handbook of Medical Image Processing and Analysis*, 2nd ed. Academic Press, 2008, ch. Deformable Models, pp. 145–166.

[85] MILLER, M., BANERJEE, A., CHRISTENSEN, G., JOSHI, S., KHANEJA, N., GERNANDER, U., AND MATEJIC, L. Statistical methods in computational neuroanatomy. *Statistical Methods in Medical Research 6*, 3 (1997), 267–299.

[86] MUZIK, O., CHUGANI, D., JUHASZ, C., SHEN, C., AND CHUGANI, H. Statistical Parametric Mapping: Assessment of Application in Children. *NeuroImage 12*, 5 (2000), 538–549.

[87] OSADA, R., FUNKHOUSER, T., CHAZELLE, B., AND DOBKIN, D. Shape distributions. *ACM Transactions on Graphics 21* (Oct 2002), 807–832.

[88] OSHER, S., AND SETHIAN, J. *Fronts propagating with curvature dependent speed: algorithms based on Hamilton-Jacobi formulations*. NASA Langley Research Center, 1987.

[89] PAGANI, E., FILIPPI, M., ROCCA, M., AND HORSFIELD, M. A method for obtaining tract-specific diffusion tensor MRI measurements in the presence of disease: Appli-

cations to patients with clinically isolated syndromes suggestive of multiple sclerosis. *Neuroimage 26* (2005), 258–265.

[90] PAI, D., JIANG, J., HUA, J., DUAN, Y., MUZIK, O., AND LU, S. Segmentation of brain structures using PDE-driven surface growing. In *Annual Meeting of the North American Fuzzy Information Processing Society, 2005. NAFIPS 2005.* (June 2005), pp. 424 – 428.

[91] PAI, D., LOEB, J., MUZIK, O., AND HUA, J. BrainFusion: A Visual Analytics Tool to Understanding Brain Disorders. *ACM Transactions on Interactive Intelligent Systems Submitted*.

[92] PAI, D., MUZIK, O., AND HUA, J. Quantitative analysis of diffusion tensor images across subjects using probabilistic tractography. In *15th IEEE International Conference on Image Processing, 2008.* (Oct. 2008), pp. 1448–1451.

[93] PAI, D., SOLTANIAN-ZADEH, H., AND HUA, J. Evaluation of fiber bundles across subjects through brain mapping and registration of diffusion tensor data. *NeuroImage 54* (2011), 165–175.

[94] PAI, D., ZOU, G., HUA, J., DONG, M., GU, X., AND MUZIK, O. A conformal and statistical mapping method for 3D PET image analysis. In *Proceedings of the Ninth IASTED International Conference on Computer Graphics and Imaging* (Anaheim, CA, USA, 2007), CGIM '07, ACTA Press, pp. 120–125.

[95] PANTAZIS, D., JOSHI, A., JIANG, J., SHATTUCK, D., BERNSTEIN, L., DAMASIO, H., AND LEAHY, R. Comparison of landmark-based and automatic methods for cortical surface registration. *NeuroImage 49*, 3 (2010), 2479–2493.

[96] PARK, H.-J., KUBICKI, M., SHENTON, M., GUIMOND, A., MCCARLEY, R., MAIER, S., KIKINIS, R., JOLESZ, F., AND WESTIN, C.-F. Spatial normalization of diffusion tensor MRI using multiple channels. *NeuroImage 20* (2003), 1995–2009.

[97] PHAM, D. L., XU, C., AND PRINCE, J. L. Current methods in medical image segmentation. *Annual Review of Biomedical Engineering 2*, 1 (2000), 315–337. PMID: 11701515.

[98] RAO, R., AND CARD, S. K. The Table Lens: Merging Graphical and Symbolic Representations in an Interactive Focus+Context Visualizations for Tabular Information. In *Conference Companion on Human Factors in Computing Systems* (New York, NY, USA, 1994), CHI '94, ACM, pp. 222–228.

[99] RICHARDSON, M., KOEPP, M., BROOKS, D., AND DUNCAN, J. 11c-flumazenil PET in neocortical epilepsy. *Neurology 51* (1998), 485–492.

[100] SAHOO, P. K., SOLTANI, S., WONG, A. K., AND CHEN, Y. C. A survey of thresholding techniques. *Computer Vision, Graphics, and Image Processing 41* (February 1988), 233–260.

[101] SCHMID, J., AND MAGNENAT-THALMANN, N. MRI Bone Segmentation using Deformable Models and Shape Priors. In *Proceedings of the 11th international conference on Medical Image Computing and Computer-Assisted Intervention - Part I* (Berlin, Heidelberg, 2008), MICCAI '08, Springer-Verlag, pp. 119–126.

[102] SCHNEIDEWIND, J., SIPS, M., AND KEIM, D. A. An automated approach for the optimization of pixel-based visualizations. *Information Visualization 6*, 1 (2007), 75–88.

[103] SEO, J., AND SHNEIDERMAN, B. Interactively Exploring Hierarchical Clustering Results. *Computer 35*, 7 (2002), 80–86.

[104] SEO, J., AND SHNEIDERMAN, B. A Rank-by-Feature Framework for Unsupervised Multidimensional Data Exploration Using Low Dimensional Projections. In *Proceedings of the IEEE Symposium on Information Visualization* (Washington, DC, USA, 2004), IEEE Computer Society, pp. 65–72.

[105] SHEN, L., AND SAYKIN, A. J. Surface-based Morphometric Analysis for Hippocampal Shape in Schizophrenia. In *Human Brain Mapping* (2003).

[106] SINGER, H., AND MINZER, K. Neurobiology of Tourettes syndrome: concepts of neuroanatomic localization and neurochemical abnormalities. *Brain and Development 25* (2003), 70–84.

[107] SIPS, M., NEUBERT, B., LEWIS, J., AND HANRAHAN, P. Selecting good views of high-dimensional data using class consistency. *Computer Graphics Forum 28*, 3 (2009), 831–838.

[108] SMITH, S. M., JENKINSON, M., WOOLRICH, M. W., BECKMANN, C. F., BEHRENS, T. E. J., JOHANSEN-BERG, H., BANNISTER, P. R., LUCA, M. D., DROBNJAK, I., FLITNEY, D. E., NIAZY, R. K., SAUNDERS, J., VICKERS, J., ZHANG, Y., STEFANO, N. D., BRADY, J. M., AND MATTHEWS, P. M. Advances in Functional and Structural MR Image Analysis and Implementation as FSL. *NeuroImage 23* (2004), 208–219.

[109] STOKKING, R., ZUIDERVELD, K. J., HULSHOFF POL, H. E., VAN RIJK, P. P., AND VIERGEVER, M. A. Normal fusion for three-dimensional integrated visualization of SPECT and magnetic resonance brain images. *Journal of Nuclear Medicine 38*, 4 (1997), 624–629.

[110] STYNER, M., GERIG, G., LIEBERMAN, J., JONES, D., AND WEINBERGER, D. Statistical shape analysis of neuroanatomical structures based on medial models. *Medical Image Analysis 7* (2003), 207–220.

[111] SURI, J., LIU, K., SINGH, S., LAXMINARAYAN, S., ZENG, X., AND REDEN, L. Shape recovery algorithms using level sets in 2-D/3-D medical imagery: a state-of-the-art review. *IEEE Transactions on Information Technology in Biomedicine 6*, 1 (March 2002), 8 –28.

[112] SZALAY, A. S., GRAY, J., FEKETE, G., KUNSZT, P. Z., KUKOL, P., AND THAKAR, A. Indexing the Sphere with the Hierarchical Trangular Mesh. Technical Report MSR-TR-2005-123, Microsoft Research, 2005.

[113] TALAIRACH, J., AND TOURNOUX, P. *Co-Planar Stereotaxic Atlas of the Human Brain: 3-Dimensional Proportional System : An Approach to Cerebral Imaging*. Thieme Medical Publishers, Jan. 1988.

[114] TATU, A., ALBUQUERQUE, G., EISEMANN, M., BAK, P., THEISEL, H., MAGNOR, M., AND KEIM, D. Automated Analytical Methods to Support Visual Exploration of High-Dimensional Data. *IEEE Transactions on Visualization and Computer Graphics 17*, 5 (2011), 584–597.

[115] THOMPSON, P., MCDONALD, D., MEGA, S., HOLMES, J., EVANS, C., AND TOGA, A. Detection and mapping of abnormal brain structure with a probabilistic atlas of cortical surfaces. *Journal of Computer Assisted Tomography 21*, 4 (1997), 567–581.

[116] THOMPSON, P. M., HAYASHI, K. M., SOWELL, E. R., GOGTAY, N., GIEDD, J. N., RAPOPORT, J. L., DE ZUBICARAY, G. I., JANKE, A. L., ROSE, S. E., SEMPLE, J., DODDRELL, D. M., WANG, Y., VAN ERP, T. G., CANNON, T. D., AND TOGA, A. W. Mapping cortical change in Alzheimer's disease, brain development and schizophrenia. *NeuroImage 23*, 1 (2004), S2–S18.

[117] THOMPSON, P. M., AND TOGA, A. W. A framework for computational anatomy. *Computing and Visualization in Science 5* (2002), 13–34.

[118] THOMPSON, P. M., WOODS, R. P., MEGA, M. S., AND TOGA, A. W. Mathematical/Computational Challenges in Creating Deformable and Probabilistic Atlases of the Human Brain. *Human Brain Mapping 9*, 2 (2000), 81–92.

[119] TOGA, A. W. *Brain Warping*, 1st ed. Academic Press, 1999.

[120] TOSUN, D., AND PRINCE, J. Cortical Surface Alignment Using Geometry Driven Multispectral Optical Flow. In *Information Processing in Medical Imaging*, G. Christensen and M. Sonka, Eds., vol. 3565 of *Lecture Notes in Computer Science*. Springer Berlin / Heidelberg, 2005, pp. 519–531.

[121] TOSUN, D., RETTMANN, M. E., AND PRINCE, J. L. Mapping techniques for aligning sulci across multiple brains. *Medical Image Analysis 8*, 3 (2004), 295–309.

[122] TURK, G., AND O'BRIEN, J. F. Shape Transformation Using Variational Implicit Functions. In *Proceedings of the 26th annual conference on Computer Graphics and Interactive Techniques* (1999), pp. 335–342.

[123] VAILLANT, M., DAVATZIKOS, C., AND BRYAN, R. N. Finding 3D Parametric Representations of the Deep Cortical Folds. In *Proc. of the IEEE Workshop on Mathematical Methods in Biomedical Image Analysis* (1996), IEEE Computer Society Press, pp. 151–159.

[124] VEMURI, B. C., MITICHE, A., AND AGGARWAL, J. K. Curvature-based representation of objects from range data. *Image and Vision Computing 4* (May 1986), 107–114.

[125] VON STOCKHAUSEN, H. M., PIETRZYK, U., AND HERHOLZ, K. "3D-tool" - a software system for visualisation and analysis of coregistered multimodality volume datasets of individual subjects. *NeuroImage 7*, 4 (1998), S799.

[126] WAHBA, G. Spline interplolation and smooothing on the sphere. *SIAM Journal on Scientific and Statistical Computing 2*, 1 (1981), 5–16.

[127] WAKANA, S., CAPRIHAN, A., PANZENBOECK, M., FALLON, J., PERRY, M., GOLLUB, R., HUA, K., ZHANG, J., JIANG, H., DUBEY, P., BLITZ, A., ZIJL, P., AND MORI, S. Reproducibility of quantitative tractography methods applied to cerebral white matter. *Neuroimage 36*, 3 (2009), 630–644.

[128] WANG, S., WANG, Y., JIN, M., GU, X., AND SAMARAS, D. 3D Surface Matching and Recognition Using Conformal Geometry. In *Proceedings of the IEEE Computer Society Conference on Computer Vision and Pattern Recognition (CVPR'06)* (2006), pp. 2453–2460.

[129] WANG, Y., CHIANG, M.-C., AND THOMPSON, P. M. Automated Surface Matching Using Mutual Information Applied to Riemann Surface Structures. In *Proc. The 8th International Conference on Medical Image Computing and Computer-Assisted Intervention (MICCAI'05)* (2005), pp. 675–683.

[130] WANG, Y., GU, X., CHAN, T. F., THOMPSON, P. M., AND YAU, S.-T. Volumetric harmonic brain mapping. In *IEEE International Symposium on Biomedical Imaging: Macro to Nano* (2004), pp. 1275–1278.

[131] WANG, Y., LIU, L. M., CHAN, T. F., AND THOMPSON, P. M. Optimization of Brain Conformal Mapping with Landmarks. In *Proc. The 8th International Conference on Medical Image Computing and Computer-Assisted Intervention (MICCAI'05)* (2005), pp. 675–683.

[132] WARD, M. O. Xmdvtool: integrating multiple methods for visualizing multivariate data. In *Proceedings of the Conference on Visualization '94* (Los Alamitos, CA, USA, 1994), IEEE Computer Society Press, pp. 326–333.

[133] WATKINS, K., PAUS, T., LERCH, J., ZIJDENBOS, A., COLLINS, D., NEELIN, P., TAYLOR, J., WORSLEY, K., AND EVANS, A. Structural Asymmetries in the Human

Brain: a Voxel-based Statistical Analysis of 142 MRI Scans. *Cerebral Cortex 11*, 9 (2001), 868–877.

[134] WILKINSON, L., ANAND, A., AND GROSSMAN, R. Graph-Theoretic Scagnostics. In *Proceedings of the 2005 IEEE Symposium on Information Visualization* (Washington, DC, USA, 2005), IEEE Computer Society, pp. 157–164.

[135] WOODS, R., GRAFTON, S., HOLMES, C., CHERRY, S., AND MAZZIOTTA, J. Automated Image Registration: I. General Methods and Intrasubject, Intramodality Validation. *Journal of Computer Assisted Tomography 22* (1998), 139–152.

[136] WORSLEY, K. J., TAYLOR, J. E., CARBONELL, F., CHUNG, M. K., DUERDEN, E., BERNHARDT, B., LYTTELTON, O., BOUCHER, M., AND EVANS, A. Surfstat: A Matlab toolbox for the statistical analysis of univariate and multivariate surface and volumetric data using linear mixed effects models and random field theory. In *Human Brain Mapping 2009 Annual Meeting* (2009), vol. 47, p. S102.

[137] YAN, P., AND KASSIM, A. Medical Image Segmentation Using Minimal Path Deformable Models With Implicit Shape Priors. *IEEE Transactions on Information Technology in Biomedicine 10*, 4 (oct. 2006), 677 –684.

[138] YANG, J., WARD, M. O., RUNDENSTEINER, E. A., AND HUANG, S. Visual Hierarchical Dimension Reduction for Exploration of High Dimensional Datasets. In *Proceedings of the Symposium on Data visualisation 2003* (Aire-la-Ville, Switzerland, Switzerland, 2003), Eurographics Association, pp. 19–28.

[139] YEO, B., SABUNCU, M., VERCAUTEREN, T., AYACHE, N., FISCHL, B., AND GOLLAND, P. Spherical Demons: Fast Diffeomorphic Landmark-Free Surface Registration. *IEEE Transactions on Medical Imaging 29*, 3 (march 2010), 650 –668.

[140] YEO, B. T. T., SABUNCU, M. R., DESIKAN, R., FISCHL, B., AND GOLLAND, P. Effects of registration regularization and atlas sharpness on segmentation accuracy. In *Proceedings of the 10th international conference on Medical image computing and computer-assisted intervention - Volume Part I* (Berlin, Heidelberg, 2007), MICCAI'07, Springer-Verlag, pp. 683–691.

[141] ZHANG, D. *Harmonic shape images: a three-dimensional free-form surface representation and its applications in surface matching*. PhD thesis, Carnegie Mellon University, Pittsburgh, PA, USA, 2000.

[142] ZHANG, Y., BRADY, M., AND SMITH, S. Segmentation of brain MR images through a hidden markov random field model and the expectation-maximization algorithm. *IEEE Transactions on Medical Imaging 20*, 1 (Jan 2001), 45 –57.

[143] ZOU, G., HUA, J., GU, X., AND MUZIK, O. An Approach for Intersubject Analysis of 3D Brain Images Based on Conformal Geometry. In *Proc. IEEE International Conference on Image Processing (ICIP'06)* (2006), pp. 1193–1196.

[144] ZOU, G., HUA, J., AND MUZIK, O. Non-rigid surface registration using spherical thin-plate splines. In *Proceedings of the 10th International Conference on Medical Image Computing and Computer-Assisted Intervention - Volume Part I* (Berlin, Heidelberg, 2007), MICCAI'07, Springer-Verlag, pp. 367–374.

ABSTRACT

VISUAL EXPLORATION AND INFORMATION ANALYTICS OF HIGH-DIMENSIONAL MEDICAL IMAGES

by

DARSHAN PAI

MAY 2013

Advisor: Dr. Jing Hua

Major: Computer Science

Degree: Doctor of Philosophy

Data visualization has transformed how we analyze increasingly large and complex data sets. Advanced visual tools logically represent data in a way that communicates the most important information inherent within it and culminate the analysis with an insightful conclusion. Automated analysis disciplines - such as data mining, machine learning, and statistics - have traditionally been the most dominant fields for data analysis. It has been complemented with a near-ubiquitous adoption of specialized hardware and software environments that handle the storage, retrieval, and pre- and postprocessing of digital data. The addition of interactive visualization tools allows an active human participant in the model creation process. The advantage is a data-driven approach where the constraints and assumptions of the model can be explored and chosen based on human insight and confirmed on demand by the analytic system. This translates to a better understanding of data and a more effective knowledge discovery. This trend has become very popular across various domains, not limited to machine learning, simulation, computer vision, genetics, stock market, data mining, and geography.

In this dissertation, we highlight the role of visualization within the context of medical image analysis in the field of neuroimaging. The analysis of brain images has uncovered amazing traits about its underlying dynamics. Multiple image modalities capture qualitatively different internal brain mechanisms and abstract it within the information space of that modality.

Computational studies based on these modalities help correlate the high-level brain function measurements with abnormal human behavior. These functional maps are easily projected in the physical space through accurate 3-D brain reconstructions and visualized in excellent detail from different anatomical vantage points. Statistical models built for comparative analysis across subject groups test for significant variance within the features and localize abnormal behaviors contextualizing the high-level brain activity. Currently, the task of identifying the features is based on empirical evidence, and preparing data for testing is time-consuming. Correlations among features are usually ignored due to lack of insight. With a multitude of features available and with new emerging modalities appearing, the process of identifying the salient features and their interdependencies becomes more difficult to perceive. This limits the analysis only to certain discernible features, thus limiting human judgments regarding the most important process that governs the symptom and hinders prediction. These shortcomings can be addressed using an analytical system that leverages data-driven techniques for guiding the user toward discovering relevant hypotheses.

The research contributions within this dissertation encompass multidisciplinary fields of study not limited to geometry processing, computer vision, and 3-D visualization. However, the principal achievement of this research is the design and development of an interactive system for multimodality integration of medical images. The research proceeds in various stages, which are important to reach the desired goal. The different stages are briefly described as follows: First, we develop a rigorous geometry computation framework for brain surface matching. The brain is a highly convoluted structure of closed topology. Surface parameterization explicitly captures the non-Euclidean geometry of the cortical surface and helps derive a more accurate registration of brain surfaces. We describe a technique based on conformal parameterization that creates a bijective mapping to the canonical domain, where surface operations can be performed with improved efficiency and feasibility. Subdividing the brain into a finite set of anatomical elements provides the structural basis for a categorical division of anatomical view-

points and a spatial context for statistical analysis. We present statistically significant results of our analysis into functional and morphological features for a variety of brain disorders.

Second, we design and develop an intelligent and interactive system for visual analysis of brain disorders by utilizing the complete feature space across all modalities. Each subdivided anatomical unit is specialized by a vector of features that overlap within that element. The analytical framework provides the necessary interactivity for exploration of salient features and discovering relevant hypotheses. It provides visualization tools for confirming model results and an easy-to-use interface for manipulating parameters for feature selection and filtering. It provides coordinated display views for visualizing multiple features across multiple subject groups, visual representations for highlighting interdependencies and correlations between features, and an efficient data-management solution for maintaining provenance and issuing formal data queries to the back end.

AUTOBIOGRAPHICAL STATEMENT

DARSHAN PAI

Darshan Pai received the MS degree in Computer Engineering from Wayne State University, Detroit, MI, in 2002. He is currently a PhD candidate in the Graphics and Imaging Laboratory in the Department of Computer Science, Wayne State University, Detroit, Michigan. His research interests are in the areas of scientific visualization, computer graphics, geometry computation, 3-D analysis, information visualization, and visual analytics. He is a student member of the ACM.